Synthesis and Characterization of Two-Dimensional Tin Chalcogenide (S, Te) Nanocrystals

Dissertation

to receive the degree

Dr. rer. nat.

at the Faculty of Mathematics, Informatics and Natural Sciences

Department of Chemistry

of the University of Hamburg

submitted by

Fu Li

Born on 06. March 1990 in Nanjing, China

Hamburg, Germany, 2019

The release for the publication of the dissertation was granted on 20.09.2019.

Dedicated to

My mother Yuefen Li, my father Zhixiang Li

My sister Xin Li

And my husband Hancong Xu

If you can't explain it simply, you don't understand it well enough.

Imagination is more important than knowledge.
-knowledge is limited. Imagination encircles the world.

Both by *Albert Einstein*

Dissertation

Title:	Synthesis and Characterization of Two-Dimensional Tin Chalcogenide (S, Te) Nanocrystals
Title (German):	Synthese und Charakterisierung zweidimensionaler Zinnchalkogenid (S, Te) -Nanokristalle
Submitted by:	Fu LI
Martrikelnummer:	6859902
Contact:	fu.li@chemie.uni-hamburg.de
Submitted on:	13.08.2019
University:	University of Hamburg
Research group:	Prof. Dr. Christian Klinke

Following reviewers recommend the adoption of the dissertation:

First reviewer:	Herr Prof. Dr. Christian Klinke
Second reviewer:	Herr Prof. Dr. Horst Weller
Time for defense:	20.09.2019

Publications

The work reported in this thesis was carried out during the period between October 2015 and May 2019 at the physical chemistry institute (University of Hamburg). I was working in the group of Prof. Dr. Christian Klinke. During this period, I worked with tin chalcogenide nanocrystals and reported the results in three manuscripts, from which two of them were published in scientific journals and one of them was still under progress. I also wrote three abstracts (two presented as poster and one presented as oral talk) which were accepted as conference proceedings. All these publications are mentioned below.

Declaration: This dissertation essentially composes of the complemented scientific work which has been published with first authorship by the author of this thesis, Fu LI in the journals: Journal of Materials Chemistry C, and Journal of Physical Chemistry Letters.

■ **Peer-reviewed Papers:**

Fu Li, Mohammad Mehdi Ramin Moayed, Frauke Gerdes, Sascha Kull, Eugen Klein, Rostyslav Lesyuk, Christian Klinke: Colloidal tin sulfide nanosheets: Formation mechanism, ligand-mediated shape tuning and photo-detection. *Journal of Materials Chemistry C*. 6 (**2018**) 9410.

Fu Li, Mohammad Mehdi Ramin Moayed, Rostyslav Lesyuk, Eugen Klein, Christian Klinke: In-plane anisotropic faceting of single-crystalline colloidal SnS nanosheets: towards anisotropic electronic transport. *Journal of Physical Chemistry Letters*. 10 (**2019**) 993.

■ **Under revision:**

Fu Li, Sascha Kull, Rostyslav Lesyuk, Christian Klinke: Colloidal synthesis of two-dimensional narrow-gap semiconductor tin telluride nanostripes and nanosheets. In progress.

■ **Conference proceedings:**

<u>Fu Li</u>, Frauke Gerdes, Sascha Kull, Mirjam Volkmann, Christian Klinke: Shape and Size Control of Bimetallic CoPt Nanoparticles and Ligand Exchange with Chiral Molecules. The 29th GCCCD® Annual Conference -17th Parallel Forum of **2017** CIESC Annual Meeting "Sino-German New Materials Forum". GCCCD® Best Poster Award (1st Price).

<u>Fu Li</u>, nanoGe Fall Meeting (**2018**) - Málaga, Spain, Oral talk: In-plane anisotropic faceting of single-crystalline colloidal SnS nanosheets.

<u>Fu Li</u>, Mohammad Mehdi Ramin Moayed, Frauke Gerdes, Sascha Kull, Eugen Klein, Rostyslav Lesyuk and Christian Klinke: Colloidal Synthesis and Characterization of Tin Sulfide SnS Nanosheets: Formation Mechanism, Shape Tuning and Anisotropic Edge-faceting. NaNaX 9 Conference in Hamburg. Poster presentation.

Content

Abstract

The special size- and shape-dependent properties of two-dimensional (2D) metal chalcogenides such as PbS, CdS, CdSe nanosheets or nanoplatelets have been intensively studied over the past decades. They display fascinating electric and optoelectrical properties, but also high toxicity which limits their further applications. Two-dimensional tin (II) sulfide (SnS) nanocrystals, emerging among all the metal chalcogenides, are now considered as promising less-toxic alternatives. The orthorhombic structure of SnS belongs to layered crystal structures, which endows some advantages for SnS in the synthesis of 2D nanocrystals. In this thesis, a novel colloidal synthesis method is presented, displaying a productive and efficient way to produce colloidal SnS nanosheets with large lateral size and controllable thickness as well as single crystallinity. The synthesis of SnS nanosheets is performed by using tin (II) acetate as the tin precursor instead of harmful precursors like tin chloride or flammable organo-metallic bis[bis(trimethylsilyl)amino] tin (II) precursor. By variation of parameters like capping ligands, it is discovered that the morphology of the synthesized SnS nanosheets can be tuned between square-shaped nanosheets with lateral sizes ranging from 150 nm to nearly 500 nm, and thicknesses from 24 nm to 29 nm with small fluctuation, and hexagonal nanosheets with sizes from 230 nm to 1680 nm and heights between 16 nm to 50 nm. The formation mechanisms of both square-shaped and hexagonal nanosheets are further studied and supported by DFT simulations. In addition, optoelectronic measurements demonstrate the relatively high conductivity and pronounced sensitivity to light (red laser, λ = 627 nm). This implies a good prospect of these synthesized nanomaterials for photo-switching, photo-sensing and photovoltaic applications.

The highly efficient morphology control of such colloidal SnS nanosheets becomes strongly attractive, as large and thin 2D nanosheets are always desirable for nano-scientists. 2D SnS nanomaterials is gathering increasing attention since they exhibit a pronounced in-plane anisotropy in terms of atomic arrangements. The application of such in-plane anisotropy can facilitate the device design, and also strengthen the device performance based on distinct responses to external stimuli conditions such as polarized light or an applied electric field. Thus,

the second task of the thesis is to find proper synthesis conditions for obtaining larger and thinner SnS, as well as tuning the anisotropy regarding the exposed edges. It is found that the change of the sulfur precursor from thioacetamide to trioctylphosphine-sulfur (TOP-S) realizes the goal, which develops an improved recipe. Larger and thinner single-crystalline SnS nanosheets with thicknesses down to 7 nm and lateral sizes up to 8 μm were synthesized. The recipe still involves oleic acid as ligand, with or without TOP as co-ligands. Interestingly, the exposed edges can be tuned either parallel to anisotropic directions (armchair and zigzag) or parallel to isotropic directions ("ladder" directions), which is regarded as edge faceting. This is, so far, the first report on colloidal syntheses of large and thin SnS nanosheets with tunable edge-faceting. Electronic transport measurements also reveal a strong dependency of their electrical properties on the crystallographic directions, which in turn confirms the structural anisotropy.

In contrast, another important tin-based metal chalcogenide, SnTe, owns an isotropic crystal structure (rock-salt crystal structure, with the space group *Fm3m*). It has a mirror symmetry in the Brillouin zone of a face-centered (*fcc*) cubic system. There is an increasing emergence of studies on SnTe nanomaterials due to their remarkable properties. For example, it is a topological crystalline insulator owing to its special crystal symmetry. Furthermore, it is used as mid-IR photodetectors as well as photovoltaic devices because of the narrow bandgap. In this thesis, a novel colloidal synthesis method was developed to acquire large 2D SnTe nanocrystals. By introducing halide alkane 1-bromotetradecane (1-BTD), 2D elongated nanosheets or called nanostripes can be obtained with some byproducts. The thickness of the synthesized SnTe nanostripes can be tuned down to 29 nm and the length can reach approximately 6.0 μm. The nanocrystals display high crystallinity, as can be proven by XRD and SAED. The influence of 1-BTD used in the reaction is also discussed. It is shown that a larger amount of 1-BTD leads to a higher percentage of nanorods compared to 2D nanostripes. The role of halides in the form of halide salts is also investigated by replacing 1-BTD with LiBr or $SnBr_2$. Absorption spectra of SnTe with different nanostructures revealed pronounced absorption features in the IR range.

Zusammenfassung

Zweidimensionale Metall-Chalkogenide wie z.B. PbS, CdS und CdSe Nanoplättchen sind aufgrund ihrer besonderen größen- und formabhängigen Eigenschaften Gegenstand intensiver Untersuchungen. Neben den faszinierenden elektrischen und optischen Eigenschaften dieser Materialien besitzen diese jedoch auch eine hohe Toxizität und krebserregende Eigenschaften, welche die Anwendungsmöglichkeiten stark einschränken. Zinn-Chalkogenide als weniger giftiges Materialien gelten als vielversprechende Alternative und besitzen mit einer Schicht-Struktur günstige Voraussetzungen zur Herstellung kolloidaler 2D Nanostrukturen.

In dieser Arbeit wird eine neue und einfache Synthese von einkristallinen SnS Nanoblättern vorgestellt. Diese Nanostrukturen besitzen große laterale Ausmaße bis in den Mikrometerbereich und können in ihrer Dicke kontrolliert werden. Dabei wird Zinn(II)acetat als Alternative zum giftigen Zinn(II)chlorid oder leicht entflammbaren Organo-Zinnverbindungen eingesetzt. Die Form der SnS Nanoblätter kann durch die Menge an Liganden und weiteren Parametern zwischen quadratischen Nanoblättern (150-500 nm Kantenlänge, 24-29 nm Dicke) und sechseckigen Nanoblättern (250-1700 nm Kantenlänge, 16-50 nm Dicke) verändert werden. Die Entstehung beider Formen wurde intensiv untersucht und in einem Mechanismus zusammengefasst, welcher durch DFT Simulationen unterstützt wird. Die elektrischen Eigenschaften von SnS Nanoblättern wurden untersucht und zeigten mit einer hohen Leitfähigkeit und guten Photostrom vielversprechende Eigenschaften zum Einsatz als Photodiode, Photosensor oder in der Photovoltaik-Technik.

Um die Eigenschaften der SnS Nanoblätter weiter zu optimieren wurde die Möglichkeit lateral größere aber in der Höhe dünnere Nanostrukturen herzustellen intensiver verfolgt. Die Schwierigkeiten liegen dabei in dem Einschränken des Wachstums in einer Dimension bei bevorzugtem Wachstum in der Ebene. Eine Besonderheit von SnS ist die Anisotropie in der Ebene durch die Kristallstruktur, welche für die Anwendung von zusätzlichem Interesse sein kann. So kann der Kristall unterschiedlich auf äußere Stimuli wie polarisiertes Licht und elektrische Felder

reagieren und so zu besseren Eigenschaften führen. Um den Anforderungen an die Anisotropie und Größenkontrolle gerecht zu werden, wurde die Schwefelquelle von TAA zu TOP-S geändert und die Synthese weiter optimiert. Dabei ergaben sich SnS Nanoblätter mit einer lateralen Größe von bis zu 8 μm und einer Dicke von 7 nm. Interessanterweise können die Kanten der Nanoblätter in der isotropen oder anisotropen Kristallrichtung kontrolliert werden, was zuvor noch nicht in der Fachliteratur beschrieben wurde. Der elektrische Tarnsport in diesen Nanostrukturen zeigt die zu erwartende Abhängigkeit von der Kristallrichtung und bestätigt die strukturelle Anisotropie.

Im letzten Abschnitt der Arbeit wird die Synthese von SnTe Nanostrukturen vorgestellt. Während SnSe eine ähnliche Kristallstruktur wie SnS aufweist, ist SnTe mit der kubischen NaCl-Struktur (*Fm-3m*) kein Material mit einer Schichtstruktur. SnTe ist aufgrund der Kristallsymmetrie Gegenstand von Untersuchungen als topologischer Isolator und wegen der geringen Bandlücke im Mid-IR-Bereich in der Photovoltaik. Da in der Fachliteratur keine Synthese von 2D SnTe gefunden werden konnte, musste diese von Grund auf entwickelt werden, um lange zweidimensionale Nanobretter herzustellen. Die zuvor thematisierte Synthese von SnS Nanoblättern wurde abgewandelt und durch den Einsatz eines Halogenalkans ergänzt, um neben Nanodrähten und Nanowürfeln die zweidimensionalen Nanobretter zu erhalten. Diese können mit einer Länge von ca. 6 μm, einer Dicke von 29 nm und hoher Kristallinität hergestellt werden. Der Einfluss der Halogenalkane in der Reaktion wurde intensiv untersucht und eine erste Abhängigkeit festgestellt. Die Absorption von SnTe Nanostrukturen wurde im IR-Bereich untersucht und zeigt interessante Eigenschaften.

Zusammengefasst wurden verschiedene Synthesereihen vorgestellt um zinnbasierte 2D Nanomaterialien kolloidal herzustellen und dabei die Form oder Kristallographie zu kontrollieren. Dabei zeigten sich auch Möglichkeiten die Eigenschaften der Materialien zu verändern und für etwaige Anwendungen zu optimieren.

List of Abbreviations

0D	Zero dimensional
1D	One dimensional
2D	Two dimensional
MBE	Molecular beam epitaxy
CVD	Chemical vapor deposition
EG	Ethylene glycol
PVP	Polyvinyl pyrrolidone
ODA	Octadecylamine
GISAXS	Grazing Incidence Small-Angle X-ray Scattering
TOP	Trioctylphosphine
OA	Oleic acid
CBC	Covalent bond classification
CTAB	Cetyltrimethylammonium bromide
TEM	Transmission electron microscopy
SEM	Scanning electron microscopy
AFM	Atomic force microscopy
HRTEM	High resolution TEM
FFT	Fast Fourier Transformation
SAED	Selected area electron diffraction
EDS	Energy dispersive x-ray spectroscopy
XRD	X-ray diffraction
XPS	X-ray photoelectron spectroscopy
UV-vis	Ultraviolet-visible spectroscopy
FTIR	Fourier transform infrared spectroscopy
TCI	Topological crystalline insulator
OR	Orthorhombic
HMDS	Hexamethyldisilazane

ICDD	International Centre for Diffraction Data
PT	Pseudotetragonal
TOP-S	Trioctylphosphine-S
a-SnS	Anisotropic-SnS
i-SnS	Isotropic-SnS
DFT	Density functional theory
1-BTD	1-bromotetradecane
1-CTD	1-Chlorotetradecane
DPE	Diphenylether
DMF	N, N-Dimethylformamide

List of Figures

List of Tables

Chapter 1   Theoretical Background

"**N**anotechnology is the idea that we can create devices and machines all the way down to the nanometer scale, which is a billionth of a meter, about half the width of a human DNA molecule." This quote from the American physicist Paul McEuen demonstrates the distinguishing feature of nanotechnology and nanoscience.[1] Generally, nanotechnology proceeds based on the creation and application of nanomaterials.[2-11] Nanomaterials created by chemical synthesis have been investigated for decades and have received great attention due to various novel applications, for example, in biomedicine, catalysis and energy storage.[12-15] A nanocrystal is defined as a material or a particle with at least one dimension smaller than 100 nanometers.[16] Colloidal nanocrystals are solution-grown and composed of homogeneous particles with sizes in the nanoscale range which are suspended in liquid (water or organic solvent).[17] Because of their nanoscale size, they can possess unique and impressive electronic, optoelectronic or catalytic properties. The size, shape, element composition, as well as crystalline structure also determine distinguishing properties among different nanocrystals. Thus, the formation of different nanocrystals has been investigated widely in the recent decades with scientists trying to manipulate the morphology of nanomaterials to reach different application goals. That has also accelerated the theoretical studies on the formation mechanism of colloid nanoparticles, which are defined as zero-dimensional nanocrystals with all three dimensions smaller than 100 nanometers.

Generally, the formation of colloidal nanoparticles involves the nucleation process and the growth process. The classical nucleation theory is considered as the simplest and most broadly applied theory which displays an ideal nucleation process for vapor condensation to liquids.[18] It describes a thermodynamic system which prefers to minimize the Gibbs free energy, which can be extended to the crystallization from liquid to solid for nanoparticles as well.[19] The nucleation and growth mechanism of solid nanoparticles were then defined by LaMer burst nucleation, followed by the Ostwald ripening process, leading to the growth of particles.[4, 20] Further theories were developed later to explain other different results of synthesis, for example, the Finke-Watzky mechanism, oriented attachment and intraparticle growth.[21-24] All these described mechanisms will be presented in the following sections, brightening the way of manufacturing nanocrystals with narrower size distribution and variety of morphologies.

1.1 Nucleation and Growth Mechanism for Nanoparticles

The classical nucleation theory was developed for explaining the growth in the vapor phase by Becker and Döring.[25] However, it has also been adapted to study processes in solution. The homogeneous nucleation was explained by Gibbs to describe a thermodynamic process of nucleation, which contains the change of the total free energy ΔG for a droplet as the sum of volume free energy (ΔG_V) and surface free energy (ΔG_S), as shown in Figure 1.1.[26]
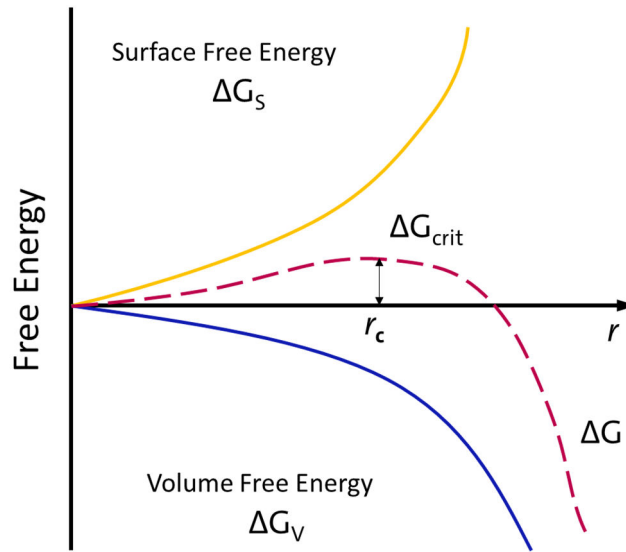
Figure 1.1. Free energy diagram for the nucleation process defined by Gibbs. (Adapted from John W. Mullin,[26] 1997).

The formation of nuclei happens under the competing situation of decreasing ΔG_V and increasing ΔG_S, finally leading to an increase of total energy ΔG to the maximum ΔG_{crit} (called activation energy) at a critical size r_c. The summarized equation is as followed:

$$\Delta G = \Delta G_S + \Delta G_V = 4\pi r^2 \gamma + \frac{4}{3}\pi r^3 \Delta G_v, \tag{1.1}$$

where γ is the interfacial tension and r is the radius of a sphere. ΔG_v is the value of ΔG_V per unit volume. The critical radius can be determined to be $-2\gamma/\Delta G_v$ by solving eq. (1.1) for $d\Delta G/dr=0$. ΔG_v is equal to $-k_B T \ln(S)/v$, where T refers to the temperature, k_B represents the Boltzmann's constant, S is the solution supersaturation, and v is the molar volume.[19]

The critical size is then obtained as:

$$r_c = \frac{2v\gamma}{k_B T \ln(S)},$$ (1.2)

The classic growth was summarized by Tadao Sugimoto in 2001.[27] Particles present certain stagnant fluid layer with the thickness of δ around them, moving around in the fluid according to Brownian motion (see Figure 1.2). The total flux of the solute, defined as J, represents the total flux of monomers which go through a spherical particle with the radius of x. Therefore, it can be written by Fick's First Law as follows:

$$J = 4\pi x^2 D \frac{dC}{dx},$$ (1.3)

where D stands for the diffusion coefficient, C represents the concentration at the distance x. Introducing the parameters including C_b, C_i, C_r, which represent respectively monomer concentration in bulk solution, monomer concentration at the interface of solid and liquid, and particle solubility and integrating $C(x)$ from $(r+\delta)$ to r, based on the stable solute-diffusion condition,[27] we obtain:

$$J = \frac{4\pi D r (r + \delta)}{\delta} (C_b - C_i).$$ (1.4)

Thus, after simplification and approximation by introducing the surface reaction rate k and the molar volume v,[4] it follows that:

$$\frac{C_i - C_r}{C_b - C_i} = \frac{D}{kr} \left(1 + \frac{r}{\delta}\right).$$ (1.5)

The growth-rate equations are as follows:

$$\frac{dr}{dt} = \frac{Dv}{r} (C_b - C_r),$$ (1.6)

$$\frac{dr}{dt} = kv\,(C_b - C_r), \tag{1.7}$$

$$\frac{dr}{dt} = \frac{Dv\,(C_b - C_r)}{r + D/k}. \tag{1.8}$$

They all explain the particle size change under certain circumstances: for example, diffusion is the limiting parameter (eq. (1.6)), the surface reaction is the limiting parameter (eq. (1.7)), or neither is the factor controlling the particle growth (eq.(1.8)). Therefore, the growth rate is mainly determined by D and k. If $kr \gg D$, the reaction is diffusion-controlled, while the surface reaction is the determining component if $kr \ll D$.
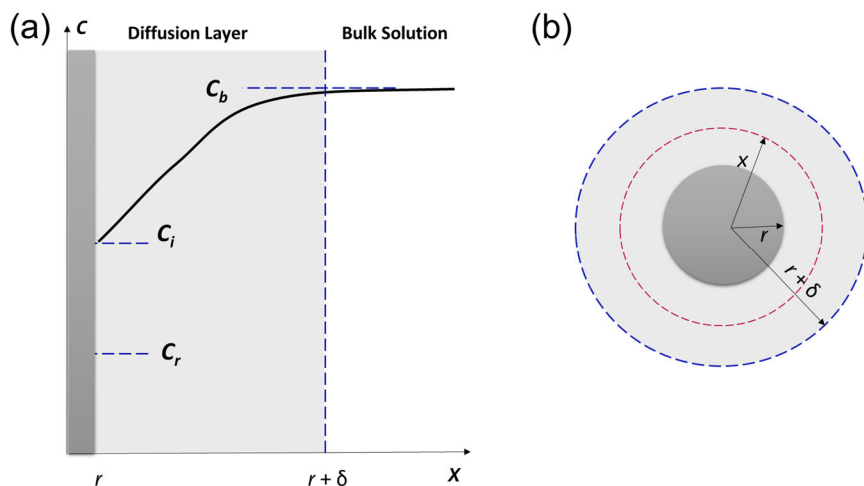
Figure 1.2. Schematic diagrams of microscopic (a) and macroscopic features of the diffusion layer structure starting from the surface of a particle (b). The plot in (a) displays the monomer concentration as a function of distance x from the particle surface. (Adapted from Tadao Sugimoto,[27] 2001).

1.1.1 LaMer and Dinegar Theory

Nucleation and growth were explained by Victor K. LaMer and Robert H. Dinegar.[20] Their theory is established from a process of preparing a monodispersed sulfur hydrosol (see Figure 1.3). It is realized by the slow decomposition of dilute sodium thiosulfate ($Na_2S_2O_3$) in the solvent of dilute

hydrochloric acid (HCl). Under the acidic pH condition, $HS_2O_3^-$ can be produced in the solution. Then, the molecularly dissolved sulfur and bisulfite ion can be produced, and the equation is written as:

$$2HS_2O_3^- = 2HSO_3^- + S_2 \qquad (1.9)$$

The whole mechanism can be explained by the following three stages: (I) the sulfur concentration increases and then reaches the critical supersaturation level C_0 (see Figure 1.3). At this stage, the solution is in a metastable state, while no nucleation occurs yet;[19] (II) the saturation increases and reaches a second level C_k, where the activation energy for nucleation can be surmounted. Then the rapid self-nucleation starts.[28] With the time goes, the monomer concentration reaches the critical limiting supersaturation. The nucleation then continues, consuming the monomers, partially relieving the supersaturation. Thus, the curve starts to drop (see Figure 1.3); (III) the concentration reduces below C_k. The nucleation process ceases, and the growth stage starts. The growth of stable formed nuclei finally leads to discrete particles via the combination of dissolved sulfur into the nuclei seeds.[19]
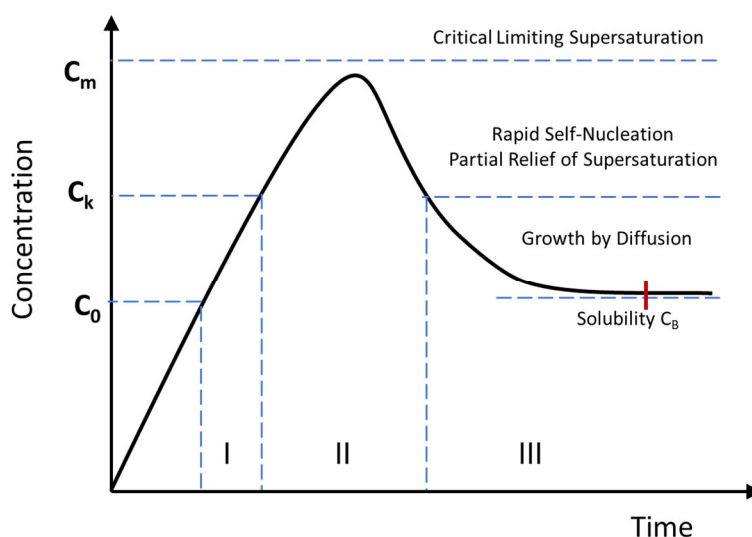
Figure 1.3. Graphical representation of the LaMer theory: the sulfur concentration as a function of the time parameter. (Adapted from LaMer and Dinegar,[20] 1950).

The LaMer and Dinegar theory describes the nucleation and growth of solid nanoparticle

syntheses. It describes both processes in terms of monomer concentration, and it is also the basis to explain the hot injection method theoretically by separation of nucleation and growth for obtaining mono-dispersity.

1.1.2 Ostwald Ripening Theory

A. P. Alivisatos *et al.* reported the focusing of the size distribution for CdSe and InAs nanocrystals by tuning the amount of injected precursor.[29] There should be a critical size at which the system is in equilibrium with any monomer amounts. Thus, nanoparticles in the synthesis smaller than the critical size will dissolve, resulting in negative growth rates, and larger nanoparticles grow at rates related to their sizes. When all the nanocrystals in the solution have larger sizes than the critical size, the size distribution starts "focusing".[29] Smaller nanocrystals will grow quicker than larger ones since less mass is needed to complete additional layers on nanocrystal surface. Through the consumption of monomer concentration, the critical size increases. Small nanocrystals then start to lessen or even vanish, while larger ones grow even bigger. This is a common phenomenon called Ostwald ripening, which causes "defocusing" of the size distribution. With the injection of additional monomers, the critical size remains small, leading to a system in the size focusing regime.

Ostwald ripening was described by Wilhelm Ostwald in 1890s[30] and demonstrates the dissolution of small particles, while larger particles grow bigger (see Figure 1.4). This ripening process is due to the requirement of the maximum of thermodynamical stability, making the surface to area ratio minimal. The energetical stabilities of molecules on the particle surface are lower than those of molecules inside the particle. Thus, surface molecules frequently escape into the solution, resulting in an increase of free molecules floating in the solution, and also a decrease of original particle size (see Figure 1.4). However, the solution becomes supersaturated via the addition of escaping molecules from shrinking particles into solution. Then those free molecules start to deposit again on the particles, but on the larger particles instead of small sized particles. Therefore, the small particles in solution become smaller in size until they vanish, while large particles grow even bigger.
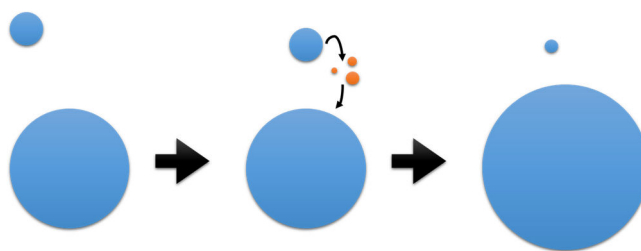
Figure 1.4. Graphical representation of the Ostwald ripening: small particles become smaller until disappearing while large particles grow bigger according to energetical stability difference between the surface and the interior of particles. (Adapted from Wilhelm Ostwald,[30-31] 1896).

In addition, Prasad *et al.* reported that a colloidal suspension was refluxed at the temperature of the solvent's boiling point with the existing ligands, transforming a colloid with high polydispersity into a monodisperse colloid by breaking the polydisperse colloid into small-sized particles with the help of ligands, followed by the isolation of the colloid from the byproduct.[32-33] This process is called digestive ripening, which is also another ripening process to achieve colloidal nanoparticles.

1.1.3 Aggregative Growth Theory

Aggregative growth is the proposed process for non-classical nucleation and growth procedures.[34] Alivisatos' group reported the growth process of Pt nanoparticles via *in situ* transmission electron microscopy (TEM).[35] The growth trajectories were tracked under TEM after the induction of an electron beam into the reaction cell, leading to the growth of Pt nanoparticles. Furthermore, it was found that the coalescence during growth is site-selective, and it reshapes the structures as well as it rearranges the surface by orienting the facets.[36] The first step C, which refers to the period of classical nucleation and growth process, will witness the generation of initial nanocrystals with ultra-small size. Step A follows, where the aggregative nucleation and growth process take place. Finally, Ostwald ripening happens after the aggregative process, which was the period named OR step (see Figure 1.5). However, these three steps may happen at the same time and result in the two-peak size distribution.[34] The aggregative growth process and

Ostwald ripening both produce larger sized nanocrystals, whereas these two processes can also be distinguished based on the crystallinity of cores. Nanocrystal products grown mainly by Ostwald ripening can only present one crystalline domain, owing to the growth from the addition of primary nanocrystals with single crystallinity. Nevertheless, formed nanocrystals grown mainly by aggregative pathway should be not of single crystallinity, according to the growth mechanism for the aggregative growth process. Polycrystallinity will then disappear on account of recrystallization over longer time, to finally present multiply twinned structures or still polycrystal structures.[34]
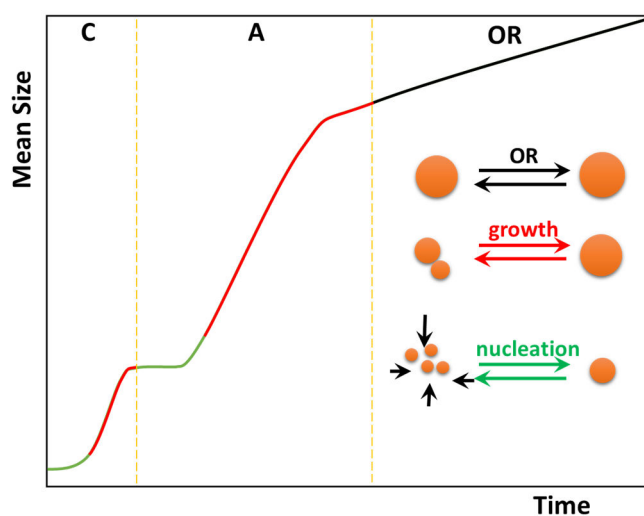
Figure 1.5. Graphical representation of the growth process of nanocrystals including the classical nucleation and growth (step C), aggregative growth (step A), and Ostwald ripening process (step OR). (Adapted from Fudong Wang,[34] 2013).

1.1.4 Finke-Watzky Two-Step Mechanism

In contrast, the Finke-Watzky two-step mechanism contains simultaneous nucleation and growth processes.[21] At first, a slow consecutive nucleation process takes place, followed by the autocatalytic surface growth without diffusion involved (Ir nucleus in their case, see Figure 1.6). For instance, monomers combine to form dimers, and dimers will then combine with another monomer to grow bigger.[37] The autocatalytic growth involves the reduction of iridium ions to iridium atoms accompanied by the oxidation of cyclohexene into cyclohexane. This mechanism

is normally applied to explain the formation mechanism of metal nanoparticles.
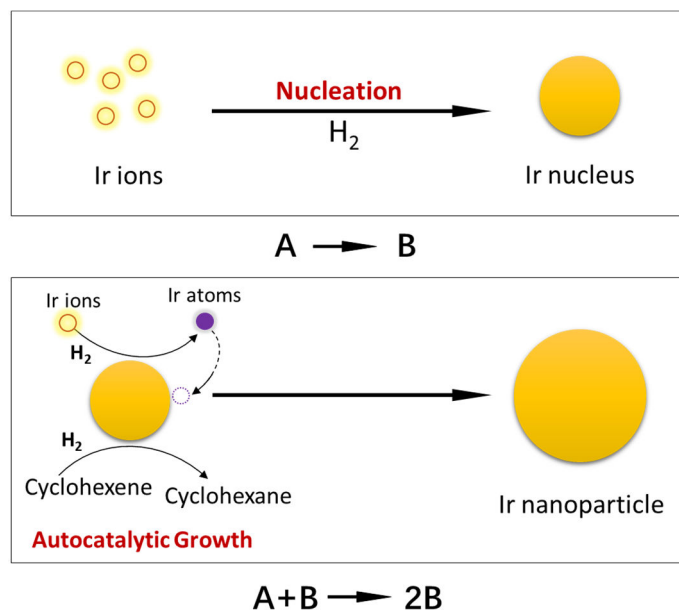
Figure 1.6. Graphical representation of the Finke-Watzky two-step mechanism. (Adapted from Siva Rama Krishna Perala,[37] 2014).

1.1.5 Oriented Attachment

The oriented attachment theory was first raised by R. Lee Penn and Jillian F. Banfield in 1998.[38] The system whose growth is based on oriented attachment has neighboring small particles formed at the beginning, followed by self-assembly with aligning the crystallographic ordering between two particles. The attachment process is driven by the minimization of the surface free energy of the whole system to reduce the amount of high energy surfaces.[39-40]

Basically, this is a growth mechanism which requires a wet-chemical synthesis environment, involving free-moving nanoparticles which later diffuse to meet each other. The attachment of two close particles will collude and adjust their orientation. Afterwards, re-ordering is needed for nanoparticles in order to proceed recrystallization, followed by the subsequent reducing of grain boundaries. Ultimately, a combination of nanoparticles into one single nanocrystal will occur (see Figure 1.7). It has been proved that oriented attachment is a good way to form anisotropic nanostructures no matter whether the crystal system is symmetric or asymmetric in certain

dimensions where symmetry-breaking is needed. The outstanding example of oriented attachment process is the colloidal synthesis of two-dimensional PbS nanosheets by oriented attachment with the assistance of halogenated compounds.[24]
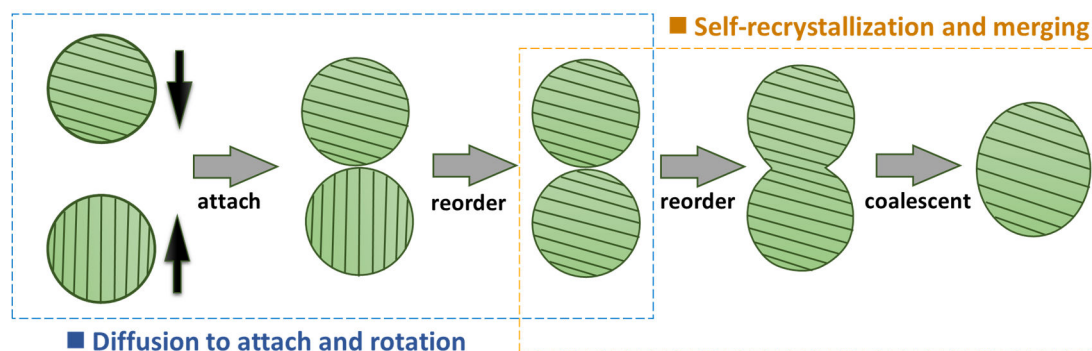
Figure 1.7. Graphical representation of the basic mechanism of oriented attachment process during growth. (Adapted from Michel Nasilowski,[39] 2014).

1.1.6 Intraparticle Growth

The intraparticle growth (or intraparticle ripening) was described by X. Peng.[41] They investigated the synthesis of gold flowers and observed the shape-changing in an intraparticle manner: it happens inside the particles without the interparticle way. The monomers diffuse towards the surface of particles to transform nanoparticles into another shape. Cl$^-$ ions play an important role in the intraparticle growth of these gold flowers, by binding to Au atoms on particle surfaces, along with promoting the movement of Au atoms.[41]

1.2 Two-dimensional Nanocrystal Synthesis

Basically, nanocrystals will grow towards the direction that the surface energy is reduced. Thus, the final shape is influenced by every crystal facet.[39] This is summarized already by Wulff as a simple construction method for equilibrium-shape determination.[39, 42] The final shape will not always be spherical. It depends on the colloidal synthesis environment (*e.g.* ligands) and

symmetry in the nanocrystal itself. Recently, two-dimensional (2D) colloidal nanocrystals have been investigated widely for new or improved properties compared to zero-dimensional (0D) and one-dimensional (1D) nanocrystals. 2D nanocrystals are also known as "quantum wells", where only one dimension is in the nanoscale range.[43] The advantages of this shape anisotropy of 2D nanocrystals have resulted in various intriguing applications in various research fields including electronics, catalysis, biomedicine, and energy storage.[44-46] Here, typical mechanisms for the formation of 2D nanostructures will be summarized.

1.2.1 Synthesis Methods

Cubic crystal symmetry (e.g. PbS) should prefer a cubic shape. However, suitable ligands and temperature conditions can lead to a 2D nanostructure for these non-layered nanomaterials.[24] Symmetry-breaking would be the key reason for this phenomenon. In contrast, a layered crystal system naturally prefers to form a 2D nanostructure. Therefore, one important factor for obtaining 2D nanocrystals originates from the crystal structure type. Here, we would like to demonstrate the different synthesis methods for achieving 2D nanostructures based on the colloidal synthesis conditions and the symmetry.

1.2.1.1 Layered Crystal Systems

Typical 2D layered materials include graphene, metal chalcogenides (IV-VI and III-VI layered compounds like SnS, GeS), metal dichalcogenides such as MoS_2 and some metal oxides like WO_3.[47-50] These nanomaterials present layered structures, which involves van der Waals interactions between upper and lower layers, and much stronger covalent bonds between atoms inside the layers. Owing to this special crystal structure, the favorable shape will be two-dimensional, which is promising for 2D nanomaterial preparations and applications. There are several preparation methods for layered material syntheses. For example, there are chemical vapor deposition (CVD), molecular beam epitaxy (MBE) or mechanical exfoliation.[51-53] So far, many feasible methods have been investigated, including liquid exfoliation, selective etching, ion-

intercalation, and the colloidal method (wet-chemical synthesis).[54-56] Basically, those methods can be classified into bottom-up and top-down methods. The top-down approach proceeds by the exfoliation of bulk materials with layered crystal structure into several layers of nanoscale materials, during which the breaking of stacked layers happens. The bottom-up approach is usually conducted by the direct synthesis of 2D nanostructures under certain precise reaction conditions, such as proper surfactants or temperature. Examples of this method include the colloidal synthesis method and CVD.[49, 57-58]

1.2.1.1.1 Exfoliation Method

Different exfoliation approaches include mechanical exfoliation, liquid exfoliation, and ion-intercalation.[59] A typical way to proceed the mechanical exfoliation approach was discovered by Geim *et al*. who exfoliated the bulk materials by applying adhesive Scotch tapes to obtain ultrathin 2D crystals.[60] After obtaining the thin layers of 2D nanomaterials on the tape, the transfer from Scotch tape to a substrate by a tweezer is conducted. Because of some drawbacks of mechanical exfoliation such as low productivity, liquid exfoliation was also developed to make large quantities of exfoliated nanosheets.[61] One example for this method is the preparation of graphene oxide from graphite. Graphite is treated with sulfuric acid or potassium permanganate as oxidizers. This is to modify the exposed facets with hydroxyl and epoxide groups which are perfect groups for water intercalation and to obtain graphene oxide via ultrasonication as the last step.[62] The ion-intercalation process involves the insertion of ions into the layers of 2D layered nanostructures, leading to the weakening of layer-layer van de Waals interactions. 2D nanostructures can be obtained later after a sonication step to split each layer.[63] Some commonly used intercalators are metal naphthalenides such as sodium naphthalenide.[64]

1.2.1.1.2 Chemical Vapor Deposition Method

The chemical vapor deposition or CVD method belongs to the bottom-up approaches. This method normally involves precursors which react with each other to form the product under high temperature and high vacuum condition in a reaction chamber and a substrate where the product will be deposited.[49, 65] Compared to the exfoliation methods, CVD can produce well-shaped highly crystalline 2D nanostructures. However, the extreme reaction condition brings

difficulties to the further development and applications of the CVD method.

1.2.1.1.3 Wet-Chemical Synthesis Method

Compared to the CVD method, the wet-chemical synthesis method is widely applied by chemical and physical-chemical scientists.[49, 58, 66] This method involves standard chemical reactions which are applied in solution with the usage of certain reactive precursors and surfactants. Thus, colloidal methods for 2D nanomaterial preparation produce 2D nanomaterials in solution, assisted by ligands and a suitable temperature to control the crystal growth. The preparation after synthesis such as deposition on substrates is convenient for further applications.[49] In addition, the highly controllable shape tuning and size tuning are also promising for industrial production.

a) *Hydro/solvothermal Method*

The hydrothermal synthesis method is one common wet-chemical synthesis method. It is performed in a closed vessel (autoclave), in which all the reactants are dissolved in hot water. Thus, the solubility of reactants in hot water under high pressure becomes one of the important factors which will define the whole reaction conditions.[67-69] Meanwhile, it requires the vapor pressure of the material near the melting point to be high enough for the high-pressure reaction. The solvothermal synthesis method differs only in the solvent: the solution is non-aqueous in the solvothermal synthesis case.[70-71] The synthesis of Bi_2Te_3, MoS_2, and SnS 2D nanosheets have been investigated using the hydro/solvothermal method to obtain high crystallinity and well-shaped morphologies.[68, 70-71] For instance, Bi_2Te_3 single-crystal nanosheets with highly uniform morphology were prepared by a facile solvothermal route.[70] The solvent used for this solvothermal method is ethylene glycol (EG), which also acts as the reducing agent for the reduction of Te precursors (Na_2TeO_3). The optimized temperature is 180 ℃ and the thickness of the Bi_2Te_3 nanosheets can be tuned by the adjustment of the NaOH concentration. A high concentration of OH^- ions from NaOH, which can facilitate the release of cations, accelerates the anisotropic growth of different facets. Polyvinyl pyrrolidone (PVP) also plays an important role in the formation of Bi_2Te_3 nanocrystals, by serving as a surfactant to achieve a defined shape.[70] Furthermore, morphology and growth mechanism studies show that the solvothermal synthesis

of Bi_2Te_3 mainly goes through three phases. Firstly, the monomer concentration in the reaction system is initially high, resulting in the 2D growth tendency. Then, the reaction keeps consuming the monomer, leading to a quick decrease in the monomer concentration. This helps to switch the growth from 2D-growth behavior to 3D-growth behavior. Thirdly, the growth of Bi_2Te_3 nanocrystals starts to stagnate and ripening starts. Thus, the shape of Bi_2Te_3 nanocrystals starts from thin hexagonal nanosheets to thicker nanosheets (see Figure 1.8). These three phases are all diffusion-controlled and the solvent EG presents a high surface tension, which gives the formation for Bi_2Te_3 nanosheet a better equilibrium growth condition.
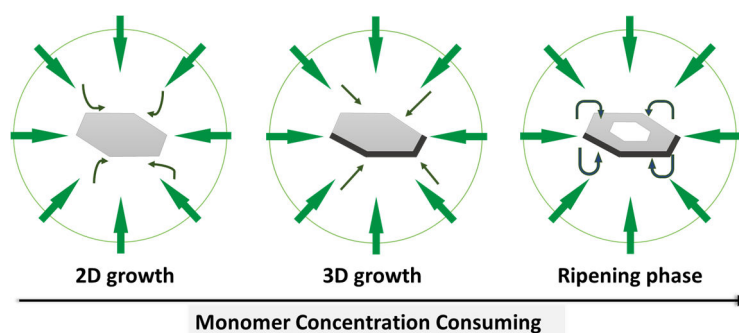
Figure 1.8. The three main growth phases of Bi_2Te_3 nanocrystals in the solvothermal synthesis method in the period of monomer consumption. (Adapted from Y. Zhao,[70] 2013).

b)   Soft-templated Method

The soft-templated method for 2D nanomaterial preparation normally involves ligands as templates. Ligand templating plays a vital role in the formation of either layered or non-layered 2D nanosheets.[72-73] The ligand templates normally act as the scaffold to shape the anisotropic nanocrystals which present the structures complementary to those of templates.[74] The syntheses with the aid of ligands have been investigated to produce various layered nanocrystals with different nanostructures, such as Sb_2S_3 nanospheres,[72] Bi_2S_3 nanorods,[75] InSe nanosheets.[76] For instance, hexagonal ultrathin InSe nanosheets reported by Lauth *et al*. are also prepared by the soft-templated method.[76] They introduced amines (octadecylamine, ODA) as lamellar soft templates. They can lead to the formation of 2D InSe nanosheets (see Figure 1.9a). The nanostructures are measured by Grazing Incidence Small-Angle X-ray Scattering (GISAXS) and the result displays a scattering periodicity of the distance between two layers of 4.4 nm. This

distance includes the length of ODA ligands (approximately 1.7 nm) and the thickness of the InSe layer (approximately 1 nm).[76] This solution-based soft-templated process is very promising for layered nanomaterial syntheses with controllable thickness and well-defined lateral shape. Meanwhile, the oriented attachment mechanism sometimes also participates in the synthesis together with the soft-templated method.[66]
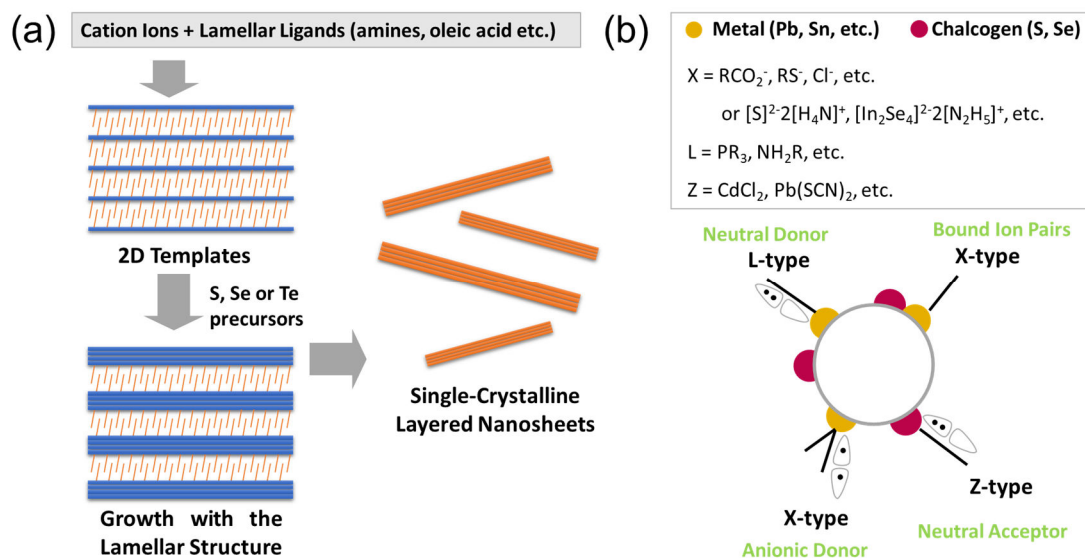
Figure 1.9. (a) Schematic illustration of the formation of layered nanosheets with the aid of lamellar ligands such as amines or oleic acid. (Adapted from Jannika Lauth,[76] 2016, and Jae Sung Son,[77] 2009). (b) Different types of surface ligands coordinating with specific atoms on the surface. (Adapted from Jonathan Owen,[78] 2015).

It is well known that surfactants, or ligands play a vital role for colloidal synthesis.[78-79] Theoretically, ligands are classified into three types, such as X-type, L-type and Z-type ligands according to the covalent bond classification (CBC) method (see Figure 1.9b).[80] Specifically, L-type ligands including phosphine molecules or long-chain amines are defined as neutral donors owning free electron pairs, which can attach to the metal ions on the crystal surface.[79] Z-type ligands contain electron-pair acceptors which are neutral, for example, $CdCl_2$. This type of ligand is suitable to coordinate to negative-charged ions on the crystal surface. In addition, X-type ligands are defined as anionic donors including negative-charged ligands such as RCO_2^- or halide ions which can attach to the cationic metal ions on the crystal surface (see Figure 1.9).

c) *Hot-injection and One-pot Heating-up Method*

The key difference between the hot-injection and one-pot heating-up method is the way to introduce precursors. The precursors in the hot-injection method are introduced by a high-temperature injection, while all the reaction materials including all the precursors are initially mixed in the reaction flask and heated up to the specific reaction temperature in the one-pot heating-up method.[66] Actually, the critical hot-injection approach is not only about performing injection at high temperatures, but also about the control of nucleation. By adjusting the injection volume, the temperature drop can be controlled, resulting in a short nucleation process, followed by a rapid cool-down step. The high temperature triggers fast nucleation with a high monomer concentration and the growth starts subsequently with the aid of present ligands. The hot-injection method has already been applied to introduce second precursors for various reactions, such as the synthesis of InSe, Bi_2Te_3, and SnSe nanocrystals.[81-83]

The one-pot synthesis method is a simple feasible approach with all the reaction materials mixed in the reaction flask at room temperature or at low temperature, followed by a gradual heating process until the reaction temperature is reached. It slows down the speed of nucleation and the speed of the precursor consumption as well. The growth process will happen simultaneously during the heating process, which does not separate the nucleation and growth processes.[84] Plenty of layered nanomaterials have also been investigated with the one-pot heating-up method to produce crystalline nanosheets such as GeSe and GeS nanosheets.[84-85]

1.2.1.2 Non-layered Crystal Systems

Since the layered crystal system brings advantages to the syntheses and applications of 2D nanostructures, great effort has been made to prepare layered nanomaterials. However, non-layered materials, for example, lead halide perovskites, metals such as Co, Ag and Rh, metal oxides like ZnO and SnO_2, metal chalcogenides or dichalcogenides including CdTe and $CoSe_2$, are also widely investigated by nano-scientists.[86] Non-layered nanomaterials with 2D structures can be perfectly complementary to 2D layered nanomaterials based on their specific crystal structures and related properties. Different from 2D layered nanomaterials, non-layered

nanomaterials are filled with dangling bonds, which ensures their chemical active surfaces are always available, yielding the promising applications like catalysis.[87] The specificity of the non-layered nanomaterials is initially defined by the crystal structures. For instance, cubic crystal systems contain strong chemical bonds towards all the three dimensions. Energy differences between different crystal facets normally drive the growth directions, leading to specific morphologies if the synthesis is only thermodynamically controlled or dominated. The reason for this phenomenon is the crystal-structure symmetries of these nanomaterials. For instance, bulk PbS nanomaterial shows cubic phase (rock-salt type), which means it naturally grows into cubic shape under thermodynamic conditions. Therefore, the thermodynamic equilibrium state needs to be disturbed, as well as the symmetry needs to be broken, if 2D nanostructual PbS nanocrystals are expected.[88]

There are several synthesis methods for non-layered nanomaterials according to their special crystal structures, including the CVD method as a gas-phase method, as well as wet-chemical methods.[89-90] Wet-chemical methods have been investigated widely and have become promising strategies for achieving a variety of 2D non-layered nanomaterials. It has several advantages, such as low costs, high productivity and shape/size control. According to the nucleation-and-growth mechanism difference, wet-chemical methods can also be classified into several sub-methods including the templated synthesis, the solvothermal method, and the surface-energy-controlled synthesis method which are similar to those for layered nanomaterial synthesis,.[77, 89] Here, some typical examples of these common synthesis methods to obtain 2D non-layered nanomaterials will be demonstrated.

Templated synthesis methods are popular in the preparation of 2D non-layered nanomaterials with their special crystal structures, which often need certain driving forces for the anisotropic growth.[77, 91] There is a typical synthesis case based on a templated synthesis method. That is the synthesis of ultrathin PbS nanosheets by oriented attachment and by a templating strategy.[24] In detail, oleic acid is used as ligands and is densely packed on the {100} facets as templates, assisting the attachment of PbS crystals and leading to lateral growth. Meanwhile, chlorinated cosolvents also assist the attachment process, adjusting the nucleation and growth rates by forming lead complexing agents (see Figure 1.10).
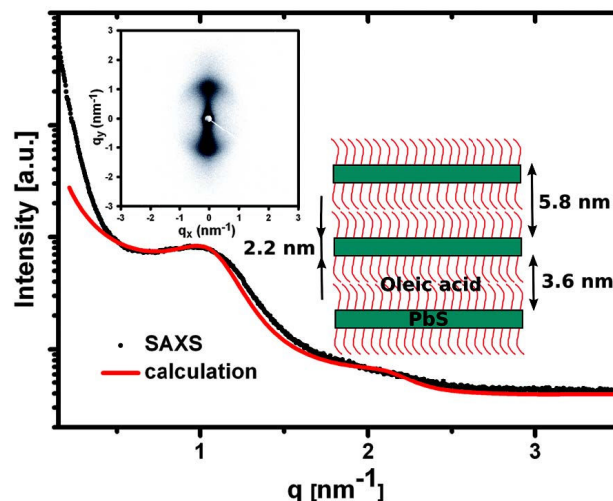
Figure 1.10. Small-angle-X-ray scattering (SAXS) measurement (black) and the simulated diffraction curve (red) of the stacked PbS layers to clarify the nanosheet thickness and the orientational distribution. The scattering image is in the inset, showing anisotropic dumbbell-shaped pattern which displays sheet orientation parallel to the q_x direction. The best simulation fit assumes a PbS sheet thickness of 2.2 nm and a layer thickness of 3.6 nm containing two oleic acid layers. Reproduced with permission.[24] Copyright 2010, AAAS.

The solvothermal method is also one typical strategy to synthesize 2D non-layered nanostructures.[92-93] A representative example is the reported solvothermal synthetic route to prepare anatase TiO_2 nanosheets by applying 2-propanol as capping agent as well as reaction solvent in the presence of hydrofluoric acid (HF).[92] The used 2-propanol and fluorine can respectively stabilize the facets and lower the surface energies of the (100) facets, leading to the final 2D nanosheet morphology. Under HF treatment, 2-propanol presents alkoxy group $((CH_3)_2CH\text{-}O^-)$ to bind to crystal surfaces via attaching to Ti^{4+} ions, impeding the growth towards the direction [001]. The final 2D morphology is considered as a thermodynamically favored nanostructure.

The surface-energy-controlled growth method normally involves some surfactant agents including polymers or gas molecules, which can preferably attach to specific crystal facets, resulting in a decrease of the growth rate of these facets and anisotropic growth of products.[91, 94] Huang *et al.* reported a general growth method to prepare free-standing hexagonal palladium nanosheets.[94] The surfactants used in this work are poly(vinylpyrrolidone) (PVP) and halide salt-cetyltrimethylammonium bromide (CTAB), in the presence of the active gas molecules CO. The

CO molecules attach to the (111) facets of palladium crystals, which hinters further growth along the corresponding [111] direction (the thickness direction). Therefore, CO guides the 2D growth of palladium nanocrystals.[94] The growth can be proved as surface-energy-controlled growth according to the TEM images, which show the increase of edge length and no change of thickness during the reaction. PVP is found to be necessary for the reaction, serving as a capping agent to prevent nanocrystals from agglomerating (see Figure 1.11).
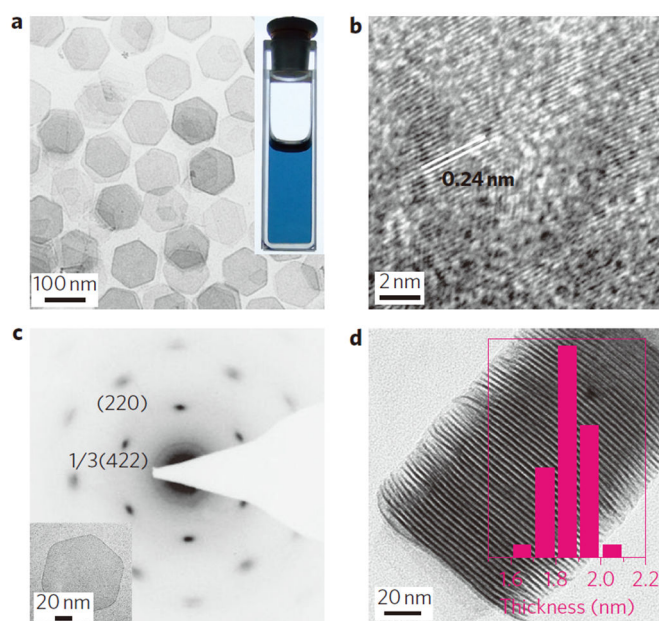
Figure 1.11. TEM characterization of ultrathin palladium nanosheets produced with the aid of PVP and CTAB in the reaction. Reproduced with permission.[94] Copyright 2011, Nature Publishing Group.

1.2.2 Characterization Methods

There are some common characterization methods to evaluate the morphology, the physical or the chemical properties of synthesized 2D nanosheets.[95-96] For instance, there are several microscopy-based characterization methods such as transmission electron microscopy (TEM), scanning electron microscopy (SEM), atomic force microscopy (AFM). These techniques can provide information about the nanomaterials: size, shape and even crystal structure information from TEM (sometimes high-resolution TEM (HRTEM) measurements are needed for clear lattice

fringes); morphology, thickness and elemental distribution from SEM; thickness and surface roughness from AFM.[95] Other information concerning crystal structure and elemental composition can be obtained by X-ray diffraction (XRD), and the physical or chemical properties *e.g.* optical properties can be measured by spectrometers.

1.2.2.1 Transmission Electron Microscopy Characterization

In a typical Transmission Electron Microscopy (TEM), high energy electrons transmit through a thin sample. The electron beam interacts with the sample on a TEM grid and the obtained images are generated based on the detected diffracted electrons through the sample. Transmitted electrons are collected and detected by the detectors. Then the data are transformed to final images by the software. The final images contain information about the size and shape distribution, as well as rough estimate of the thickness distribution according to the contrast compared to the background. A simple sketch of a TEM set-up (see Figure 1.12) shows its basic components including an electron source (electron gun), condenser lens and objective lens, projective lens and phosphor screen or another imaging device.[96] Basically, electrons are generated by heating a filament (e.g. tungsten filament) or by using field emission.[97] By applying a condenser lens, the electron beam can be focused to hit the sample on the TEM grid. The transmitted electrons through the grid are broadened and then focused again by an objective lens. After passing through the intermediate/projective lens, the final image of the sample on the phosphor screen (or CCD) can be formed with certain magnification ranging from 100x to even 10^6x (see Figure 1.12).
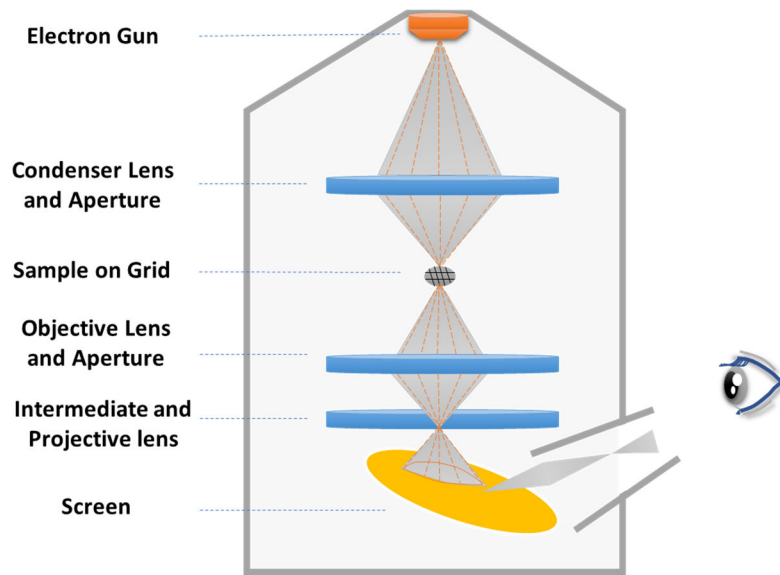
Figure 1.12. Schematic representation of the set-up inside a TEM (Adapted from Kourosh Kalantar-zadeh and Benjamin Fry,[96] 2008).

Therefore, darkness in the obtained image represents how much the electron portion is diffracted. The background is lighter than the nanomaterials because of more electrons are transmitted through the areas without the covering of samples (see Figure 1.11). That is why we can roughly tell the relative thickness from the contrast: the darker the contrast, the thicker the sample.

a) High-resolution TEM

High-resolution TEM (HRTEM) is one special and powerful imaging mode of TEM characterization to check the detailed crystal structure of nanomaterials. The final HRTEM images are formed based on the phase contrast which results from the interference of the electron wave.[47, 98] As the electron wave strikes onto the surface of the sample, most of electrons will penetrate through the sample. Apart from the transmitted electrons, scattered ones or diffracted ones are also formed during the transmission, leading to the change of the electron phase.[99] All these electrons then interact with atoms inside the sample, displaying interference patterns of the final image, as described by Bragg diffraction. Therefore, HRTEM measurements give information about crystal fringes of detected facets and measurement of the distance of two planes can determine the specific facets (see Figure 1.13).[100]

Corresponding to HRTEM images, the Fast Fourier Transformation (FFT) on the images presents well-ordered points which display a Miller plane, showing the information in reciprocal space of the detected crystal.[101] Each point refers to a specific facet of the crystal, which also matches the analysis of crystal fringes from TEM measurements (see insets from Figure 1.13e, d, f).

b)   Selected Area Electron Diffraction

Selected area electron diffraction, also called SAED or SAD, is defined as a microscopy technique based on the TEM instrument. In the TEM pathway, atoms inside the sample act as diffraction gratings to the electrons. The SAED patterns can be obtained after the diffraction, displaying a set of diffraction patterns owing to the specific crystal structure of the measured sample (see Figure 1.13c).[100] We can clarify the corresponding facets with the measurement of certain distances of spots. Furthermore, the specific exposed facets of the real sample in the TEM image can also be determined if the rotation angle is known between the SAED pattern and the final TEM image.
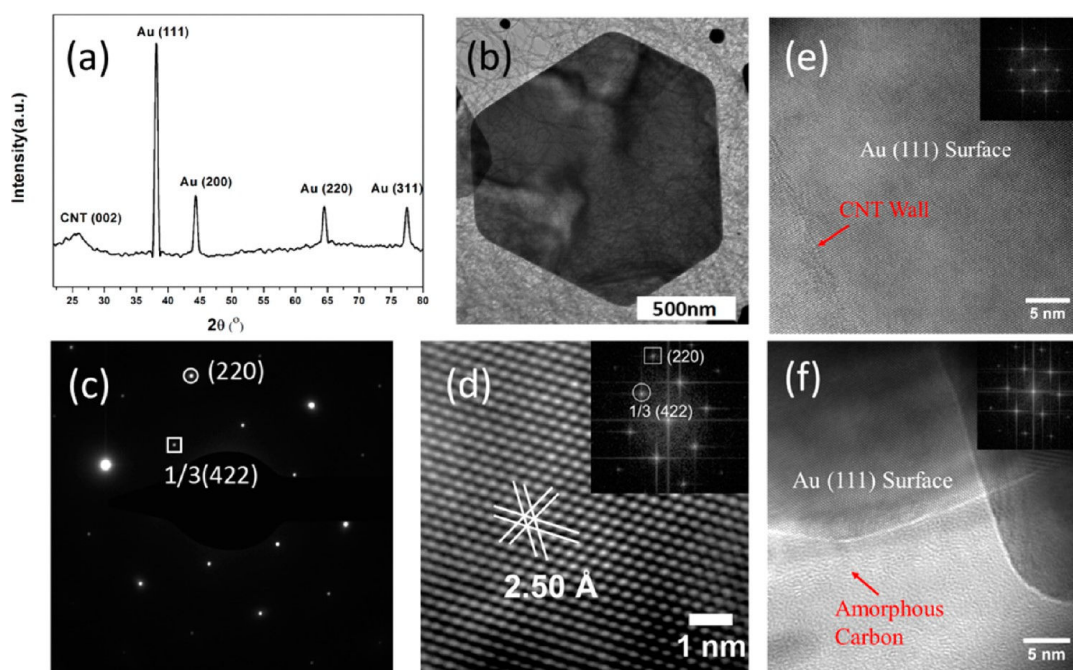
Figure 1.13. The XRD (a), TEM (b), SAED (c), and HRTEM measurement (d-f) on Au nanoplatelets. Reproduced with permission.[100] Copyright 2017, American Chemical Society.

c) *Energy Dispersive X-ray Spectroscopy*

Energy dispersive X-ray spectroscopy (EDS) is another technique inside a TEM (and also a SEM) to characterize the composition of the detected samples by their interactions with the incident electron beam. EDS contains three basic components including an X-ray detector, a pulse processor and a multiple channel analyzer.[102] The incident beam ejects electrons in certain energy positions, leaving holes which other outer electrons from a higher-energy shell can fill, creating X-ray radiation. Therefore, characteristic X-rays can be evaluated by energy-dispersive spectrometer, demonstrating the elemental composition of the sample.[102] Thus, we can get information about the elemental distribution (*e.g.* Pb: S atomic ratio) from EDS analysis.

1.2.2.2 Scanning Electron Microscopy Characterization

The resolution limitations of eyes (0.2 mm) and normal optical microscopes (500-1500x) pushed the development of scanning electron microscopy (SEM). The SEM is used to characterize smaller features based on the electrons which have a much shorter wavelength than that of visible light.[103] It is normally composed of several basic components including an electron source (electron gun), all the needed lenses, specific detectors for different kind of electrons emitted from the specimen, as well as a software for image display (see Figure 1.14).[104] The interaction between the electron beam and the sample produces X-rays, Auger electrons, secondary electrons, primary backscattered electrons, and cathodoluminescence (see Figure 1.15), each of which displays different information about the sample.

Secondary electrons are produced by the inelastic interactions between the primary electron beam and the specimen.[105] They normally appear near the surface of the sample with a distance of 5 to 10 nm, showing high sensitivity to the surface morphology of nanostructures. Therefore, secondary electrons are normally used to display the final images for SEM characterization.[106] When the electron beam hits the surface of the sample to create a hole, another electron from the outer shells fills this empty energy position, producing characteristic X-rays. Auger electrons are created when the outer electrons are ejected by the energy from an electronic transition process of a high-energy electron falling in the vacancy located in the inner shell.[107] This usually

happens in the depths of several nanometers below the sample surface. Cathodoluminescence can be emitted if the electrons and holes recombine.[108] Backscattered electrons are defined as the primary electrons which rebound back by the atom nucleus. They can also be used to display images for SEM characterization.
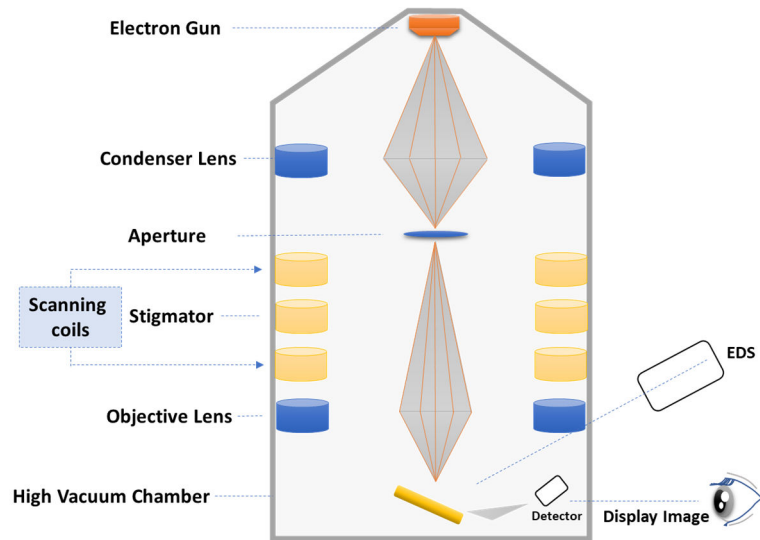
Figure 1.14. Schematic representation of SEM set-up. (Adapted from Tahani Flemban,[109] 2017).
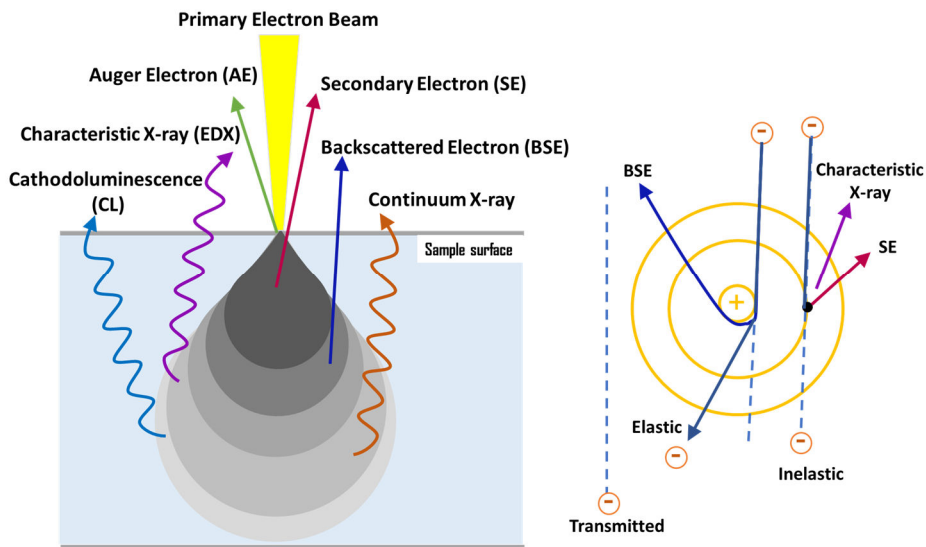
Figure 1.15. Sample and electron beam interaction at an atomic scale and the interaction depth distribution. (Adapted from Paul Whiteside,[110] 2016).

1.2.2.3 Atomic Force Microscopy Characterization

An atomic force microscope (AFM) is mainly composed of a cantilever, a laser beam, a photo-detector and a display system (see Figure 1.16).[111] The cantilever is normally made from silicon with a tip in the nanometer range. The interaction forces between the tip and the sample surface are the key parameters for the AFM measurement. There are several kinds of forces that can be applied for the measurements, such as van der Waals forces, and mechanical contact forces. Generally, there are three main modes of AFM measurement, including intermittent mode, contact mode, and vibrating mode. What is used in this thesis is the intermittent mode (or tapping mode). It is relatively soft and not harmful to the tip nor to the surface of the sample. In tapping mode, the cantilever will tap with a high resonance frequency, and the feedback will be continually used to adjust the distance between the sample and the tip. Therefore, the image of defined surface morphology is obtained. AFM characterization is considered as a useful tool for obtaining the height or thickness of the measured nanostructures, especially 2D nanostructures.
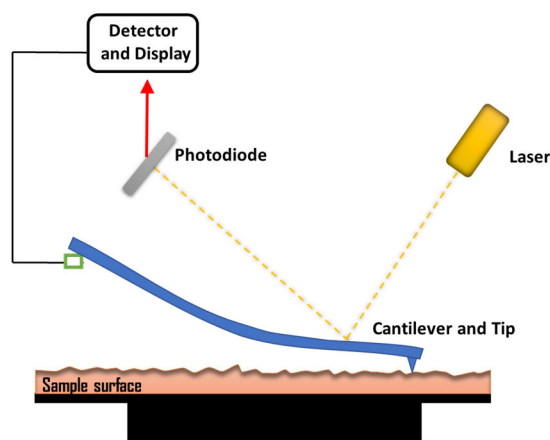
Figure 1.16. Schematic representation of AFM set-up.[111]

1.2.2.4 Powder X-ray Diffraction Analysis

In 1912, the equation which defined the direction of diffracted X-rays from the crystals was interpreted by William Lawrence Bragg and William Henry Bragg.[112] It is written as:

$$2d\sin\theta = n\lambda,$$ (1.10)

where λ is the incident radiation wavelength, θ is the half value of the diffraction angle, and d is the lattice distance of the crystal. This is known as Bragg diffraction. This phenomenon has two key factors, including one wave which can produce interference, and one scattering center which forms a periodic arrangement. Two important geometry relationships are also involved during the diffraction: (1) the incident radiation, normal line of reflecting surface and diffraction radiation are coplanar; (2) the angle of diffraction radiation and transmission radiation must be equal to 2θ, which is defined as the diffraction angle. The schematic graph of Bragg diffraction is shown in Figure 1.17. Nanomaterials measured by XRD can be characterized to get basic information about crystallinity and rough dimensional information.
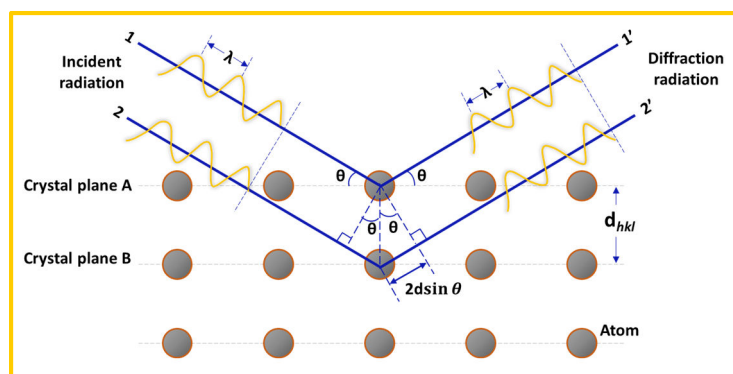
Figure 1.17. Schematic representation of Bragg diffraction process.[112]

1.2.2.5 Spectroscopy Characterizations

Spectroscopy characterizations including nuclear magnetic resonance spectroscopy (NMR), terahertz spectroscopy (THz) and X-ray photoelectron spectroscopy (XPS) play a vital role in clarifying the chemical composition, ligands, size distribution, and other sample information. There are several common instruments used in this thesis, such as Ultraviolet-visible spectroscopy (UV-vis), Fourier transform infrared spectroscopy (FTIR), which we will introduce in detail in the following sections.

1.2.2.5.1 Ultraviolet-visible Spectroscopy

Ultraviolet-visible (UV-vis) spectroscopy is one kind of absorption spectrometry which utilizes the absorbing ability of the measured materials in the spectrum range between 190 and 1100 nm.[113] The produced spectra normally come from the energy level transition of valence electrons, occasionally together with the transition through vibrational levels and rotational levels inside molecules. The transition types include four basic kinds, such as π–π^*, n–π^*, σ–σ^*, and n–σ^*, from which σ–σ^* transitions need the largest energy. In a typical set-up, a white-light source goes to a diffraction grating (monochromator), passes a slit and lens to focus. Then it passes several mirror systems to converge. Finally, the light reaches the detector after passing through the reference and the sample and being absorbed (see Figure 1.18a). UV spectroscopy plays an important role in the determination of the concentration of particles, particle agglomeration condition, and bandgaps.
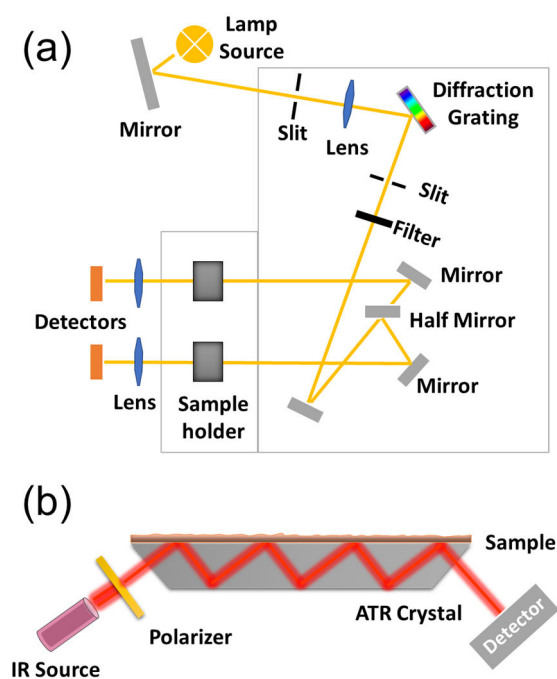
Figure 1.18. Schematic representation of a typical set-up of a UV-Vis spectrometer (a) and the ATR unit (b) from FTIR Spectrometers.[114-115]

1.2.2.5.2 Fourier Transform Infrared Spectroscopy

There are at least two requirements for a significant infrared spectroscopy (IR) measurement: (1) the applied radiation should contain enough energy for the vibrational transition of sample molecules; (2) there should be certain interaction between radiation and sample molecules. Molecules like N_2 or Cl_2 without dipole moments will not present dipole change in the vibration, so those molecules are not IR-active.[116-117] Theoretically, two basic vibration modes exist in molecules, embodying stretching vibration and bending vibration. These vibration properties of sample molecules define the obtained IR spectra, including the frequency, the number, and the intensity of absorption peaks.[116-117] Dispersive IR and Fourier transform IR are two types of IR spectroscopy. Dispersive IR only adopts a small range of wavelengths towards the detector. When it comes to FTIR, the light goes through a Michelson interferometer which can split the light beam and recombine the beams, letting the two split beams interfere. Attenuated total reflection (ATR) is used to avoid the strong attenuation of the IR signal for the sample.[114] It employs an ATR crystal with high refractive index, which impels the light to be fully internally reflected at least once (see Figure 1.18b). The original light contains a full range of wavelengths, which is modulated by the interferometer to obtain a specified spectrum. The Fourier transform algorithm (FT) is applied to analyze the early data of absorption information to the final absorption spectra. Generally, this type of characterization could provide some basic information about the detected materials, such as the molecule structure based on the absorption positions and shapes, and also the component distribution of compounds based on the intensity of characteristic absorption peaks.

1.2.3 Synthesis and Applications of 2D Tin Chalcogenide Nanomaterials

Two-dimensional nanostructures have been widely investigated owing to their remarkable electronic, optoelectronic and catalytical properties.[118-119] Based on different applications, different elements will be selected, which is specifically employed for desired investigations. Nanomaterials with more environmentally friendly elements including tin chalcogenides (SnS, SnSe, SnTe) become promising and attract more attention compared to lead-or cadmium-based

toxic nanomaterials (*e.g.* PbS, CdSe). Therefore, we stress here several encouraging syntheses and applications of 2D tin chalcogenide nanostructures, especially emphasizing electronics, optoelectronics, NIR detectors, topological crystalline insulators, and other promising applications.

In literature, theoretical and experimental studies all emphasize the promising properties of 2D SnS such as selected valleys' optical excitation, ferroelectric and piezoelectric properties.[120-121] Wong *et al.* reported an improved synthesis method for obtaining large-size and thin SnS crystals, which showed high sensitivity, superior selectivity, low detection limit (≪100 ppb), as well as good reversibility to gas NO_2. This reveals that SnS presents good potential for gas sensing.[122] In addition, it was also found that there is high responsivity (2.04×103 A W^{-1}) and high external quantum efficiency, together with a fast response time of 90 ms through the photodetector built with SnS crystals, showing excellent behaviors as promising photodetectors.[122]

Xue's group reported a PVT method for preparing 2D SnS nanoplates. The transport measurements reveal the mobility along the zigzag direction was much higher than that along the armchair direction (1.7 times larger).[123] The measured hole mobility can reach 20 $cm^2\,V^{-1}s^{-1}$, and the current on-off ratio reaches 10^4 at 77K. SnSe nanomaterials also show similar anisotropy properties to SnS nanomaterials as they have similar crystal structures.[124]

SnTe has been confirmed as a remarkable topological crystalline insulator (TCI) based on its special crystal symmetry, and a potential material in mid-IR applications, as well as photovoltaic devices.[8-11, 125] Talapin's group evaluated the photovoltaic and thermoelectric applications of synthesized SnTe nanocrystals. It is found that there are low electrical conductivities of approximately 10^{-10} S cm^{-1} on original ligand capped SnTe nanocrystals. However, the conductivity dramatically raises by at least 6 orders of magnitude by hydrazine treatment to remove oleic acid layers. Additionally, Zhang's group prepared SnTe with distinct facets and morphologies, showing suitability for transport studies of topological surface states.[11]

Chapter 2 Motivation

Colloidal 2D semiconductors are nowadays highly investigated and show promising properties and trends for low-cost photodetectors, sensors, solar cells and even spintronic devices. However, the model materials such as CdS (Se,Te) and PbS (Se, Te) contain heavy and toxic metals. To solve this problem, nanomaterials with more environmental friendly elements and equivalent spectral properties including tin chalcogenides (SnS, SnSe, SnTe) are now becoming promising and attract substantial attention over the last years.[3, 126-128] Particularly, tin (II) sulfide, which owns an indirect and a direct bandgap of 1.07 and 1.3 eV respectively, presents a layered orthorhombic (OR) crystal structure, which is a distorted rock-salt structure. It contains atomic double layers with in-plane covalent bonds and weak van der Waals forces out-of-plane. Therefore, the crystal structure already endows the chemical stability of the 2D morphology in SnS nanostructures.[129]

Recently, several investigations have been published for obtaining uniform 2D SnS nanostructures, although the main methods are physical vapor deposition, molecular beam epitaxy, and mechanical exfoliation.[130-131] Nevertheless, they normally lead to polydisperse, irregular shaped SnS nanostructures.[130] Therefore, the colloidal synthesis becomes more attractive, owing to the advantages that uniform nanostructures can be obtained in the presence of different kinds of surfactants to control the crystal growth. This leads to uniform lateral shapes and well-faceted edges. Solution-based nanostructures and devices can be further fabricated by spin coating or casting process. This has been considered as a prerequisite for the significant and cheap fabrication of well-ordered structures or deposition on a large variety of substrates for further usage.

The analysis of previously published work allows one to conclude that most of the synthesized SnS (analogically SnSe) present nanocubes and nanoparticles. Meanwhile, most are prepared with halogenated precursors as tin precursors (*e.g.* tin chloride), or in the presence of hexamethyldisilazane (HMDS) in the synthesis flask for obtaining 2D nanostructures.[83, 132-134] Thus, one goal here is to find one possible recipe which can yield well-shaped 2D SnS nanosheets without halogenated compounds involved or flammable precursors with less stability and high reactivity such as bis[bis(trimethylsilyl)amino] tin(II). This will be investigated in detail and discussed in Section 3.1 of the results and discussion chapter.

During the investigations on the synthesis method, another aspect was put into focus – the special property of SnS to show in-plane anisotropy. This feature is present in various 2D nanocrystals, such as rhenium disulfide and phosphorene. It can give nanomaterials more possibility to display different responses to external stimuli (*e.g.* polarized light), brightening the field of electronic, optoelectronic and other applications. As a phosphorene analogue, SnS nanocrystals are also considered as one type of promising and potential anisotropic 2D nanomaterial. Hence, another goal stated here is to reveal the regularities of edge-faceting of SnS nanosheets in the system in order to make it applicable for anisotropic electron transport. Thus, to optimize the synthesis approach in order to make tunable edge faceting possible in SnS nanostructures becomes attractive. This will be studied and discussed in Section 3.2 of the results and discussion chapter.

In contrast to SnS (analogically SnSe), tin telluride (SnTe) displays a rock-salt cubic crystal structure instead of the layered OR structure probably due to the closer electronegativities of Sn and Te. It is one representative type of narrow band-gap semiconductors, which owns a bulk bandgap of only 0.18 eV. Recently, it has been discovered as an extraordinary topological crystalline insulator (TCI).[9-10] However, the preparation of solution-based SnTe nanocrystals published so far, only yields zero-dimensional or one-dimensional nanostructures.[125, 135] 2D nanostructured SnTe synthesized with colloidal methods has never been reported to the best of our knowledge. This brings out the third goal of this thesis: to develop a stable recipe to produce 2D colloidal SnTe nanostructures. It will give more inspiration and experience to the discovery of 2D Te-based metal chalcogenide nanocrystals in solution. This will be investigated in Section 3.3 of the results and discussion chapter.

Chapter 3   Results and Discussion

In this chapter, the successful optimization of recipes to obtain 2D SnS nanosheets (NSs) with high crystallinity and tunable edged-faceting, as well as single-crystal SnTe with 2D morphology will be described and discussed in detail. They are all prepared via the hot-injection colloidal method during the synthesis. The influences of each ligand and other related parameters during the reaction will be discussed to figure out the possible formation mechanisms of the synthesized nanocrystals. The nanocrystals of SnS and SnTe have been characterized using electron microscopy techniques including TEM, SEM, HRTEM, as well as various spectrometers such as UV-Vis-NIR and FTIR spectroscopy. The crystal structures of SnS and SnTe nanocrystals have been confirmed by XRD and SAED. The thicknesses are determined by AFM, together with the Scherrer equation based on XRD data. The electrical measurement on the obtained nanocrystals will also be shown to display the electronic and optoelectronic response abilities.

3.1 Synthesis and Characterization of Colloidal Square-like Isotropic SnS Nanosheets

■ *The results discussed in the following chapter have already been published as: F. Li, M. M. Ramin Moayed, F. Gerdes, S. Kull, E. Klein, R. Lesyuk and C. Klinke, "Colloidal tin sulfide nanosheets: formation mechanism, ligand-mediated shape tuning and photo-detection". J. Mater. Chem. C, 2018, 6(35), 9410-9419.[129]*

3.1.1 Synthesis and Basic Characterizations

The crystal structures of SnS nanomaterials belong to the layered crystal structure system. Thus, the 2D morphology is preferred by SnS instead of 0D nanoparticles or 1D nanowires. Most of the colloidal syntheses of SnS so far have been conducted with halogenated precursors. Halogenated precursors have been reported to be fully complexed by hexamethyldisilazane (HMDS) to form 2D SnS nanosheets in the end. Therefore, introducing halogenated precursors to the reaction is

not necessary.[136] In addition, the flammable precursor like bis[bis(trimethylsilyl)amino] tin(II) has also been adopted to yield SnS NSs with the lateral size and thickness of 7 μm × 20 nm.[134, 136-137]

Here, a novel halogen- and HMDS-free synthesis of SnS NSs is introduced and demonstrated in detail. Tin acetate (TA), oleic acid (OA), and trioctylphosphine (TOP) in diphenyl ether (DPE) solvent were mixed and degassed at 75 ℃ (2 hours), followed by heating up to the reaction temperature 230 ℃ under N_2 atmosphere. The reaction started immediately after the rapid hot-injection of sulfur precursor thioacetamide (TAA). To guarantee the repeatability of the recipe, the injection volume was kept constant for all comparable experiments. Theoretically, TA in the reaction was partially transformed to tin oleate by the replacement of OA. Both oleate and acetate groups would participate in the nucleation and growth process of SnS NSs.[138] As a comparison, tin (II) chloride, acting as a tin precursor, was also studied. It turns out that the product only contains irregular-shaped SnS NSs and byproducts (see Figure 3.1). The product does not show well-defined morphology or thin thickness from the TEM contrast, which indicates that halide ions without the assistance of *e.g.* HMDS will result in non-2D nanostructures in our case.
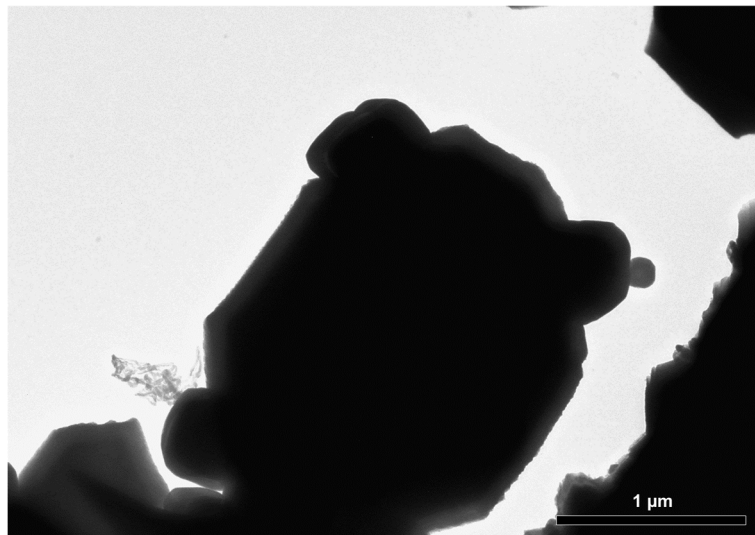
Figure 3.1. TEM image of SnS synthesized using 0.25 mmol $SnCl_2 \cdot H_2O$. [F. Li, M. M. Ramin Moayed, F. Gerdes, S. Kull, E. Klein, R. Lesyuk and C. Klinke, *J. Mater. Chem. C*, **2018**, 6(35), 9410-9419], Published by The Royal Society of Chemistry.

The synthesized square-shaped SnS NSs present an average lateral size of about 460 nm with our standard recipe mentioned above (see Figure 3.2a). The well-ordered SAED pattern in Figure 3.2b demonstrates the high crystallinity of the synthesized single SnS NS (see Figure 3.2c). The

calculated distances match the *d*-spacing values from the list of reflections of OR-SnS bulk (the International Centre for Diffraction Data (ICDD) card, SnS: 00-039-0354). It shows the diffraction planes of, for example, (200), (101), (002) after calculation and analysis of *d*-spacing (see Figure 3.2b).
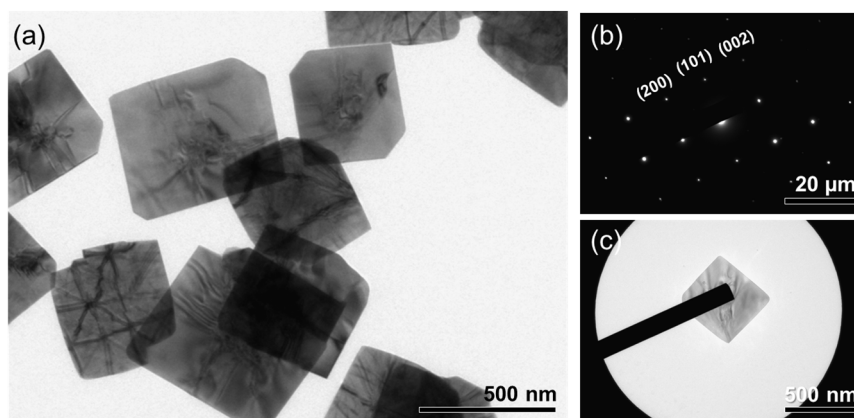
Figure 3.2. (a) TEM image of dispersed square shaped SnS NSs prepared with the standard synthesis process. (b) SAED pattern of an individual SnS NS and the corresponding nanosheet in the TEM image (c). [F. Li, M. M. Ramin Moayed, F. Gerdes, S. Kull, E. Klein, R. Lesyuk and C. Klinke, *J. Mater. Chem. C*, **2018**, 6(35), 9410-9419], Published by The Royal Society of Chemistry.

The X-ray diffractogram of the powder sample of SnS NSs in a capillary also matches the reference pattern of bulk OR-SnS (see Figure 3.3, reflexes of the powder sample). In terms of the SnS NS sample prepared by drop-casting on a silicon wafer, only reflexes belonging to [010] direction can be detected in the XRD data, including (040) and (080) reflexes (see Figure 3.3, reflexes of the film sample). This originates from the texture effect, which only displays the reflexes representing the thickness direction (see Figure 3.3). Texture is determined as the orientation distribution for nanomaterial samples containing plenty of crystals.[139] The level of texture can imply the percentage of preferred orientations in the whole sample. Accordingly, strong texture effects often happen when 2D nanomaterials lie on the substrate by XRD analysis as shown above. Therefore, XRD measurements with dry samples in the capillary are necessary to acquire complete XRD patterns, which aims at precisely identifying the crystal phase.
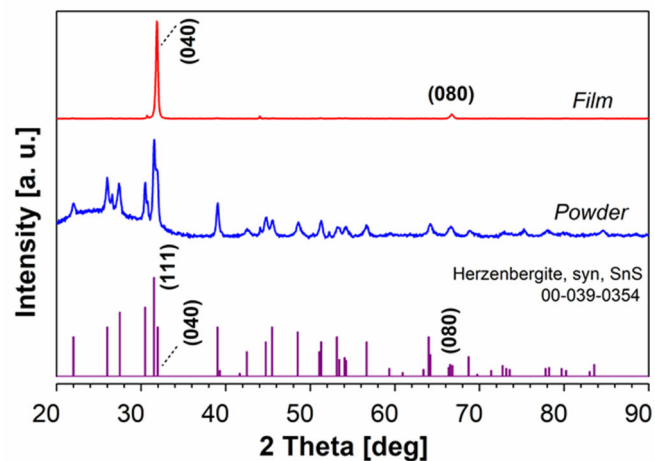
Figure 3.3. XRD diffractograms of drop-casted SnS and powder SnS in a capillary tube. [F. Li, M. M. Ramin Moayed, F. Gerdes, S. Kull, E. Klein, R. Lesyuk and C. Klinke, *J. Mater. Chem. C*, **2018**, 6(35), 9410-9419], Published by The Royal Society of Chemistry.

The Scherrer analysis can be applied to the (040) reflex from the XRD pattern to obtain the thickness value of 29 nm. The SEM images shown in Figure 3.4a demonstrate an overview of the SnS NS morphology, displaying highly yielded square-shaped SnS NSs with smooth surface morphology. Particularly, some of the synthesized square shaped NSs present truncated edges. There are few byproducts such as small nanoparticles produced as well. The characterization of the byproducts will also be investigated later in this section. A typical AFM height measurement demonstrates that the height of the SnS NS is 31 nm (see Figure 3.4b, c).

Theoretically, the colloidal growth of nanocrystals normally involves two factors which are manipulated by the reaction conditions. They are classified as thermodynamic factors and kinetic factors. Thermodynamic factors normally contain the related factors including surface capping, reaction temperature or reduction potential, while kinetic factors contain the same or some other cases, *e.g.* monomer concentration or reaction temperature.[140] It has been widely investigated that the kinetically controllable synthesis is an effective and important pathway to obtain anisotropic growth to an asymmetric nanostructure based on a highly symmetric crystal structure.[140] Based on the determination of thermodynamic control and kinetic control, it is known that a thermodynamically controlled product will be achieved if the whole reaction system is treated with enough time and sufficient activation energy to reach the minimum status of the Gibbs free energy. The Gibbs free energy is composed of the bulk energy and the

total surface energy (see Section 1.1). The total surface energy is the main factor to obtain the minimum status of the total free energy, and it can be manipulated by tuning the capping ligand conditions around the surface of crystals.[141]
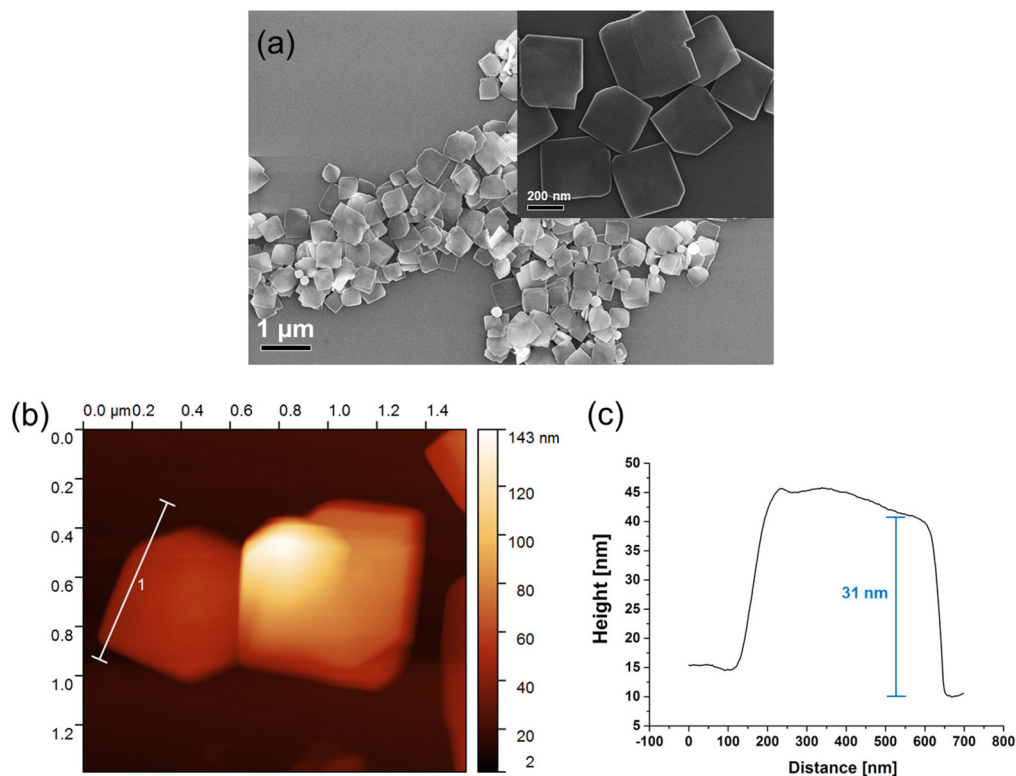
Figure 3.4. (a) SEM image of SnS NSs on the silicon substrate with an inset of SEM image under higher magnification. (b) AFM image and height measurement (c) of an individual nanosheet with a thickness of around 31 nm. [F. Li, M. M. Ramin Moayed, F. Gerdes, S. Kull, E. Klein, R. Lesyuk and C. Klinke, *J. Mater. Chem. C*, **2018**, 6(35), 9410-9419], Published by The Royal Society of Chemistry.

Therefore, capping ligands are considered as one type of vital parameters in the colloidal reaction. They indeed lower the surface energies of all the related facets of nanocrystals and finally result in an adjusted morphology with highest stability. The growth stage involves kinetic factors, such as the surface passivation from the capping ligands which affects the attaching speed of atoms towards the surface and the diffusion condition. Thus, it is necessary to tune the possible reaction parameters especially ligand amounts for the optimization of the SnS NSs, which will be discussed as followed.[142]

3.1.2 Influence of Trioctylphosphine as Ligand

Basically, a crystal facet with lower surface energy presents a slower growth speed, while higher-surface-energy-equipped facets show higher growth speeds, which aims at minimizing the total surface energy according to the Gibbs–Curie–Wulff theorem and the Wulff construction.[143-144] The anisotropic growth of 2D nanocrystals will occur with different ligands selectively binding to different surfaces to provide different speeds for different surface facets to grow further. Therefore, investigating the ligand influence will shed light on the anisotropic growth of 2D SnS nanocrystals and also provide explanation for the growth pathway of the prepared nanocrystals.

Theoretically, the formation of SnS NSs goes through several steps including: (1) the tin precursor complexation by OA replacement before the second precursor TAA is introduced into the reaction; (2) the reaction of two precursors to form nuclei; (3) the growth process to form SnS NSs. The SnS nanostructures synthesized with neither TOP nor OA present shapes of 0D nanoparticle and small square nanoplatelets with sizes smaller than 100 nm (see Figure 3.5a). The obtained small nanoplatelets have exposed edges which are parallel to (001) and (100) facets, as well as to the (101) facets as truncated facets (see Figure 3.5a). This implies that the acetate group can also be considered as capping ligand during the synthesis.

The promotion for 2D morphology with no TOP and no OA by acetate groups can happen, which is also supported by DFT simulations regarding adsorption energies (see Table 3.1). The high adsorption energies of acetate ligands on all these three facets (101), (100), (010) indicate the final product must contain truncated rectangular nanoplatelets. However, the drawback of this recipe is that acetate groups as sole ligands are too short to stabilize the nanocrystals during the reaction, which leads to the formation of small 2D nanocrystals, small particles, and agglomerates as well (see Figure 3.5a).
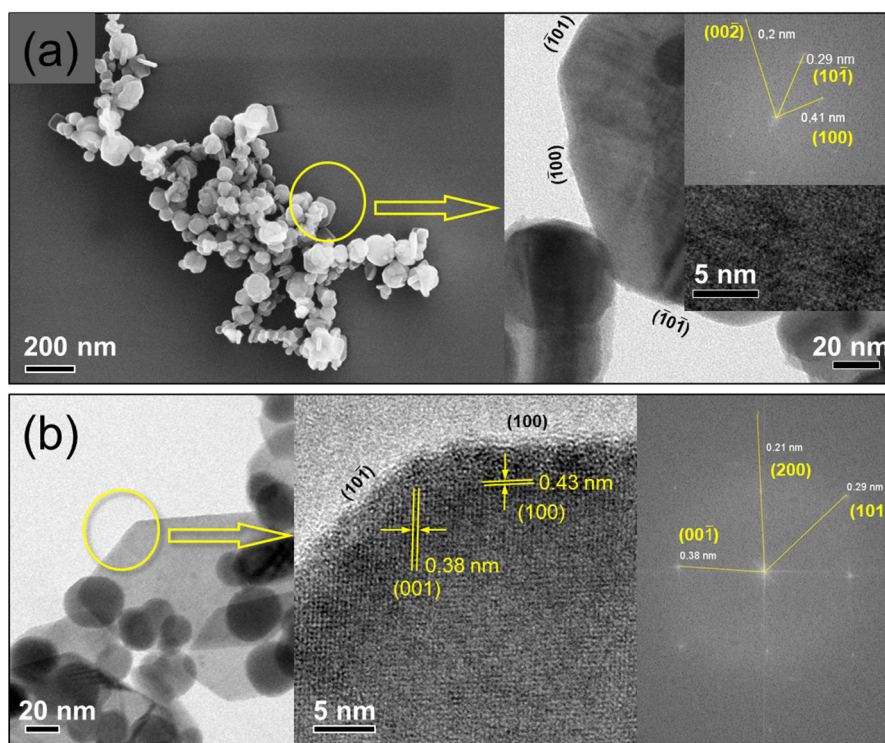
Figure 3.5. (a) SEM image, together with corresponding TEM image and HRTEM image (resulting FFT) of the prepared SnS nanostructures synthesized with no TOP and no OA ligands involved. (b) TEM image and corresponding HRTEM image (resulting FFT) of the synthesized hexagonal nanosheets prepared by applying 0.64 mmol OA without TOP as ligands. [F. Li, M. M. Ramin Moayed, F. Gerdes, S. Kull, E. Klein, R. Lesyuk and C. Klinke, *J. Mater. Chem. C*, **2018**, 6(35), 9410-9419], Published by The Royal Society of Chemistry.

The result above indicates that only acetate ligands are not enough to yield thinner and larger 2D nanostructures. Therefore, different ligands need to be introduced in the reaction system. Then the introduction of OA into the reaction is carried out. Spherical nanoparticles and hexagonal nanosheets were obtained under the parameter conditions that no TOP and 0.64 mmol of OA was used for the reaction with all the other parameters constant (see Figure 3.5b and Figure 3.6a). The reason for this is that oleate ligands prefer the bond on (100) and (101) (or {101} family) facets, which leads to the hexagonal morphology (see Figure 3.5b, HRTEM and FFT). From the HRTEM image, the spacings of two perpendicular lattice fringes are 0.43 nm and 0.38 nm respectively, which correspond to (100) and (001) facets. Thus, the exposed facets of the hexagonal sheets can be determined as (100) facets which correspond to longer sides of the hexagonal sheets (see Figure 3.5b).

45

Table 3.1. Adsorption energies [eV] of different ligands on each facet including (101), (100), (010) facets in a SnS crystal, calculated by the density functional theory (DFT) method. The simulated molecules are respectively the full version of acetate group (AA⁻), simplified versions for TOP molecule, OA and oleate (respectively triethylphosphine (TEP) and tributylphosphine (TBP) for TOP, butyric acid (BA) for OA, and BA⁻ (butyrate) for the oleate). All the simplified molecules were applied here to enable reasonable calculation times and to prevent the influence of the side chains on the simulations. In addition, simulations on different chain lengths (C2 and C4) display similar tendencies regarding different facets. [F. Li, M. M. Ramin Moayed, F. Gerdes, S. Kull, E. Klein, R. Lesyuk and C. Klinke, *J. Mater. Chem. C*, **2018**, 6(35), 9410-9419], Published by The Royal Society of Chemistry.

	SnS-101 side facet (isotropic)	SnS-100 side facet (anisotropic-zigzag)	SnS-010 top facet (Top or down)
TEP (C2)	1.834	1.842	0.651
TBP (C4)	2.061	2.060	0.772
AA⁻ (C2)	3.661	4.453	2.506
AA (C2)	0.988	1.358	0.551
BA⁻ (C4)	3.635	4.355	2.547
BA (C4)	1.076	1.120	0.623

The increase of the TOP amount transforms the product from square-shaped nanoplatelets coupled with many nanoparticles as by-products, to mainly square nanosheets with increasing lateral sizes from 160 nm to 240 nm, to finally 460 nm (Figure 3.6). This tendency can be explained by the preference of TOP ligands on {101} facets instead of other facets. It is shown that a small amount of TOP still can perform its influence to keep the 2D morphology produced (see Figure 3.6b-d). When the TOP amount is larger than 1.0 mmol, there is no significant change on the lateral size of SnS NSs (see Figure 3.6e). Thus, TOP ligands play a vital role in maintaining the anisotropic growth direction of square-shaped SnS NSs together with acetate groups, whilst OA

promotes the hexagonal-shaped nanostructure formation.
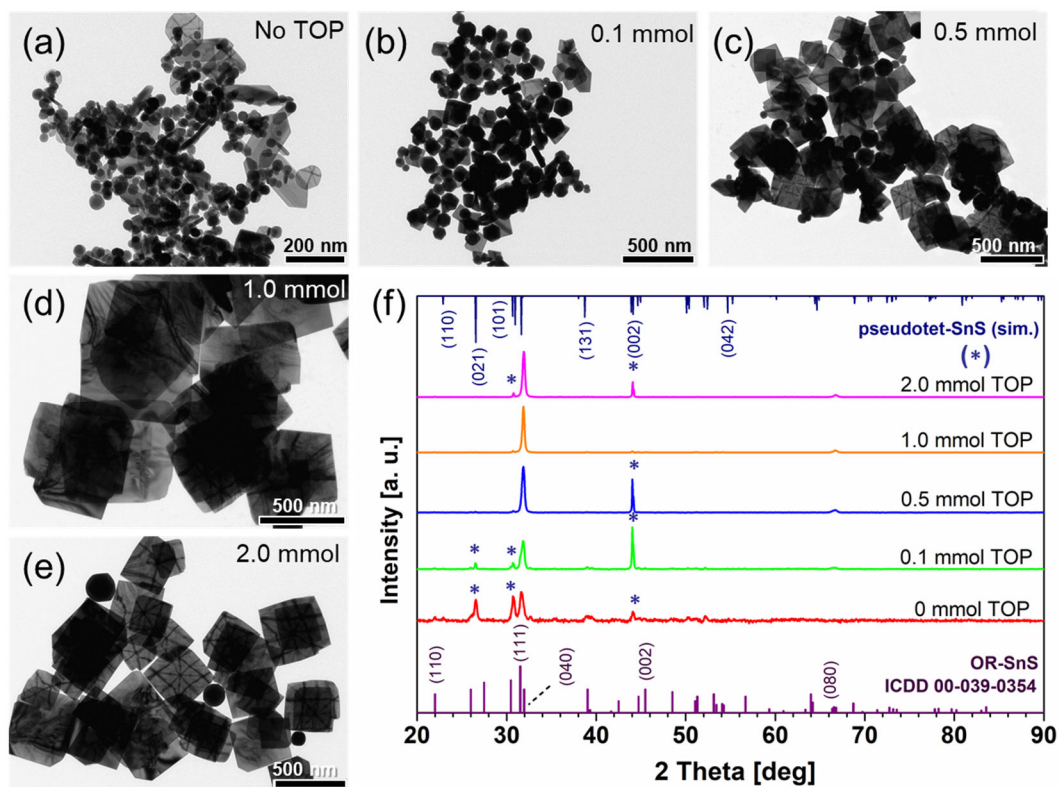
Figure 3.6. (a-e) TEM images of synthesized SnS nanostructures with an increasing amount of TOP used in the synthesis: from 0 mmol to 2.0 mmol. (f) XRD diffractograms of synthesized SnS from a-e. [F. Li, M. M. Ramin Moayed, F. Gerdes, S. Kull, E. Klein, R. Lesyuk and C. Klinke, *J. Mater. Chem. C*, **2018**, 6(35), 9410-9419], Published by The Royal Society of Chemistry.

In Figure 3.6f, the XRD patterns of TOP-variation series display a more pronounced reflex (040) with a rising amount of TOP. This indicates that nanostructures with more square-shaped and larger 2D morphology are formed, together with fewer byproducts like particles and nanoplatelets. When the TOP amount is increased (from 0 mmol to 2.0 mmol), the reflex at 44.04° begins to disappear. This is found to be quite close to the reflex (220) of the zinc-blend (ZB) phase of SnS which locates at 43.8°, instead of OR phase of SnS. Theoretically, the ZB phase of SnS is a metastable phase of SnS. It is reported as one phase only kinetically stable and retained by the specific energy barrier preventing its transformation to the OR phase.[145-146] However, the pseudotetragonal (PT) phase which is more stable under our reaction conditions, can better explain the diffraction reflex at 44.04° with the convolutions of 43.9° and 44.1° from PT phase.[132]
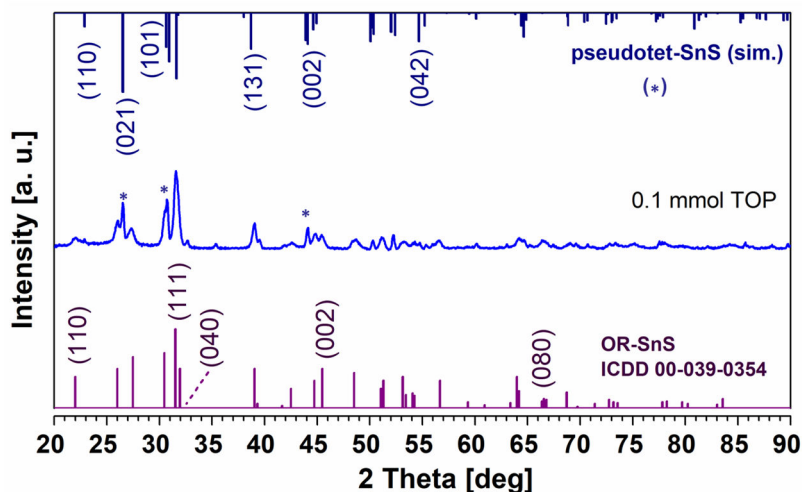
Figure 3.7. X-ray diffractogram of the prepared SnS nanostructures synthesized by applying 0.1 mmol of TOP during the reaction. The XRD sample was prepared in a capillary tube. [F. Li, M. M. Ramin Moayed, F. Gerdes, S. Kull, E. Klein, R. Lesyuk and C. Klinke, *J. Mater. Chem. C*, **2018**, 6(35), 9410-9419], Published by The Royal Society of Chemistry.

The XRD measurement of the powder SnS NSs sample in capillary synthesized by applying 0.1 mmol of TOP shows the diffraction pattern of the combination of both OR and PT crystal structures, coupled with a small intensity of the reflexes from the crystalline sulfur ($2\theta = 32.7°$ and $35.5°$ respectively corresponding to ($12\bar{1}$) and ($03\bar{1}$), ICDD card 01-072-2402) (see Figure 3.7). Additionally, the reflexes at $30.7°$ and $26.5°$ refer to the facets of (101) and (021) of the PT phase. The SAED patterns also support the crystal structure of the main product OR phase and the byproduct PT phase (see Figure 3.8a and b).

Therefore, with more TOP involved, there will be a higher yield of crystalline SnS NSs with the OR phase, together with a gradual disappearance of PT SnS nanocrystals. The thickness values obtained from XRD data of the samples from TOP-varying experiments are in a range between 24 and 29 nm (AFM data are shown in Figure 3.9).
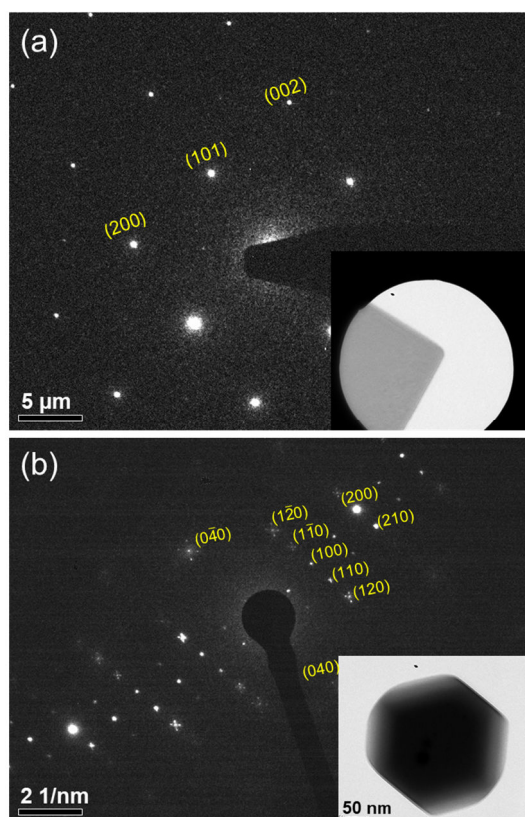
Figure 3.8. (a) The SAED pattern of an individual SnS nanosheet as the main product and an individual SnS nanoparticle as a byproduct (b). [F. Li, M. M. Ramin Moayed, F. Gerdes, S. Kull, E. Klein, R. Lesyuk and C. Klinke, *J. Mater. Chem. C*, **2018**, 6(35), 9410-9419], Published by The Royal Society of Chemistry.
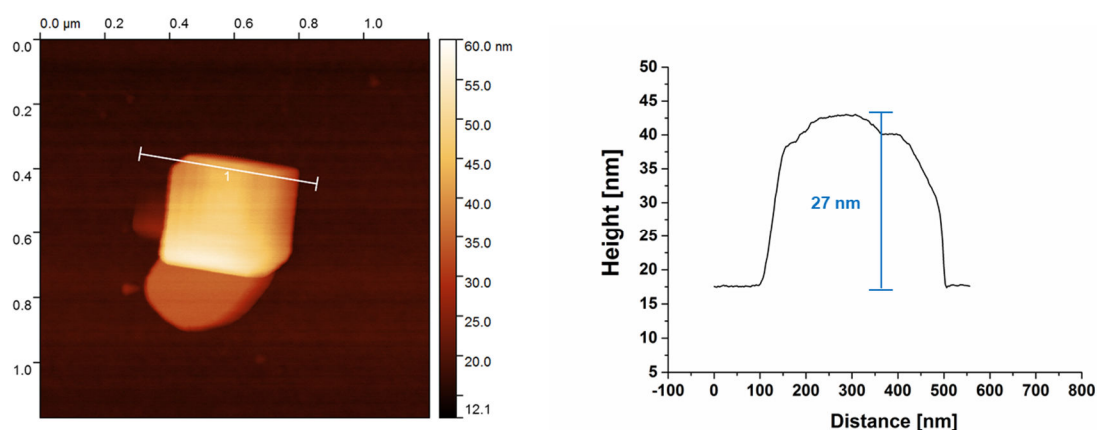
Figure 3.9. AFM image and the height measurement of an individual SnS NS, which shows that the measured thickness is about 27 nm. This value is slightly larger than that calculated based on XRD data (26 nm). The sample was synthesized using a higher TOP amount, 2.0 mmol with other reaction parameters constant. [F. Li, M. M. Ramin Moayed, F. Gerdes, S. Kull, E. Klein, R. Lesyuk and C. Klinke, *J. Mater. Chem. C*, **2018**, 6(35), 9410-9419], Published by The Royal Society of Chemistry.

In terms of HRTEM characterization, an individual truncated square-shaped nanosheet was measured (see Figure 3.10, Figure 3.11). Based on the SAED pattern and the corresponding TEM image, all the edges are confirmed to be parallel to the corresponding facets as shown in Figure 3.10a and d. They demonstrate the four main side edges parallel to the {101} facets, coupled with truncated edges referring to (100) and ($\bar{1}$00) facets for the nanosheet (SAED pattern needs to be rotated by instrumentation according to certain staggered angle). The detailed HRTEM images (Figure 3.10b, c) for the selected area of the individual SnS NS reveal that the measured lattice spacings of the crystal fringes along the exposed edge also match the SAED results, demonstrating the exposed ($\bar{1}$00) and ($\bar{1}$01) facets. This is also proven by the corresponding FFTs (see insets of Figure 3.10b, c).
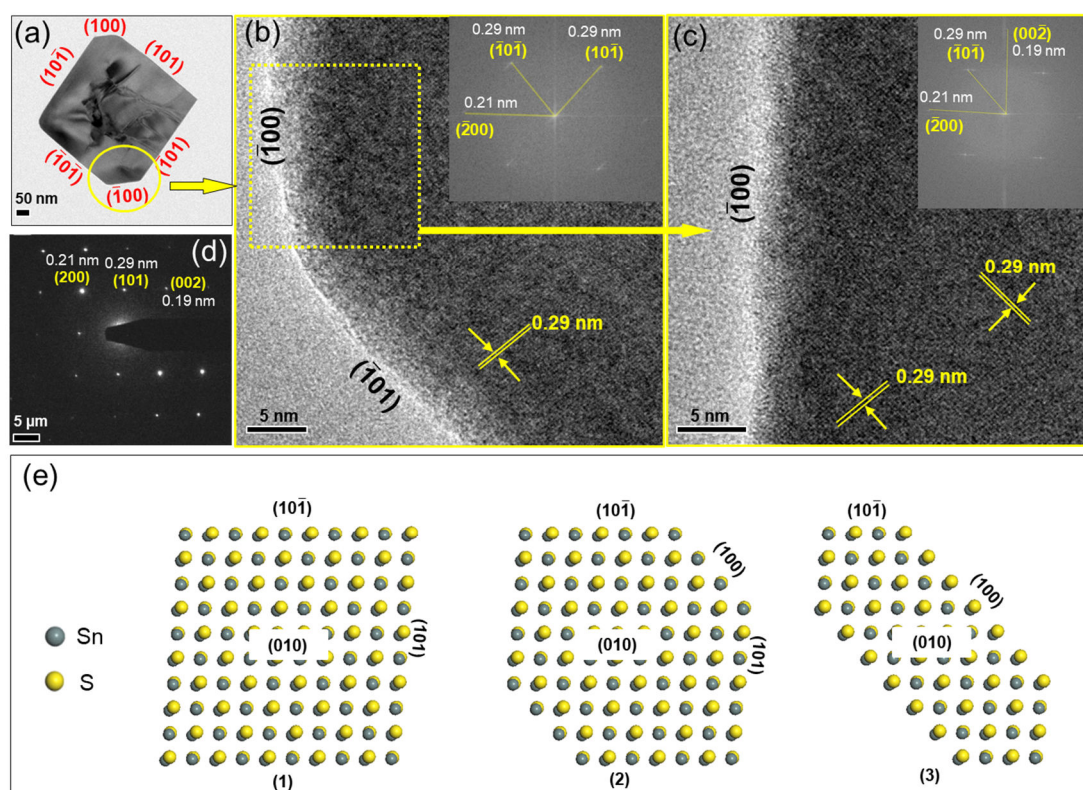
Figure 3.10. (a) TEM image and HRTEM images, as well as FFT analyses (b, c) of an individual SnS nanosheet prepared by using the standard synthesis parameters. Each facet has been recognized according to the corresponding SAED pattern (d) and the HRTEM measurements (b, c). (e) A set of atomic models of SnS with more and more truncated edges which parallels to the (100) facet is shown here. Owing to the layered crystal structure, there is an overlapping phenomenon for the drawn Sn or S atoms. [F. Li, M. M. Ramin Moayed, F. Gerdes, S. Kull, E. Klein, R. Lesyuk and C. Klinke, *J. Mater. Chem. C*, **2018**, 6(35), 9410-9419], Published by The Royal Society of Chemistry.

50

Atomic models for square-shaped SnS with more and more truncated edges are drawn to observe the atomic arrangements along the [100] direction (see Figure 3.10e). Meanwhile, the atomic arrangements of (101), ($\bar{1}$01) and (100) planes demonstrate that there are alternatively ordered Sn and S atoms in (101) and ($\bar{1}$01) facets, and (100) plane consists of Sn and S atoms lying line by line along the Y axis (see Figure 3.12a, b). There is always one bond out of the three bonds, which is present perpendicular to the facets.

Based on the CBC method,[80] TOP is one kind of L-type ligand and it would prefer to bind to metal centers. Our DFT simulations also reveal that TOP has a higher preference to the {101} facets compared to other facets such as the (010) facet. Thus, it is concluded that acetate ligands result in the formation of 2D SnS nanoplatelets, while TOP can help to maintain the square shape, as well as to enlarge the size of platelets into larger 2D nanosheets.
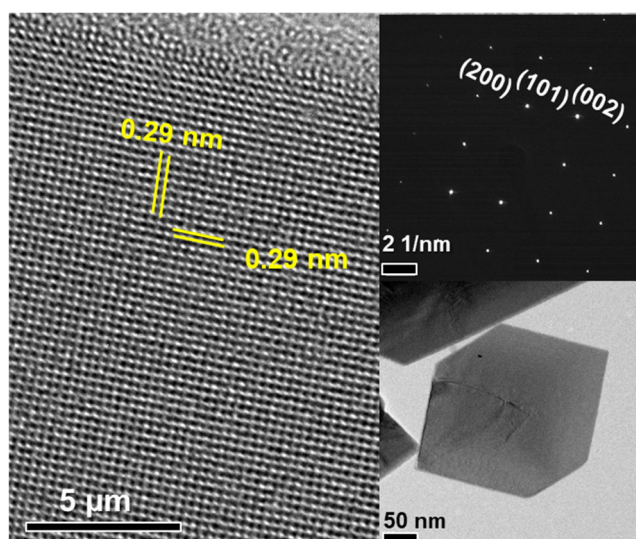
Figure 3.11. HRTEM image of a single crystalline SnS nanosheet showing the lattice spacing of 0.29 nm of clear crystal fringes, as well as the corresponding SAED pattern and the low-magnification TEM image of this nanosheet. [F. Li, M. M. Ramin Moayed, F. Gerdes, S. Kull, E. Klein, R. Lesyuk and C. Klinke, *J. Mater. Chem. C*, **2018**, 6(35), 9410-9419], Published by The Royal Society of Chemistry.
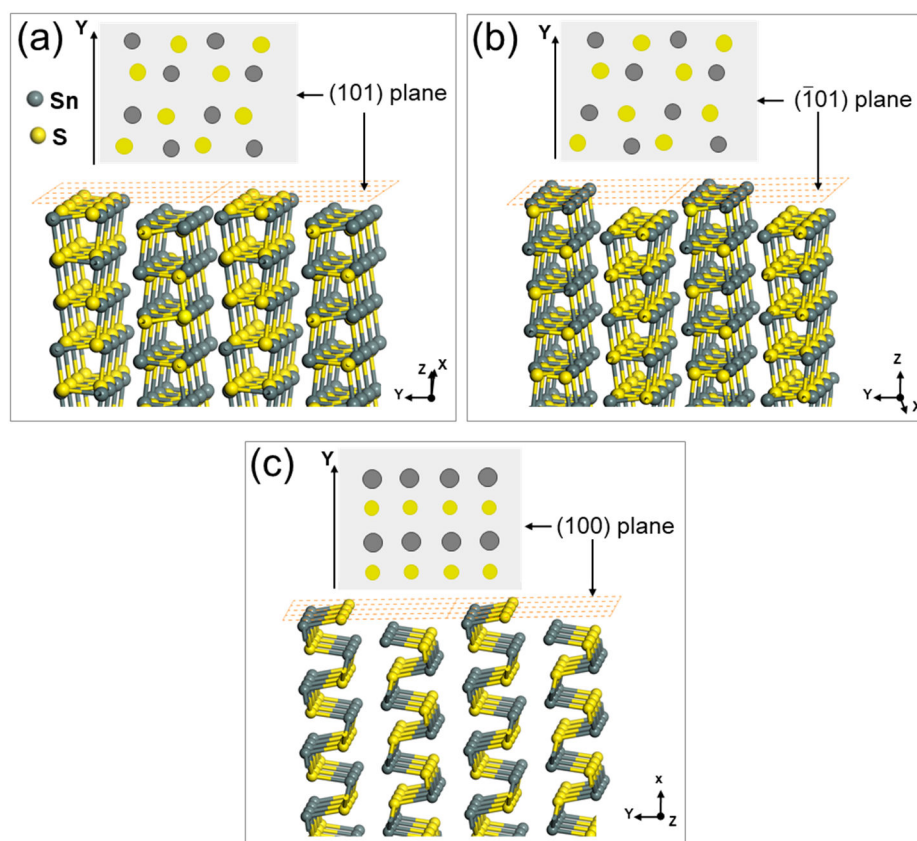
Figure 3.12. Atomic arrangements of the shown (101), ($\bar{1}$01), (100) facets of SnS crystal model. The corresponding top view of each facet is also shown to display the atom order of Sn and S atoms. [F. Li, M. M. Ramin Moayed, F. Gerdes, S. Kull, E. Klein, R. Lesyuk and C. Klinke, *J. Mater. Chem. C*, **2018**, 6(35), 9410-9419], Published by The Royal Society of Chemistry.

3.1.3 Influence of Oleic Acid as Ligand

In this part, we also start to investigate the influence of OA for the formation of SnS NSs with other parameters kept constant (TOP 1.0 mmol). When there is only TOP involved in the reaction without OA, the product is mainly composed of small square-shaped nanosheets and nanoparticles (see Figure 3.13 and Figure 3.14). This result can also be supported by the simulation for TOP as shown above, which reveals that TOP as a ligand in the reaction can enhance the growth towards the square NSs with the exposed (101) facets (see Figure 3.14a). From the TEM images in Figure 3.13 (a-c), there is a clear tendency that lateral sizes of the product increase from 180 to 380 nm, and thicknesses increase from 16 to 29 nm, coupled with a higher degree of uniformity in the morphology.
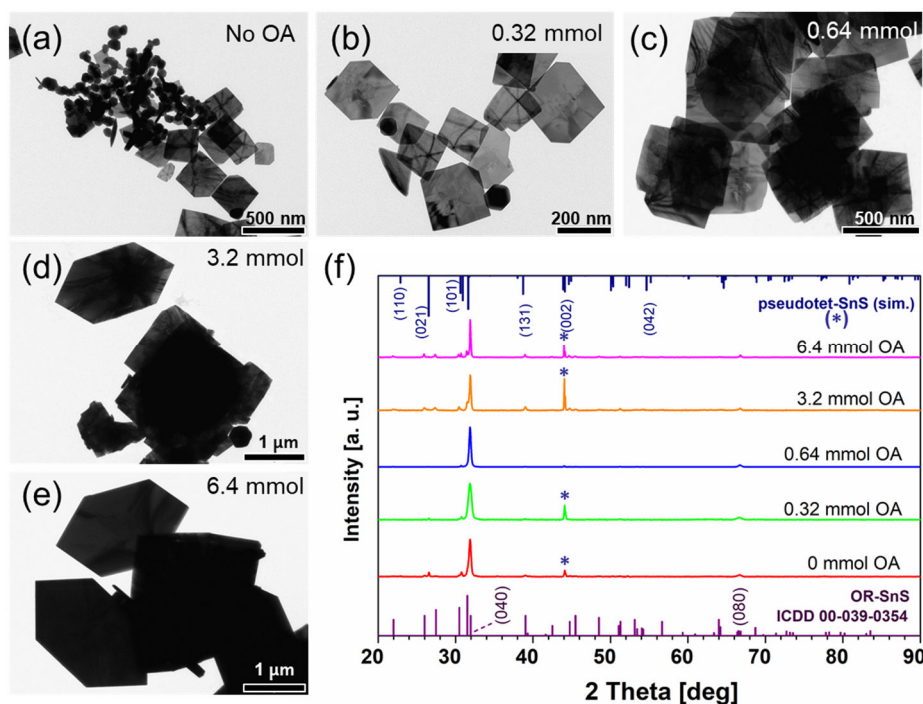
Figure 3.13. (a-e) The shape and size evolution of SnS nanostructures with an increasing amount of OA, from 0 mmol to 6.4 mmol. (f) XRD diffractograms of synthesized SnS from a-e. [F. Li, M. M. Ramin Moayed, F. Gerdes, S. Kull, E. Klein, R. Lesyuk and C. Klinke, *J. Mater. Chem. C*, **2018**, 6(35), 9410-9419], Published by The Royal Society of Chemistry.

In particular, the product is mainly composed of square-shaped NSs as well as particles when a low amount of OA is used (OA≤0.64 mmol). This is because the strong adsorption energy of TOP

on the (101) facet dominates compared to other facets (see Table 3.1). This finally facilitates the formation of square-shaped SnS in the presence of the original acetate. Then, the hexagonal-shaped product appears when the used OA amount is larger than 2 mmol, which is recognized as the starting amount of OA for the formation of hexagonal-shaped nanosheets. Lateral size and thickness values both rise dramatically when OA is larger than 3.2 mmol. According to the law of mass action, the higher the OA amount, the higher the possibility for OA to be bound to the crystal surface, substituting the oleate ligands. Based again on the covalent bond classification (CBC) method,[80] OA, as one type of L-type ligand, is much weaker than oleate which is an X-type ligand. In the case of oleate, it can promote the monomers to grow on the crystal surface, leading to the growth of nanosheets laterally and vertically.
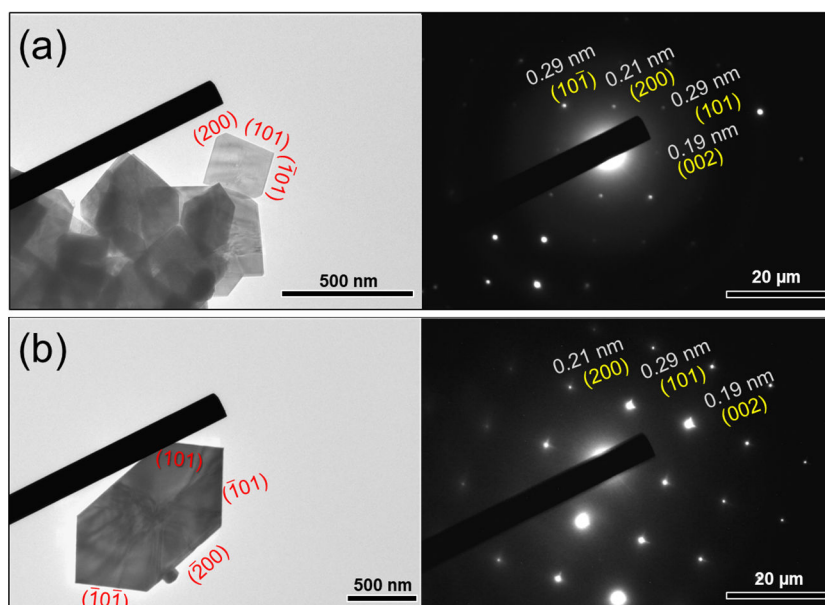
Figure 3.14. (a) TEM image and corresponding SAED pattern of the synthesized SnS NSs using no OA and 1.0 mmol TOP in the reaction. (b) TEM image and corresponding SAED pattern of the synthesized SnS NSs using 6.4 mmol OA and 1.0 mmol TOP. [F. Li, M. M. Ramin Moayed, F. Gerdes, S. Kull, E. Klein, R. Lesyuk and C. Klinke, *J. Mater. Chem. C*, **2018**, 6(35), 9410-9419], Published by The Royal Society of Chemistry.

In Figure 3.13d-e, the higher OA amount (≥3.2 mmol) cause a shape evolution from square to hexagonal, simultaneously affecting the size values (especially 6.4 mmol of OA). The analysis of the lateral sizes measured from TEM overview images (see Figure 3.13), reveals a significant increase from 160 nm to approximately 1600 nm with a rising amount of OA from 0.32 mmol to

6.4 mmol. The above results illustrate that OA plays a vital role in size and shape tuning between square shape to hexagonal shape, which results from the largest adsorption energy of neutral OA molecules on (100) facets compared to those on other facets (see Table 3.1).[129] This eventually leads to the formation of hexagonal-shaped SnS NSs with elongated morphology, under the condition that the OA amount is in excess regarding the acetate groups (see Figure 3.14b).

In addition, XRD diffractograms of OA-varying experiments in Figure 3.13 also show an enhanced pronounced (040) reflex, implying that a suitable quantity of OA can result in stable OR-SnS nanostructures. There is also a schematic illustration of shape and size evolution of SnS nanostructures with changing parameters including OA shown in Figure 3.15. Based on the parameter varying experiments, the nanosheets can be tuned from moderate lateral size (LS=490 nm, TN=29 nm) to larger and thicker nanosheets (LS=875 nm, TN=33 nm) by adopting a higher amount of OA, along with shape change from a square shape to hexagonal and square shapes (see Figure 3.15).
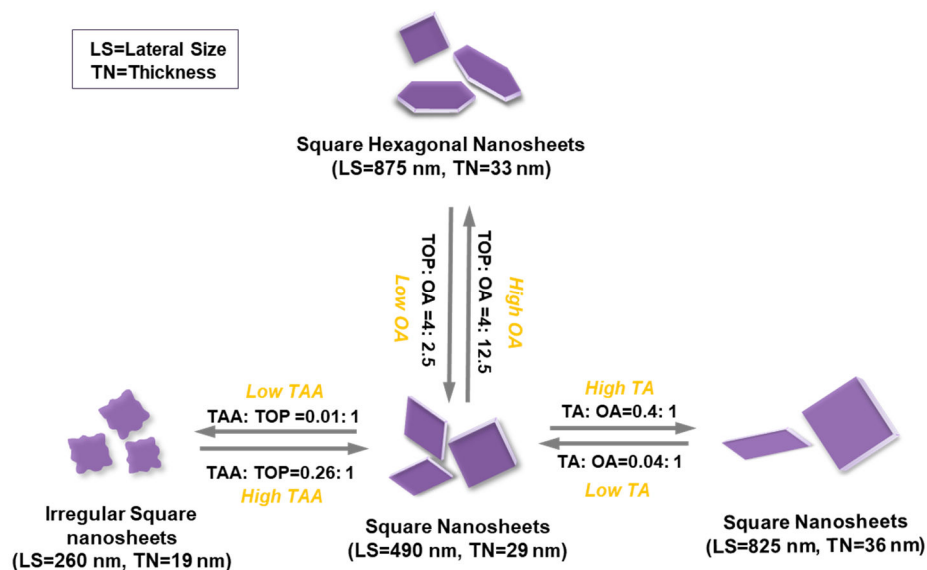
Figure 3.15. Schematic representation of shape and size evolution of SnS nanostructures with the varying parameters including OA, TA, and TAA.

3.1.4 Effect of Precursor Amount

Theoretically, the precursor concentration can define the monomer availability for the nucleation and growth stage, and also specify the number of nuclei for the further step of growth.[142] We observed that the size value dropped with the increase of the amount of tin precursor (see Figure 3.16). When a small amount of TA is used (0.025 mmol), the lateral size reaches nearly 830 nm, and the thickness reaches 36 nm. Generally, the morphology becomes mainly larger and thicker when low TA amount is employed (<0.25 mmol). The reason for that is the lesser amount of TA, the lower the number of nuclei produced, leading to the formation of larger and thicker nanosheets in the reaction. When the TA amount is 0.5 mmol, the nanoparticle product is formed owing to the excess of acetate compared to oleate (see Figure 3.16e).
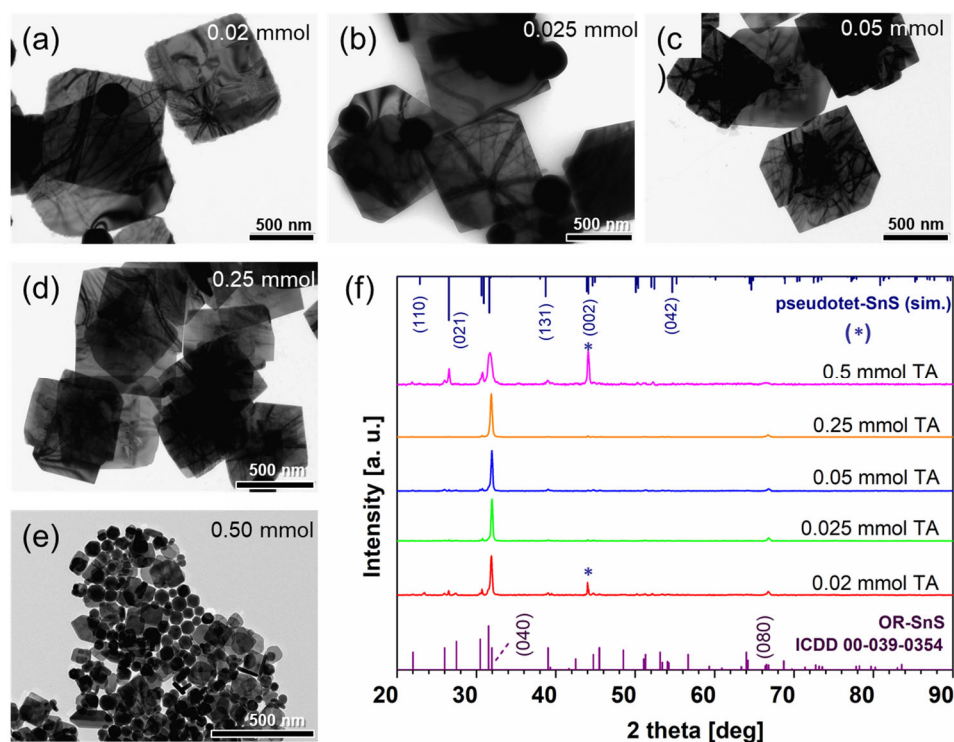
Figure 3.16. (a-e) The shape and size evolution of SnS nanostructures using a varying amount of TA, from 0.02 mmol to 0.5 mmol in the reaction. (f) XRD diffractograms of synthesized SnS from a-e. [F. Li, M. M. Ramin Moayed, F. Gerdes, S. Kull, E. Klein, R. Lesyuk and C. Klinke, *J. Mater. Chem. C*, **2018**, 6(35), 9410-9419], Published by The Royal Society of Chemistry.

In addition, different amounts of sulfur precursors have been also applied in the reaction to clarify the effect of sulfur precursor for the synthesis (see Figure 3.17). The TEM characterizations

show that lower amounts of TAA (≤0.13 mmol) only result in irregular shaped SnS nanostructures (see Figure 3.17a-c). However, the irregular sheets are still crystalline in the OR phase (see Figure 3.18). This may be ascribed to the insufficiency of sulfur monomers for the further growth of SnS nanostructures. The XRD diffractograms also demonstrate that (040) and (080) reflexes become more pronounced while other reflexes decrease with increasing amount of TAA, showing an increasing numbers of 2D nanocrystals (see Figure 3.17f). Additionally, SnS NSs with squared shape start to appear when the TAA amount reaches 0.26 mmol, and the morphology stays similar when 0.52 mmol of TAA is used in the reaction.
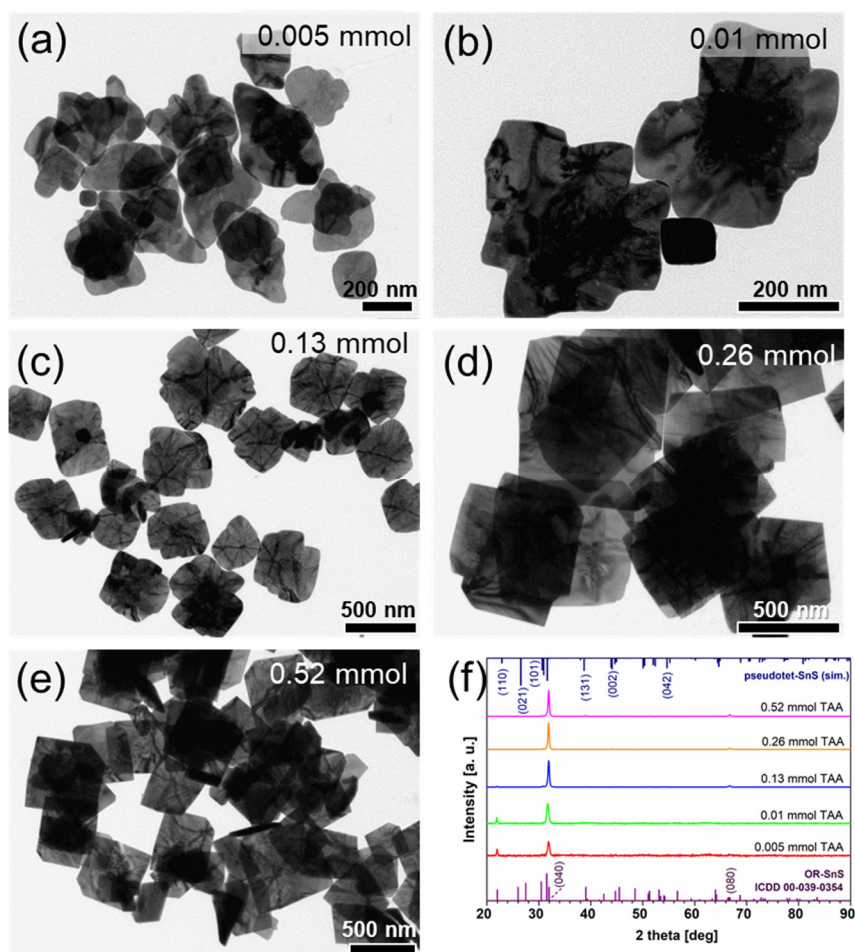
Figure 3.17. (a-e) The shape and size evolution of SnS nanostructures using a varying amount of TAA, from 0.005 mmol to 0.52 mmol in the reaction. (f) XRD diffractograms of synthesized SnS from a-e. [F. Li, M. M. Ramin Moayed, F. Gerdes, S. Kull, E. Klein, R. Lesyuk and C. Klinke, *J. Mater. Chem. C*, **2018**, 6(35), 9410-9419], Published by The Royal Society of Chemistry.

Above all, a growth mechanism for 2D SnS NSs is raised here based on the syntheses mentioned in Section 3.1. In the beginning, tin ions from tin precursors are originally coordinated by acetate as Sn-acetate, forming a shape of strongly distorted trigonal bipyramid as the first coordination sphere.[129, 147] Then TAA as the sulfur precursor suddenly decomposes upon hot-injection, generating S^{2-} ions for next-step interaction with Sn^{2+} ions.
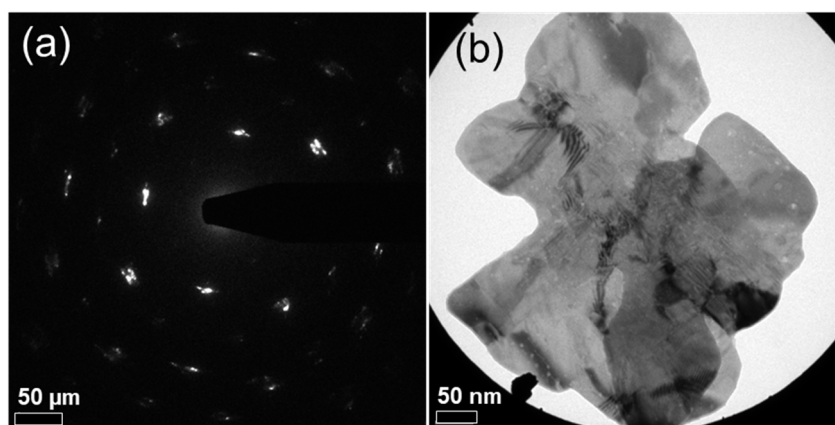
Figure 3.18. TEM image and SAED pattern of irregular-shaped SnS nanostructures synthesized by using 0.01 mmol TAA. [F. Li, M. M. Ramin Moayed, F. Gerdes, S. Kull, E. Klein, R. Lesyuk and C. Klinke, *J. Mater. Chem. C*, **2018**, 6(35), 9410-9419], Published by The Royal Society of Chemistry.

Thus, SnS nuclei start to form after the rapid decomposition of TAA with the burst emergence of monomers, followed by the attachment of surrounding ligands in the solution, which passivate the surface of nuclei. The acetate ligands can trigger the formation of SnS nanoparticles and square-shaped nanoplatelets with the size smaller than 100 nm if there is no OA and no TOP involved in the reaction. This is because of the dominated passivation on {101}, (100) and (010) facets by acetate ligands. If OA is used in the reaction (0.64 mmol), hexagonal sheets and small nanoparticles as byproduct will be produced due to the strong bond of oleate ligands on (100) and {101} facets, whereas square-shaped SnS NSs will be obtained if TOP is introduced to the reaction (1.0 mmol) with no OA involved. When OA amount is smaller than 3.2 mmol, coupled with 1.0 mmol TOP, tin acetate will be partially substituted with tin oleate during the vacuum step. This results in square-shaped NS (approximately 460 nm large) formation without byproducts. Nevertheless, hexagonal NSs will appear if the OA amount is even higher.

Therefore, the final shape or morphology is contributed by the balance between TOP and OA, as

well as the original acetate groups. Tuning the amount of TOP or OA can manipulate the morphology between square and hexagonal NSs. When the suitable ratio of TOP/OA is applied, the product containing pure OR-SnS NSs without PT-type byproducts can be prepared.

3.1.5 Electrical Measurements

In order to study potential electronic applications of the synthesized SnS NSs, the conductivity and photoconductivity of the contacted individual SnS NS (see Figure 3.19) were measured. It shows a relatively higher dark conductivity (7.9 S m^{-1}) of the contacted SnS NS than that of the reported colloidal PbS NSs (one order of magnitude higher than the one of PbS).[148] Upon illuminating on the sheets by a red laser (λ = 627 nm), the conductivity increases with an increase of laser power. This can be explained by an increasing charge carrier concentration owing to the optical excitation and generation of electron-hole pairs.

In addition, the sensitivity of the system can be calculated with the equation (I_{ill}-I_{dark})/I_{dark}, and the value is 0.95. Moreover, the spectral response R_λ and detectivity D^* can also be calculated by applying the following equations:

$$R_{\lambda =} \frac{I_{ph}}{P_{light}\, A}\, , \qquad\qquad (3.1)$$

$$D^*_{=} \frac{R_\lambda\, A^{0.5}}{(2eI_{dark})^{0.5}}\, , \qquad\qquad (3.2)$$

where I_{ph} represents the photogenerated current, P_{light} stands for the density of laser power (50 mW cm^{-1}), A is defined as the effective area of the built device (0.5 μm^2), and e represents the elementary charge. The photodetectors based on the contacted SnS NSs display a spectral response of ~ 3×10^3 AW^{-1}, and a detectivity of ~ 4×10^9 Jones. The performance of SnS NSs is superior compared to the literature with some materials under similar conditions.[122] This is also good evidence for the high quality of SnS crystals and their low defect density.
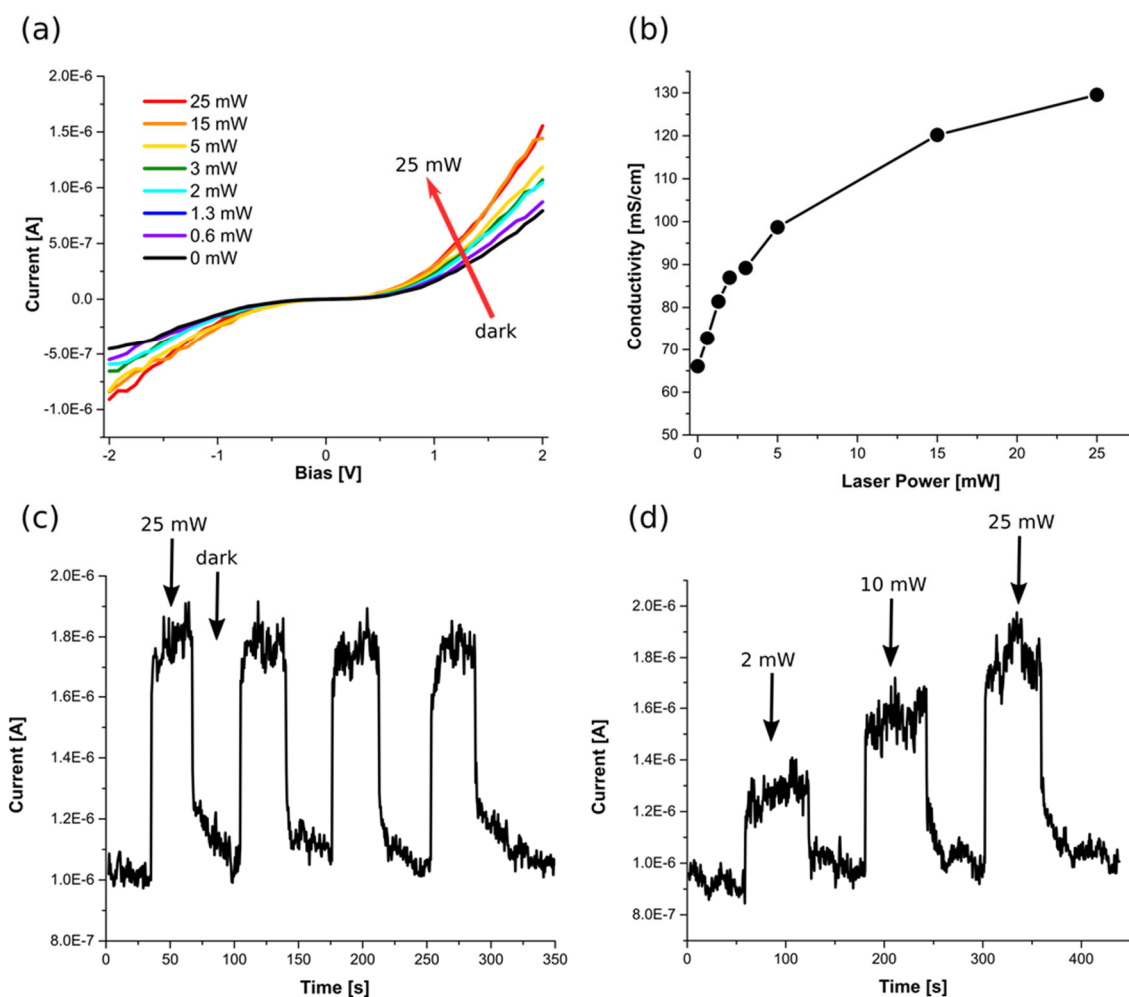
Figure 3.19. The photo-electrical properties of the synthesized SnS NSs. (a) Current-voltage (I-V) characteristics of SnS NSs under illuminations with different intensities of red laser (λ = 627 nm) including 0 mW which is the dark situation, and 0.6, 1.3, 2, 3, 5, 15, 25 mW respectively. (b) Conductivity plot of SnS NSs with increasing laser power. (c) The stability of photo-current under intermittent illumination. The laser power used is 25 mW. The photo-currents are obtained with good stability and also fast transitions between on and off state. (d) Photo-currents under intermittent illumination with increasing laser powers. The stability and speed of the system are maintained although the laser power changes. [F. Li, M. M. Ramin Moayed, F. Gerdes, S. Kull, E. Klein, R. Lesyuk and C. Klinke, *J. Mater. Chem. C*, **2018**, 6(35), 9410-9419], Published by The Royal Society of Chemistry.

We can also observe an increase of the photocurrents with the raising beam power, due to the higher number of electron-hole pairs, but there is also a saturation of dependency of photoconductivity on laser power with higher intensities (see Figure 3.19b). With intermittent illumination, the photo-currents are obtained with good stability and also fast transitions between on and off state (see Figure 3.19c). This property is a vital factor for photodetectors, which is also another indicator of high quality and lack of defects.[149] Furthermore, we observe a

clear change of photocurrents under intermittent illumination with increasing laser powers. The stability and speed of the system are maintained although the laser power changes (see Figure 3.19d). Therefore, these measurements imply the potential of these synthesized SnS NSs for non-toxic cost-effective optoelectronics.

3.2 Synthesis and Characterization of Colloidal Ultra-large and Thin Single-crystalline SnS Nanosheets

- *The results discussed in the following chapter have already been published as: Li, F.; Ramin Moayed, M. M.; Klein, E.; Lesyuk, R.; Klinke, C., "In-plane anisotropic faceting of ultralarge and thin single-crystalline colloidal SnS nanosheets". J. Phys. Chem. Lett. 2019, 10 (5), 993-999.[150]*

3.2.1 Synthesis and Basic Characterizations

In order to improve the morphologies to obtain larger and thinner SnS nanosheets, we varied all the possible parameters in the previous recipe. However, there is no significant progress based on the previous recipe. Thus, we started to replace certain parameters to check the influence.

In this recipe, trioctylphosphine-S (TOP-S) is used to replace the previous sulfur precursor (TAA) to achieve a lower reactivity for the reaction. TOP-S is prepared by dissolving elemental sulfur in TOP solvent and stirring the mixture for 2-3 days to be completely dissolved at room temperature in the glove box.

Therefore, the reaction is similar except for the hot-injection of TOP-S instead of TAA. A typical TEM image of an individual SnS nanosheet with the size of about 3100×2500 nm is shown, along with an SEM image as inset (see Figure 3.20a). The microscopy characterizations show well-defined rectangular nanosheet morphology.[150] The SAED pattern obtained using TEM microscopy displays a well-ordered OR diffraction pattern, which shows a high crystallinity of OR-SnS (see Figure 3.20b). The distances of diffraction dots of the SAED are calculated, demonstrating the representing facets {101}, (100) or (001) respectively. These results then indicate the corresponding facets of the original sheet in the TEM image (see Figure 3.20b, inset) after considering the rotation by instrumentation according to certain staggered angle between the TEM image and the corresponding SAED pattern. Therefore, the rectangular SnS NS presents the exposed facets of (100) and (001). This is different from the small square-shaped SnS nanosheets

synthesized with TAA in the previous section (exposed facets parallel to {101} facets, see Figure 3.10a). Hence, it seems that the syntheses in this section yield a novel phenomenon of edge-faceting difference, which will be investigated and discussed later.
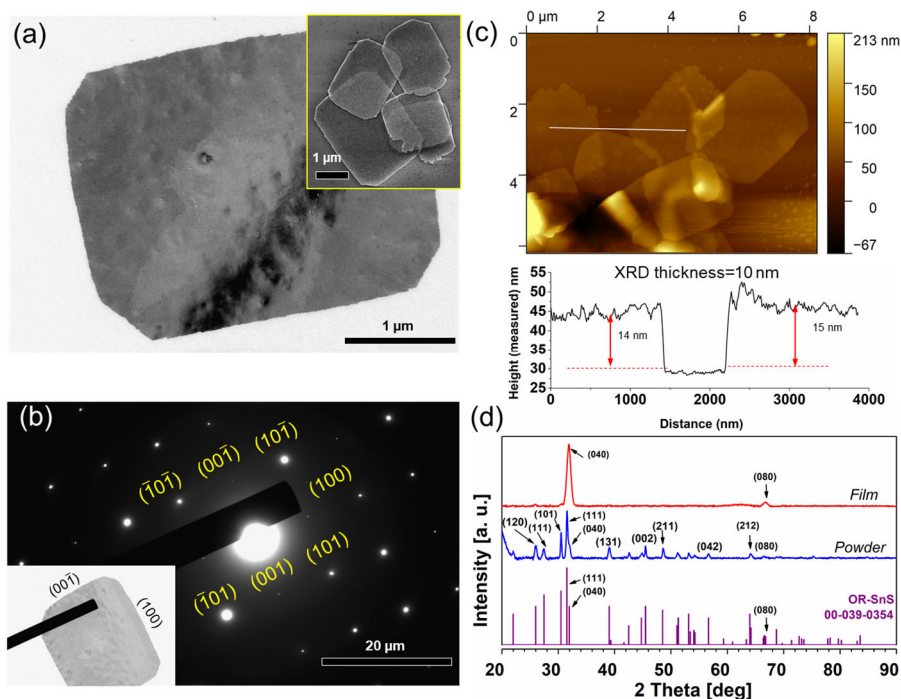
Figure 3.20. TEM image (a), SAED pattern (b), AFM image and corresponding height measurement (c), and XRD diffractograms (d) of the synthesized large and thin SnS NSs. Reprinted with permission from [Fu Li, Mohammad Mehdi Ramin Moayed, Eugen Klein, Rostyslav Lesyuk, Christian Klinke. *J. Phys. Chem. Lett.* **2019**, 10(5), 993-999]. © 2019 American Chemical Society.

The AFM image shown in Figure 3.20c demonstrates that the measured height is approximately 14-15 nm. The calculated thickness value based on the Scherrer equation according to XRD data (see Figure 3.20d) is about 10 nm. The capillary sample is measured by XRD and the result matches well the reflexes form the reference card (00-039-0354). In addition, the texture effect is also shown here in the XRD data of the drop-casted XRD sample, indicating the thickness direction [010]. The mentioned SAED pattern shows the absence of the (010) facet and the XRD data is consistent with the SAED pattern, which both reveal that the nanocrystal surface is oriented along the [010] direction (see Figure 3.20b). Additionally, the thinnest SnS NSs are achieved successfully by applying 0.52 mmol of 2M TOP-S as sulfur precursors during the synthesis. The thickness is down to 7 nm (11 nm for AFM data, see Figure 3.21) and lateral size is about 2.4 μm.
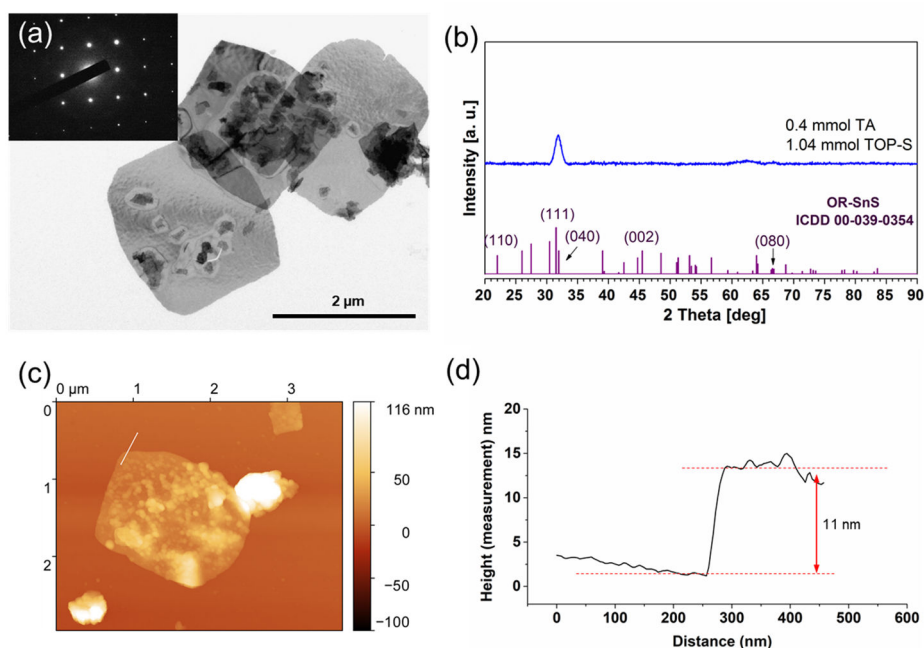
Figure 3.21. The TEM (a), XRD (b) and AFM (c, d) characterizations for the thinnest SnS NSs. Reprinted with permission from [Fu Li, Mohammad Mehdi Ramin Moayed, Eugen Klein, Rostyslav Lesyuk, Christian Klinke. *J. Phys. Chem. Lett.* **2019**, 10(5), 993-999]. © 2019 American Chemical Society.
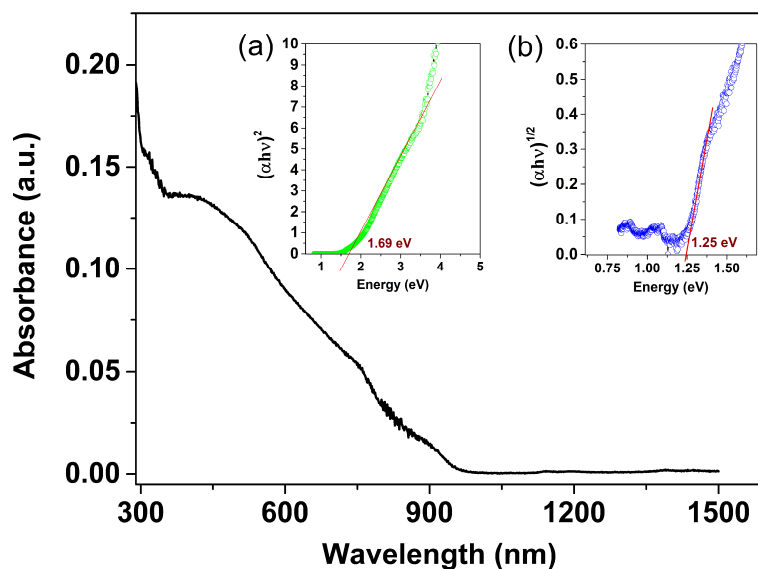
Figure 3.22. Optical absorption spectra of synthesized a-SnS nanocrystals (the inset (a) represents the Tauc plot of $(\alpha h \upsilon)^2$ versus photon energy hυ for obtaining the direct bandgap, while the inset (b) represents the Tauc plot of $(\alpha h \upsilon)^{1/2}$ versus photon energy hυ to obtain the indirect bandgap of SnS nanocrystals). Reprinted with permission from [Fu Li, Mohammad Mehdi Ramin Moayed, Eugen Klein, Rostyslav Lesyuk, Christian Klinke. *J. Phys. Chem. Lett.* **2019**, 10(5), 993-999]. © 2019 American Chemical Society.

The optical bandgap (E_g) of SnS NSs is determined using the Tauc linearization on optical absorption measurements.[151] The intersection points are determined by the tangents to get the direct and indirect bandgaps of respectively 1.69 eV and 1.25 eV (see Figure 3.22, insets).

In-plane anisotropy from the crystal structure level will result in in-plane anisotropy of other properties such as electronic anisotropy, which has been in focus in the recent years. [123, 152-153] Thus, the possibility of tuning the edge-faceting in the solution becomes quite attractive and promising for 2D colloidal anisotropic nanomaterials in electronic or other applications. Here, we have successfully managed to synthesize anisotropic types of SnS nanosheets as well as isotropic types by adjusting the reaction conditions (see Figure 3.23).
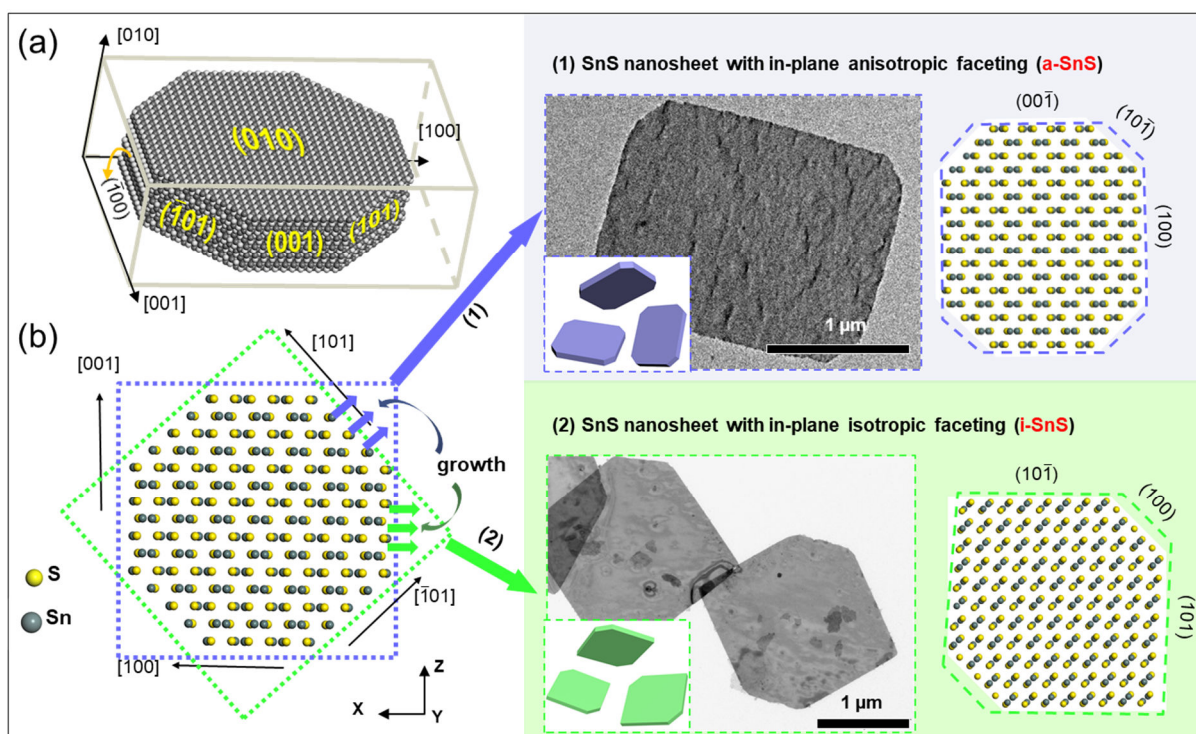
Figure 3.23. (a) A three-dimensional model is built to display an octagonal prism of SnS nanocrystals with all the possible exposed facets marked. (b) Two types of SnS nanosheets symbolically originate from one sketched crystal model marked with two frames which indicate the growth directions respectively. Reprinted with permission from [Fu Li, Mohammad Mehdi Ramin Moayed, Eugen Klein, Rostyslav Lesyuk, Christian Klinke. *J. Phys. Chem. Lett.* **2019**, 10(5), 993-999]. © 2019 American Chemical Society.

The anisotropic type is composed of rectangular SnS NSs with four exposed edges parallel to the (100), (001) planes, or parallel to the corresponding zigzag and armchair direction [001] and [100].

The isotropic type contains rectangular (or nearly square) SnS NSs with exposed edges parallel to the {101} planes, which correspond to four isotropic "ladder" directions (see Figure 3.23, Figure 3.24, Figure 3.25). We determine these two types as respectively anisotropic-SnS (a-SnS) and isotropic-SnS (i-SnS) NSs in this thesis. SnS presents an orthorhombic crystal structure with Sn and S atoms arranging in two adjacent layers, which stack along the Y (or b) axis via weak van der Waals interactions.[123] A 3D crystal model of an octagonal prism presenting space-filling SnS crystals, is drawn here as a hypothetical growth origin to find the growth pathway for these two different types of SnS NSs (see Figure 3.23a, b-(1), b-(2)). The a-SnS NSs are prepared via applying 0.64 mmol of OA and 1.0 mmol of TOP in the reaction system, and rapid injection with 0.26 ml of 1 M TOP-S at 300 °C. They are in rectangular shapes with edges parallel to the armchair/zigzag directions. In Figure 3.24, we can observe that the main difference of the anisotropic side 1 (100) facet and the anisotropic side 2 (001) facet, as well as the isotropic side belonging to the {101} planes.
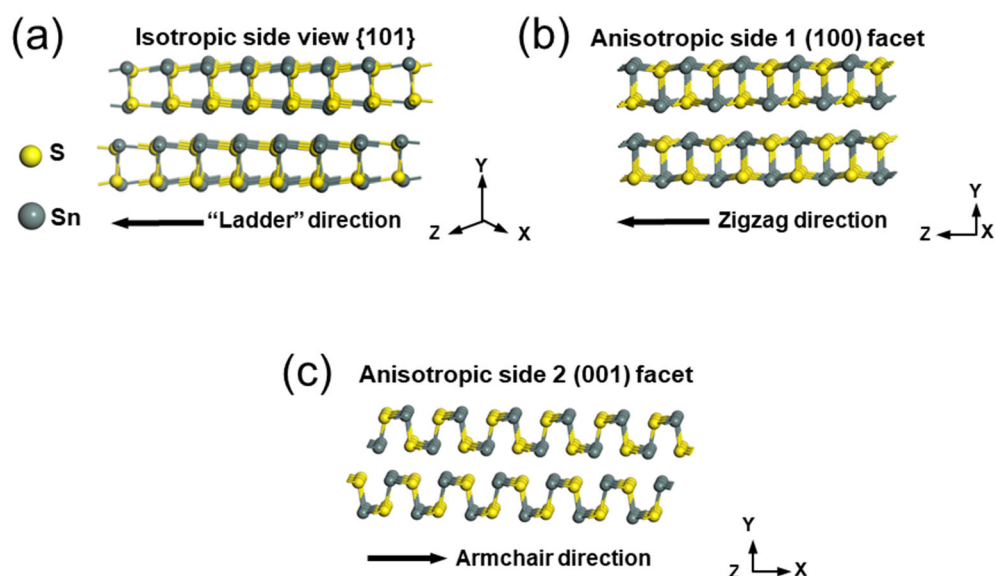
Figure 3.24. Atomic orderings of exposed facets parallel to the "ladder" direction (a), zigzag direction (b), and armchair direction (c) from the crystal structure of layered SnS NSs respectively. Reprinted with permission from [Fu Li, Mohammad Mehdi Ramin Moayed, Eugen Klein, Rostyslav Lesyuk, Christian Klinke. *J. Phys. Chem. Lett.* **2019**, 10(5), 993-999]. © 2019 American Chemical Society.
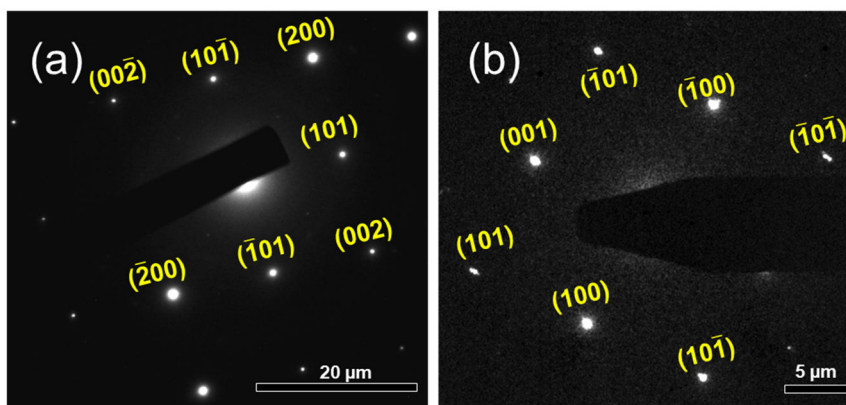
Figure 3.25. The SAED patterns of i-SnS (a) and a-SnS NSs (b) from Figure 3.23b. Reprinted with permission from [Fu Li, Mohammad Mehdi Ramin Moayed, Eugen Klein, Rostyslav Lesyuk, Christian Klinke. *J. Phys. Chem. Lett*. **2019**, 10(5), 993-999]. © 2019 American Chemical Society.

3.2.2 High-resolution TEM Characterization of Anisotropic SnS and Isotropic SnS Nanosheets

The SAED patterns can determine the exposed facets of the synthesized SnS NSs. HRTEM characterizations can furthermore confirm the exposed facets according to the measurable crystal fringes.

In terms of a-SnS NSs, the HRTEM measurements have been performed here to determine the exposed facets (see Figure 3.26). The selected area along the long side of a rectangular SnS NS was measured under HRTEM. The result shows a periodical lattice fringe of 0.20 nm which can be determined as (002) plane spacing (see Figure 3.26a-c). The HRTEM image of the selected area along the short side demonstrates the lattice spacing of 0.19 nm, matching the (00$\bar{2}$) facet. The *d*-spacings of 0.29 nm inside the crystal reveals nearly perpendicular in-plane planes (10$\bar{1}$) and ($\bar{1}$0$\bar{1}$) planes (see Figure 3.26b). Thus, it is confirmed that the long side is parallel to the (001) or (00$\bar{1}$) plane, whilst the short side is parallel to the (100) or ($\bar{1}$00) plane. This can be further proved and confirmed by the corresponding SAED pattern (see Figure 3.26d). Additionally, the a-SnS NS also owns four pairs of truncated corners which are parallel to the {101} planes.
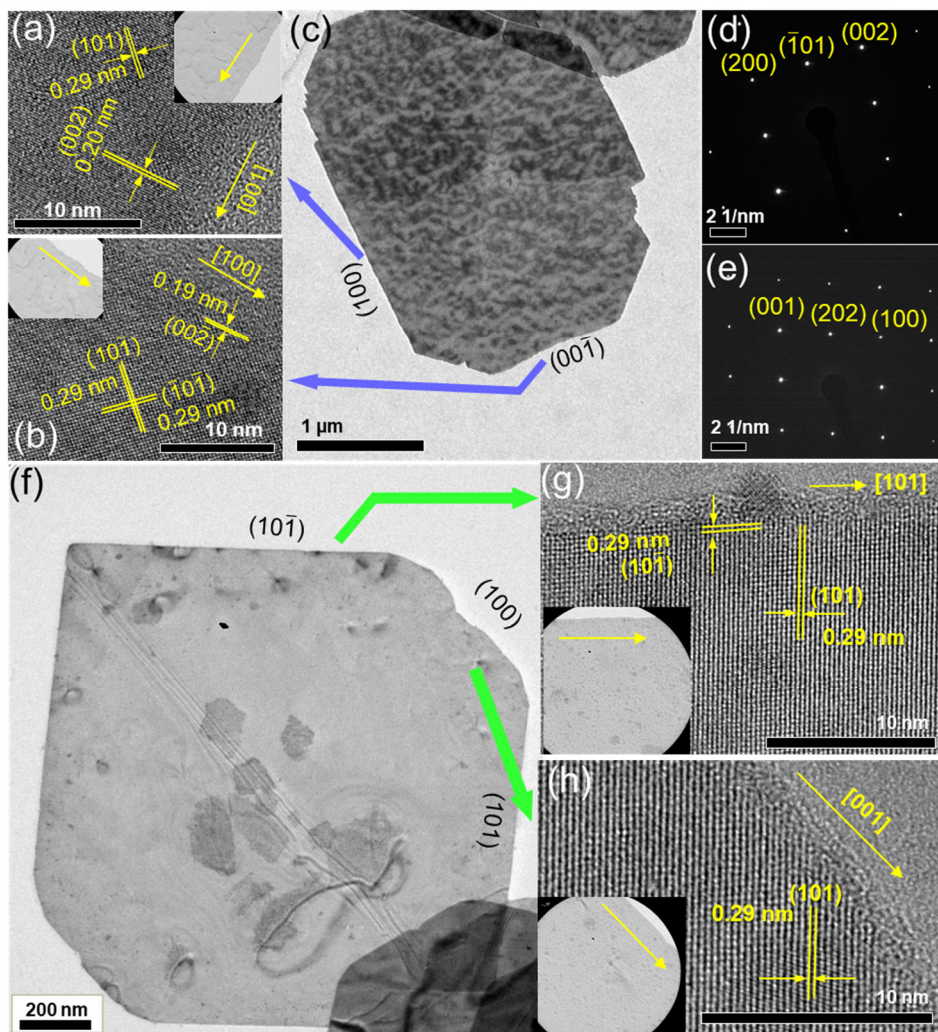
Figure 3.26. HRTEM images and the corresponding SAED patterns of a-SnS (a-d) and i-SnS NSs (e-h). Reprinted with permission from [Fu Li, Mohammad Mehdi Ramin Moayed, Eugen Klein, Rostyslav Lesyuk, Christian Klinke. *J. Phys. Chem. Lett.* **2019**, 10(5), 993-999]. © 2019 American Chemical Society.

The other type of SnS NSs, defined as i-SnS NSs, are synthesized by adopting 1.56 mmol of OA and 0.52 ml of 1 M TOP-S. The obtained NSs are rectangular SnS NSs with four edges parallel to the {101} planes which correspond to the "ladder" directions, as well as truncated corners parallel to (100) facets (see Figure 3.25). Similarly, the selected area along one side of the SnS NS was measured under HRTEM. It shows that the spacing of the periodical lattice fringes is 0.29 nm which can be determined as (10$\bar{1}$) plane (see Figure 3.26f, g), and truncated edges along the (100) planes (see Figure 3.26h).

3.2.3 Anisotropic/Isotropic SnS Transition

In Section 3.1 of this chapter, we have already studied the adsorption energies of each capping ligand and how they function in the anisotropic growth stage of isotropic square-shaped or hexagonal-shaped SnS NSs. In this section, we will describe an anisotropic growth of large and thin SnS NSs with tuned reaction parameters, to achieve two different edge-faceted nanosheets, or called in-plane anisotropic faceting.

Based on the taking-aliquot experiments, it was found that the size becomes larger and larger as the reaction time lasts, which is considered as a similar growth mechanism as the SnS NSs prepared in the first section (see Figure 3.27). Therefore, the anisotropic growth stage is considered to be manipulated by the capping ligands after the fast nucleation stage for the final formation of SnS NSs in this section. That is to say, the tuning of the capping ligand combination, can tune the growth direction of SnS NSs, which eventually governs the edge faceting.
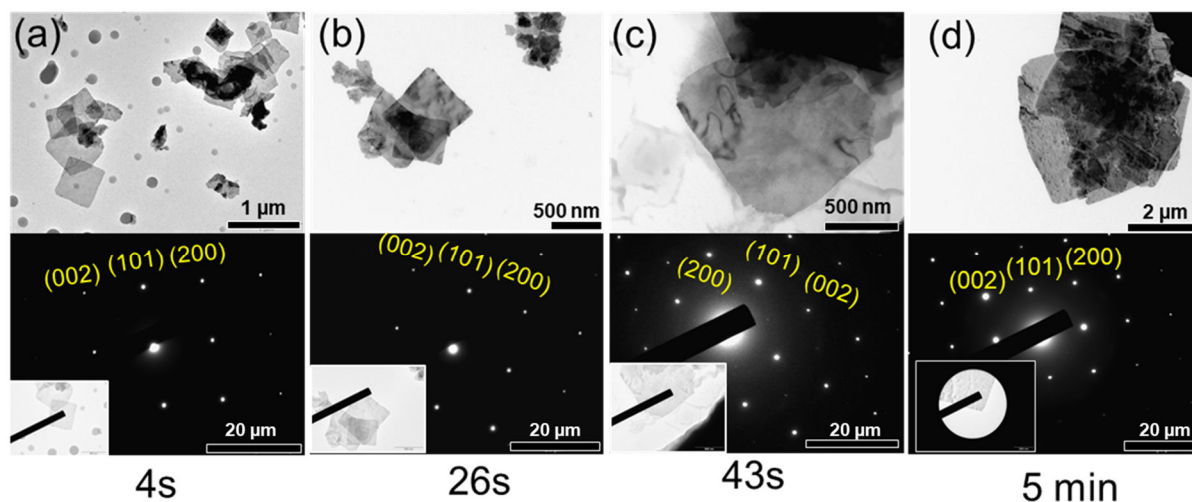
Figure 3.27. TEM images of the taken aliquots from the reaction solution of 4 s (a), 26 s (b), 43 s (c), 5 min (d) after the hot-injection is finished. Reprinted with permission from [Fu Li, Mohammad Mehdi Ramin Moayed, Eugen Klein, Rostyslav Lesyuk, Christian Klinke. *J. Phys. Chem. Lett.* **2019**, 10(5), 993-999]. © 2019 American Chemical Society.
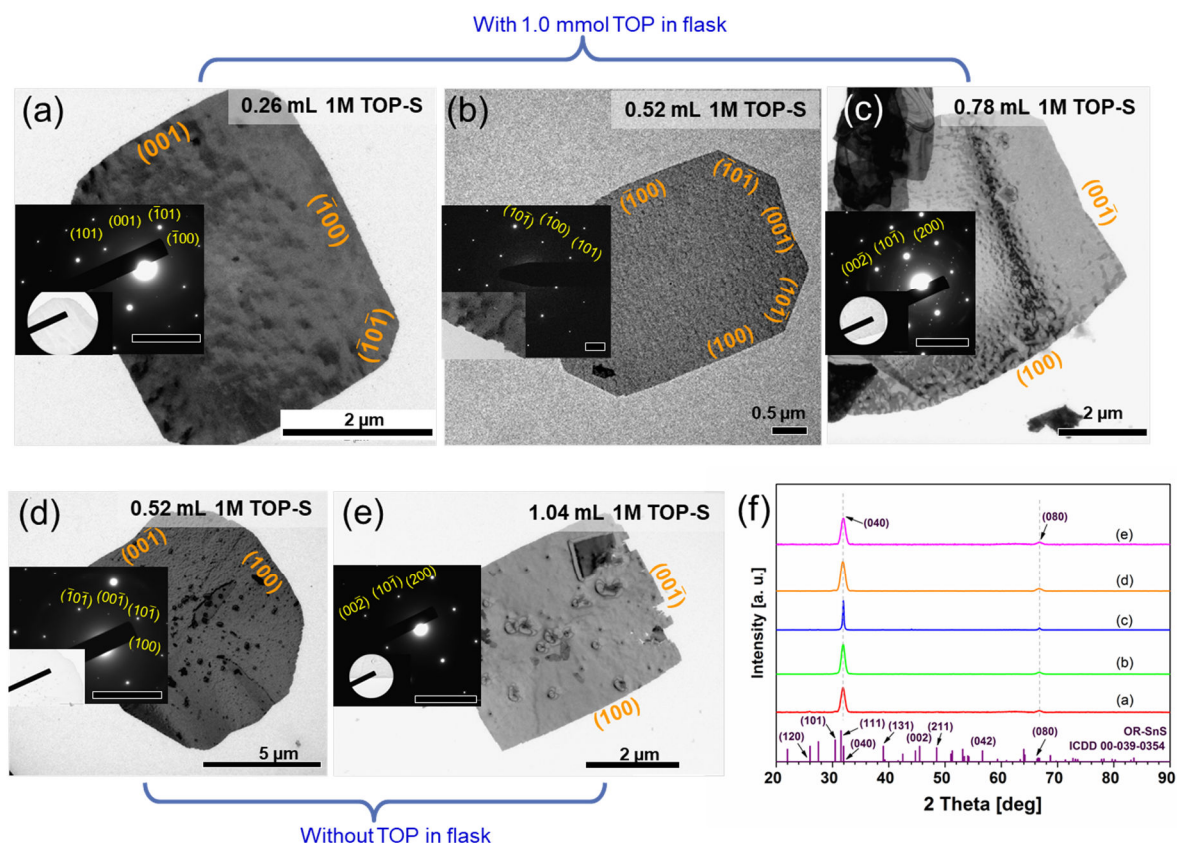
Figure 3.28. TEM images of the synthesized SnS NSs by varying the amount of TOP-S with 1.0 mmol TOP involved (a-c) and no TOP involved (d-e) respectively in the flask. Scale bar=20 μm, 5 μm, 20 μm, 20 μm, 20 μm for SAED patterns from the insets of a-e. (f) XRD diffractograms of the samples in a-e. Reprinted with permission from [Fu Li, Mohammad Mehdi Ramin Moayed, Eugen Klein, Rostyslav Lesyuk, Christian Klinke. *J. Phys. Chem. Lett.* **2019**, 10(5), 993-999]. © 2019 American Chemical Society.

In detail, the impacts of the OA and TOP amount (in the flask and in the TOP-S precursor solution) on the reaction have been investigated (see Figure 3.28, Figure 3.29, Figure 3.30). The more TOP-S, the larger and thicker a-SnS NSs are formed (0.26, 0.52, 0.78 ml, see Figure 3.28). Based on the XRD data, the calculated thicknesses are 10, 12, 36 nm respectively, whilst the corresponding AFM images reveal that the thicknesses are approximately 5 to 7 nm larger (partially shown in Figure 3.29). Intriguingly, with no TOP, and 0.64 mmol OA in the flask before hot-injection of TOP-S, only undefined-shaped NSs are obtained. The type of a-SnS NSs starts to form, which displays four definite rectangular edges without any truncated corners when the amount of TOP-S is increased to 1.04 mmol (see Figure 3.28e). Additionally, the lateral size reduces from almost 8 μm to 3.5 μm, while the thickness fluctuates between 8.9 to 9.3 nm from the XRD data.
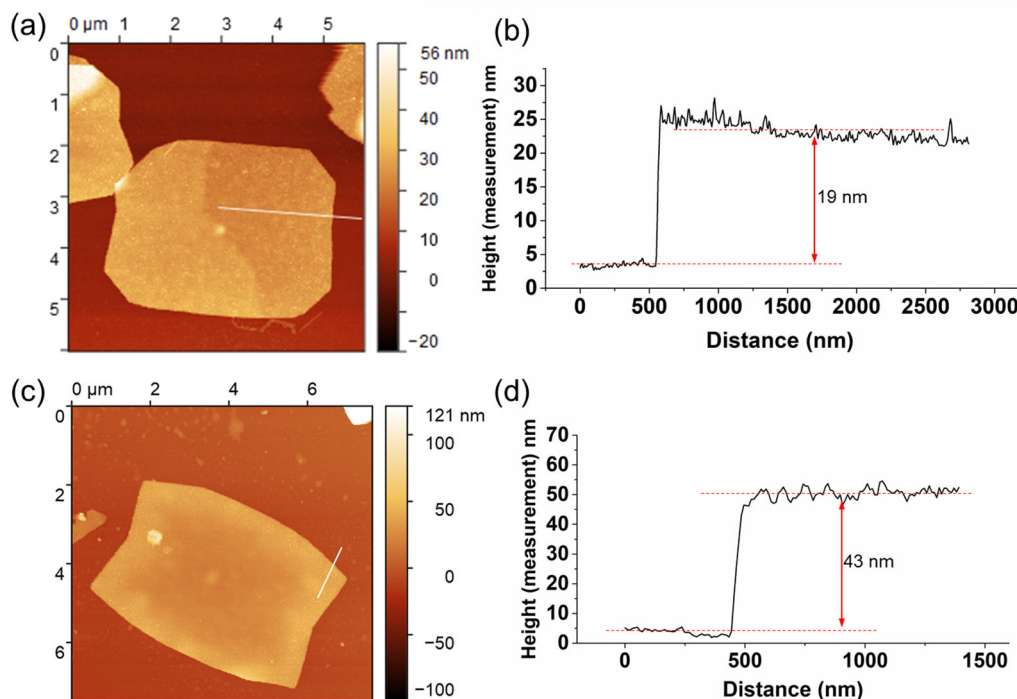
Figure 3.29. AFM images and the corresponding height measurements of the synthesized SnS NSs prepared by using 1.0 mmol TOP in the flask and 0.52ml (a, b), or 0.78 ml (c, d) of 1M TOP-S for the hot-injection during the reaction. Reprinted with permission from [Fu Li, Mohammad Mehdi Ramin Moayed, Eugen Klein, Rostyslav Lesyuk, Christian Klinke. *J. Phys. Chem. Lett.* **2019**, 10(5), 993-999]. © 2019 American Chemical Society.

Similarly, we have also investigated the synthesized SnS NSs with a variation of the amount of OA (0.64, 1.5, 2.0 mmol) without TOP put in the flask before the hot-injection process (see Figure 3.30). The undefined-edged NSs are synthesized with 0.64 mmol OA (see Figure 3.30a). In particular, the edge-faceting is switched to the isotropic type, leading to i-SnS NSs when 1.5 or 2.0 mmol of OA is used in the synthesis. Regarding the morphology, the size turns smaller upon the increasing OA amount, from 7.9 μm to 1.5 μm. Meanwhile, the thickness becomes larger from 8.9 nm to 17.6 nm and then even 27 nm, which is obtained from the XRD data (see Figure 3.30, partial AFM images in Figure 3.31). When 1.0 mmol of TOP is used together with 1.5 mmol of OA, i-SnS NSs are still formed, whereby the edges become more truncated, parallel to the (100) or ($\bar{1}$00) planes (see Figure 3.32).
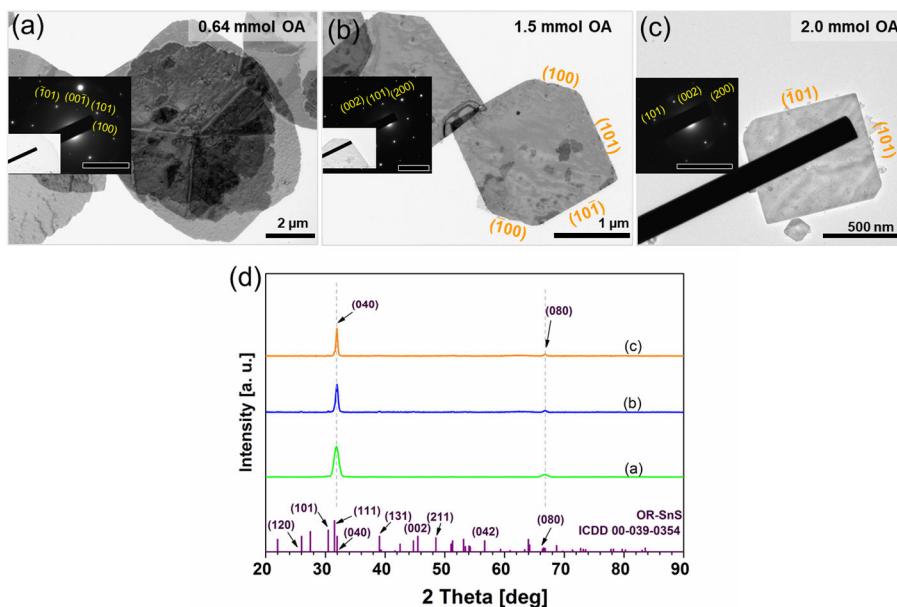
Figure 3.30. TEM images (a-c) and corresponding XRD diffractograms (d) of the synthesized i-SnS NSs by using respectively 0.64 mmol (a), 1.5 mmol (b), or 2.0 mmol (c) OA amount with no TOP in the flask before the injection of TOP-S precursor. Scale bar=20 µm for SAED patterns from the insets of a-c. Reprinted with permission from [Fu Li, Mohammad Mehdi Ramin Moayed, Eugen Klein, Rostyslav Lesyuk, Christian Klinke. *J. Phys. Chem. Lett.* **2019**, 10(5), 993-999]. © 2019 American Chemical Society.
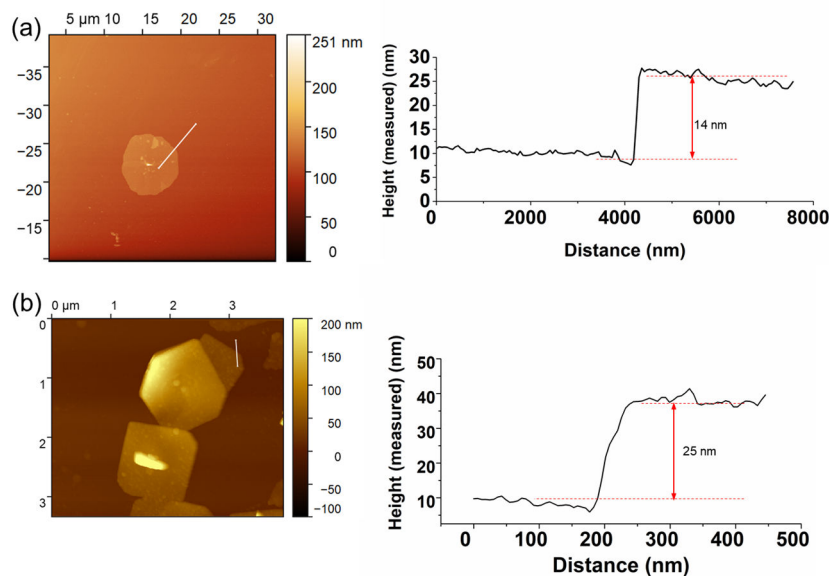
Figure 3.31. AFM images and the corresponding height measurements of synthesized SnS nanosheets. They are prepared with 0.64 mmol OA and no TOP (in the flask, a), and 1.5 mmol OA and no TOP (in the flask, b) during the reaction. Reprinted with permission from [Fu Li, Mohammad Mehdi Ramin Moayed, Eugen Klein, Rostyslav Lesyuk, Christian Klinke. *J. Phys. Chem. Lett.* **2019**, 10(5), 993-999]. © 2019 American Chemical Society.

Theoretically, binding affinities of capping ligands on specific facets can drive the anisotropic growth to specific directions, forming specific preferred morphologies.[154-155] The a-SnS NSs are produced under the circumstance that the growth speeds on the {101} facets are much higher than those on the (100), (001) and their parallel ($\bar{1}$00) and (00$\bar{1}$) facets, which are strongly passivated by OA.[129] Differently, i-SnS NSs are formed under the condition that the growth speeds along the [100] (or [$\bar{1}$00]) and [001] (or [00$\bar{1}$] directions are relatively fast compared to those on the {101} facets. To support this, DFT simulations have been conducted to study the possible mechanism of the edge faceting phenomena according to the adsorption energy of capping ligands on the main facets of SnS (see Table 3.2).
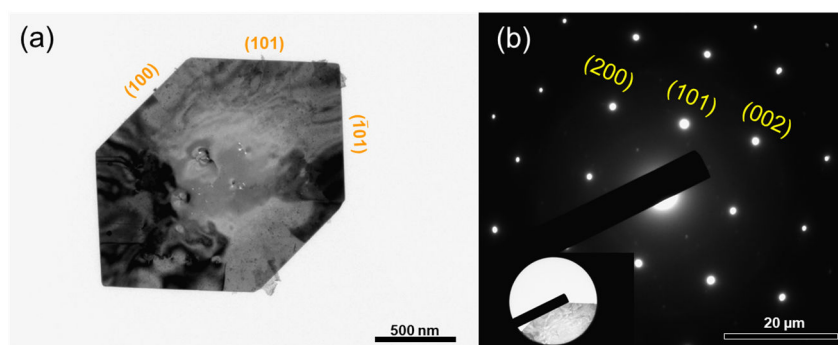
Figure 3.32. TEM image and the corresponding SAED pattern of the synthesized SnS nanosheets prepared with 1.5 mmol OA and no TOP (in the flask) in reaction, together with a high amount of oleic acid (1.5 mmol). Reprinted with permission from [Fu Li, Mohammad Mehdi Ramin Moayed, Eugen Klein, Rostyslav Lesyuk, Christian Klinke. *J. Phys. Chem. Lett.* **2019**, 10(5), 993-999]. © 2019 American Chemical Society.

Different from the previous section where TAA was used as the sulfur precursor for the i-SnS NS synthesis, in this recipe TOP-S as the sulfur precursor was found to be the key to obtaining a-SnS NSs. In terms of TAA involved synthesis, i-SnS NSs can be synthesized via the combined passivation of capping ligands including oleate, TOP, and OA according to the high adsorption energy of TOP and oleate on the {101} and (100) facets. Herein, the formation of a-SnS NSs is mainly based on the high adsorption abilities of TOP-S on the (100), (001) facets (see Table 3.2), which can sterically hamper the pathway of SnS monomers towards the nuclei surfaces, subsequently slowing down the growth of those facets. It then results in the specific faceting with exposed edges along anisotropic directions instead of isotropic directions.[150]

Table 3.2. Adsorption energy [eV] of capping ligands on each facet of SnS crystals via the calculation based on the Density of Functional Theory (DFT) method. The simulations were performed by adopting simplified molecules for TOP as well as TOP-S (triethylphosphine TEP, tripropylphosphine TPP, tributylphosphine TBP) with different chain lengths (C2, C3, and C4). They reveal similar tendencies. Reprinted with permission from [Fu Li, Mohammad Mehdi Ramin Moayed, Eugen Klein, Rostyslav Lesyuk, Christian Klinke. *J. Phys. Chem. Lett.* **2019**, 10(5), 993-999]. © 2019 American Chemical Society.

|	SnS-101 side facet (isotropic)	SnS-100 side facet (anisotropic, zigzag)	SnS-001 side facet (anisotropic, armchair)	SnS-010 top facet (Top or down)
TPP	1.939	1.503	1.551	0.675
TPP-S (C3)	1.740	2.390	1.799	0.927
TEP-S (C2)	1.660	2.183	1.657	1.118
TBP-S (C4)	1.972	2.761	2.067	1.364

The introduction of TOP-S into the reaction system has a strong impact on the surface of the SnS crystal, preferentially stabilizing the (100) and (001) facets. This will slow down the growth speed of these influenced facets. That is why eventually these facets are more stable and grow less fast compared to other facets, turning out to be the final exposed facets for the final nanosheets.[150] In addition, the DFT simulations using simplified molecules with different chain lengths displays similar tendencies (see Table 3.2).

Furthermore, the in-plane faceting from a-SnS to i-SnS can be realized by tuning the OA amount even in the presence of TOP-S. This phenomenon is also supported by the DFT simulations in the previous section which reveal that high adsorption energy of oleate on (100) and {101} facets. It eventually results in the formation of square-shaped nanosheets with truncated (100) corner edges when the OA amount is large enough for the ligand replacement on specific facets.

3.2.4 Anisotropic Transport Measurements

The zigzag and armchair directions of the synthesized SnS NSs were then investigated in terms of the presence of electronic anisotropy (see Figure 3.33).[123] To measure the transport properties along different crystallographic directions, individual sheets were picked to be contacted and measured at room temperature. In one group, four contacts were placed parallel to the side edges, to get the conductivity value along the anisotropic directions (see Figure 3.33a). For another group of devices, the contacts were placed from corner to corner, to investigate the isotropic directions (see Figure 3.33b).
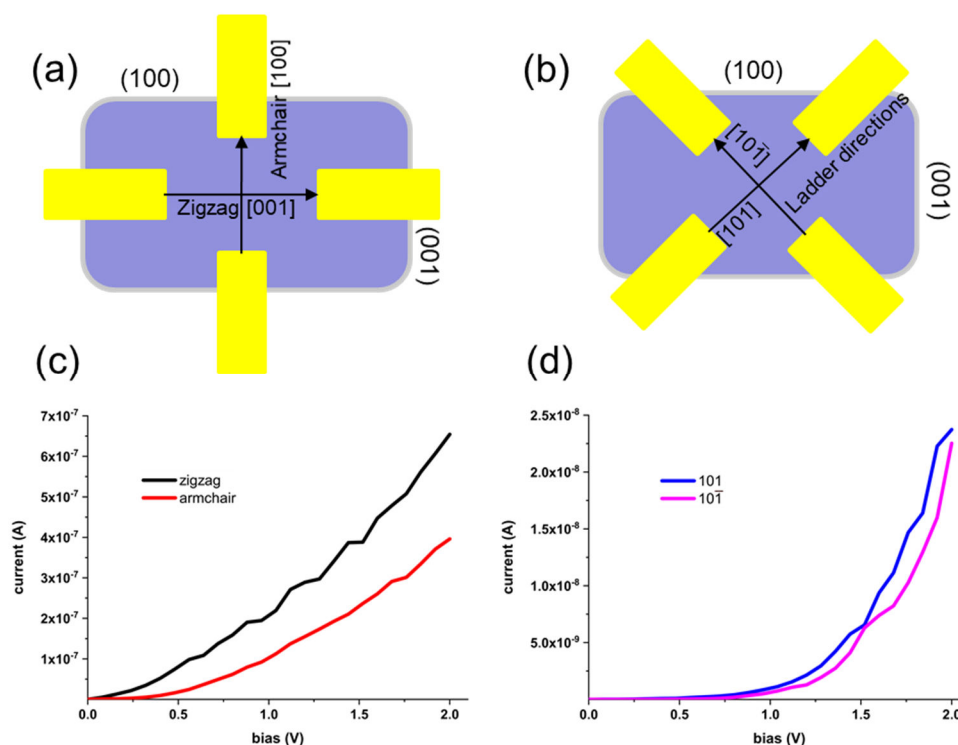
Figure 3.33. Electrical measurements conducted along two pairs of directions. Schematic illustration of the nanosheets, contacted along anisotropic directions (a) and along isotropic directions (b). The I-V characteristics measured along anisotropic directions. It exhibits a higher conductivity along the zigzag direction compared to that along the armchair direction (c). (d) The I-V characteristics measured along isotropic directions, displaying similar conductivities along two "ladder" directions. Reprinted with permission from [Fu Li, Mohammad Mehdi Ramin Moayed, Eugen Klein, Rostyslav Lesyuk, Christian Klinke. *J. Phys. Chem. Lett.* **2019**, 10(5), 993-999]. © 2019 American Chemical Society.

The I-V characteristics of the NSs along both pairs of directions are shown in Figure 3.33c, d. The conductivity along the zigzag direction [001] reaches 65 S/m, whilst the conductivity along the

armchair direction [100] is 39 S/m. The ratio of these two conductivities is calculated to be 1.67, which is also consistent with values from the literature.[123] The effective masses of the carriers (mainly holes) are substantially different along these two pairs of directions.[124, 130, 156] The carriers have a higher mobility along the zigzag direction, leading to a higher conductivity.[123] However, the conductivities along the "ladder" directions [101] and [10$\bar{1}$] are shown to be quasi-isotropic, respectively 2.2 and 2.3 S/m (see Figure 3.33d). This is due to the fact that the atom arrangements along these two directions are equal, which results in a comparable electrical conductivity.

Hence, the simple confirmation of different conductivities for each crystallographic direction has been performed. The results show an in-plane electronic anisotropy in terms of conductivity along the zigzag and armchair directions, but an in-plane isotropic behavior from corner to corner, along "ladder" directions.

3.3 Synthesis and Characterization of Two-dimensional SnTe nanostructures

■ *The results discussed in the following chapter have already been summarized as another paper named "Colloidal synthesis of two-dimensional narrow-gap semiconductor tin telluride nanostripes and nanosheets". This article is still in progress for submission.*

3.3.1 Synthesis and Basic Characterizations

The synthesis of 2D SnTe cannot be achieved by simply replacing TOP-S with TOP-Te using previous recipes for SnS syntheses. This is due to the different precursor reactivity as well as diverse chemical, physical properties of different element atoms. Similarly, it has been reported that TOP-Te has a quicker cleavage rate than TOP-S, which leads to the formation of more nuclei and faster exhaustion of monomers.[157] This cleavage-rate difference can also be found in the incubation time (Te needs much longer time than S) when we try to dissolve chalcogen elements in the solvent TOP. However, a fast cleavage of Te precursor is not suitable for anisotropic growth and will result in 3D bulk structures instead of 2D morphology (shown later in this section).

Thus, some other parameters need to be introduced here to achieve 2D SnTe nanostructures. The tin precursor used here is still tin acetate, which is not flammable and highly reactive. The tellurium (Te) precursor applied here is elemental Te dissolved in TOP solution. In a typical reaction, 0.25 mmol of TA, 6.4 mmol of OA and 1.0 mmol of TOP were mixed in the flask with 10 ml of DPE as the solvent. Before heating up the system to the reaction temperature 250 ℃, 1-bromotetradecane (1-BTD) was added to introduce halide molecules into the reaction. Then the hot-injection of Te precursor TOP-Te took place, followed by a quick color change from yellow to greyish yellow or even grey. Eventually, the reaction was cooled down for collection and purification.
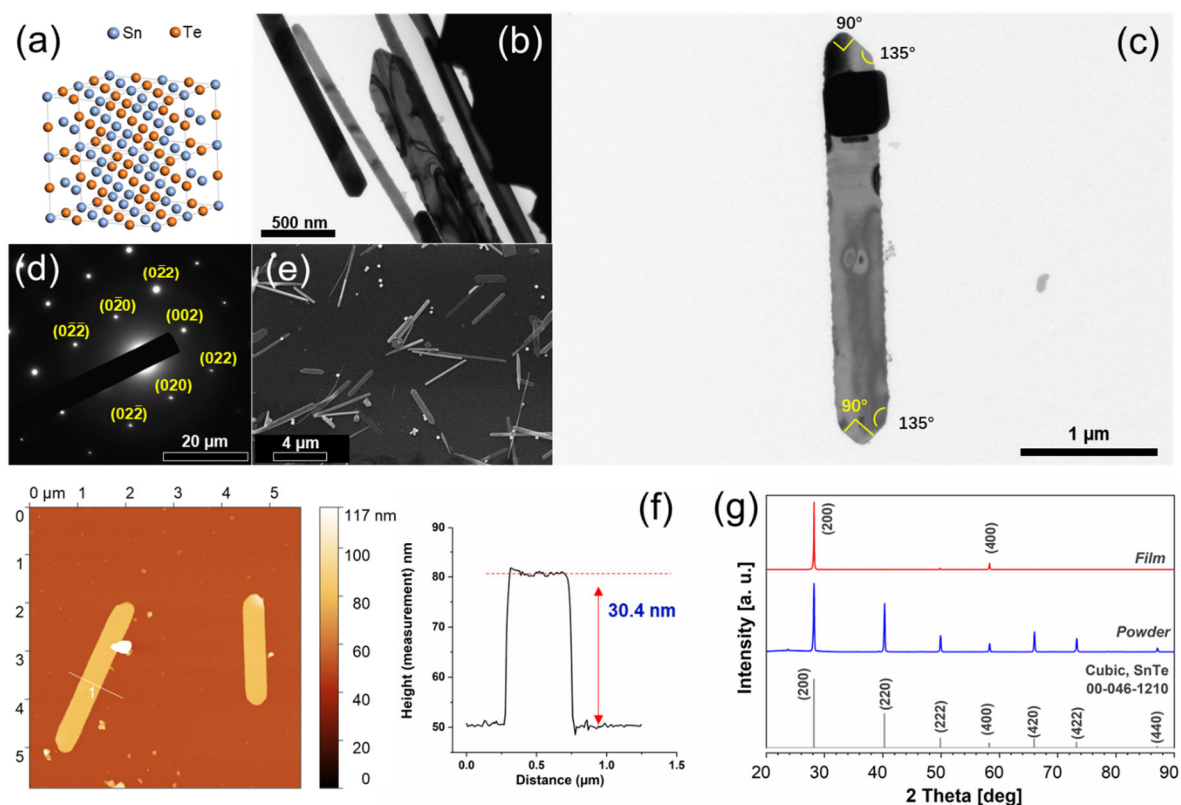
Figure 3.34. (a) Atomic models of the crystal structure of SnTe nanocrystals. (b-d) TEM images, SAED pattern and overview of SEM image (e) of SnTe nanostripes. (f) AFM image and the height line scan measurement. (g) XRD diffractograms of SnTe samples prepared by drop-casting and in a capillary tube.

The synthesized product mainly contains 2D elongated SnTe nanostripes, along with some elongated SnTe nanorods (see Figure 3.34). The SnTe atomic model exhibits a rock-salt crystal structure of SnTe nanocrystals (see Figure 3.34a). This is the typical cubic phase β-SnTe.[158] TEM images and the corresponding SAED pattern show a nanostripe morphology and high crystallinity of the synthesized SnTe nanocrystals (see Figure 3.34b, c, d). Based on the SEM image, the calculated mean length of the dispersed nanostripes is 3.2 μm, and the stripe length ranges from 1.5 μm to even 5.8 μm (see Figure 3.34e). The AFM image reveals that the stripes have a relatively flat surface and the measured height or thickness of the stripes is around 30 nm (see Figure 3.34f). Powder X-ray diffraction of a dry sample in a capillary tube shows well-matched diffraction reflexes, which can be indexed to cubic SnTe (*Fm3m*, 225, 00-046-1210), whilst the XRD diffractogram of the drop-casted sample exhibits periodical pronounced reflexes which correspond to (200) and (400) because of the texture effect (see Figure 3.34g). This indicates that

nanostripes laying perpendicular to the [100] directions and the flat lateral surface is the (100) facet. Theoretically, the cubic crystal system owns the same a, b, c values, so it presents the same ordering among all the {100} family. Thus, the thickness orientates along one direction from all the <100> directions. We define here the thickness direction orientates along the [100] directions in this thesis. In addition, the measured angles of the edges and side-edge are approximately 90° and 135° in Figure 3.34c.
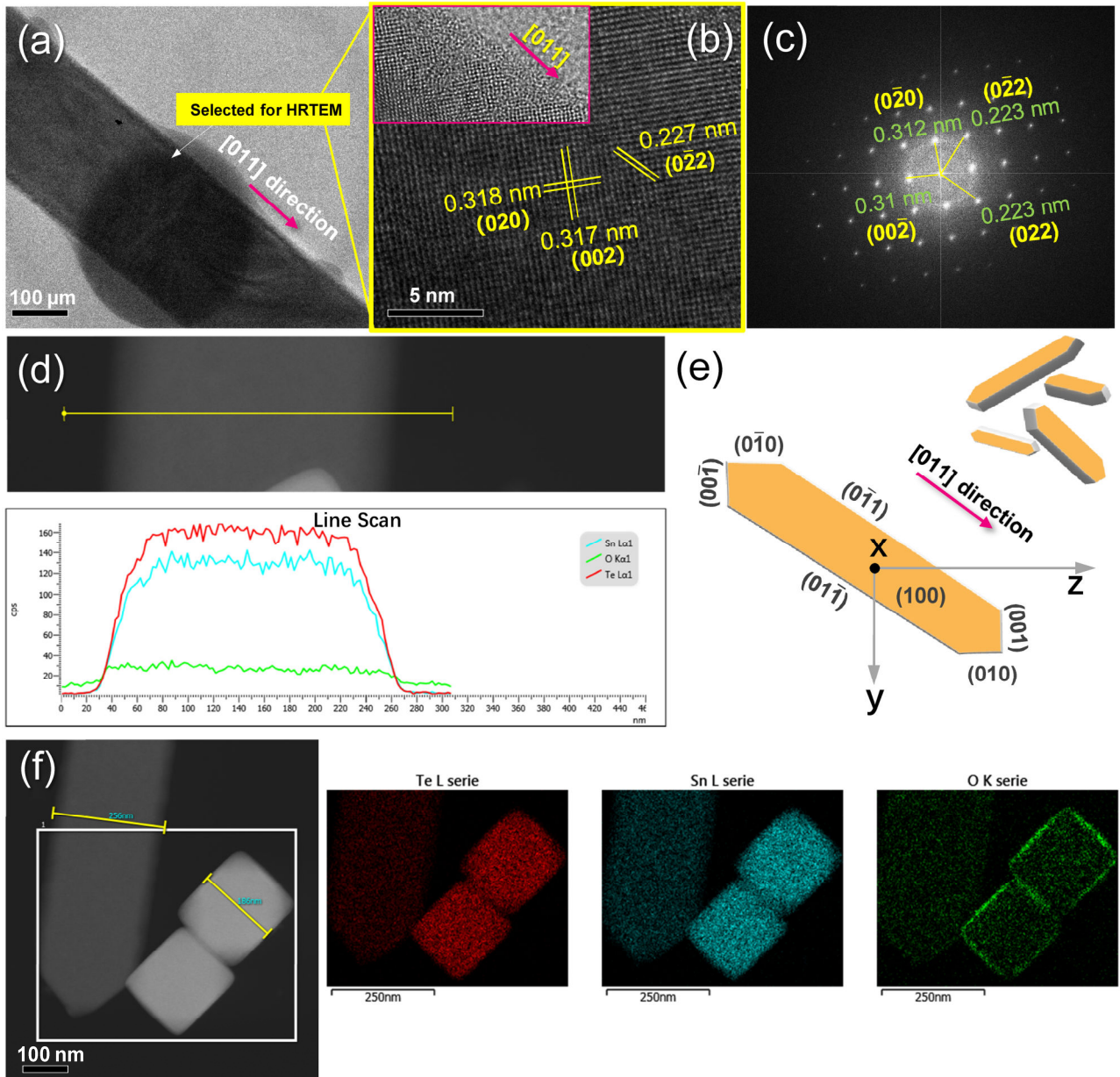
Figure 3.35. HRTEM characterizations of SnTe nanostripes and the corresponding FFT analysis (a-c). (d) EDX line scan of the nanostripes with element distributions for Sn, Te, and O. (e) Schematic representative of SnS nanostripes with determined exposed facets marked above. (f) EDX mapping analysis of the selected areas for SnTe nanostripes and nanocubes with the elements Sn, Te and O measured.

HRTEM characterization and elemental analysis have been conducted to investigate the lattice details and the elemental distribution of SnTe nanostripes (see Figure 3.35). An HRTEM image of a selected area which is near the side of one typical nanostripe demonstrates clear lattice fringes of perpendicular planes. The measured d-spacings of these two perpendicular planes are approximately 0.317 and 0.318 nm, referring to the (002) and (020) facets (see Figure 3.35a, b). The lattice spacing of 0.227 nm indicates the side edge is parallel to the (0$\bar{1}$1) facet. These determined facets can also be confirmed by the corresponding FFT analysis in Figure 3.35c.

In Figure 3.35e, nanostripes with determined exposed facets are marked. The EDX line scan, mapping analysis and elemental analysis of the nanostripes and nanocubes were conducted as shown in Figure 3.35d, f and Figure 3.36. They display a highly stoichiometric ratio of Sn and Te, which is 1: 1.005 (another EDX shows the ratio of 1: 1.012) for the SnTe nanostripe, and 1.015: 1 for the SnTe nanocube (byproduct).

Interestingly, there is also a certain amount of oxygen detected. A shell layer of oxygen atoms with a high intensity can be observed around the SnTe nanocubes, while merely even distributed oxygen atoms are mapped with a low intensity on the SnTe nanostripe. This may result from the fact that the thickness of the cubes is much higher than the nanostripes (see Figure 3.35f). This thin layer of oxygen has also been reported by Klimov's group.[135] They demonstrated that the outer layer on their nanocrystals contain no Te but the element O according to the mapping analysis and assumed an SnO_x shell of about 2 nm on the surface of the synthesized SnTe nanocrystals.

In addition, we measured the side length of the SnTe nanocubes' squared patterns and the width of the SnTe nanostripe's pattern based on the EDX mapping analysis (see Figure 3.35f). The results indicate that the side length of dot squares of Sn and O were measured to be slightly larger than that of Te, which may be one supportive evidence of the presence of an SnO_x shell around the SnTe nanostripes and SnTe nanocubes.

Element	Linientyp	k-Faktor	k-Faktor-Typ	Absorptionskorrektur	Massen%	Massen% Sigma	Atom %
O	K serie	1.455	Theroretisch	1.00	2.42	0.05	16.03
Sn	L serie	1.890	Theroretisch	1.00	46.73	0.12	41.72
Te	L serie	1.983	Theroretisch	1.00	50.85	0.12	42.24
Gesamt:					100.00		100.00
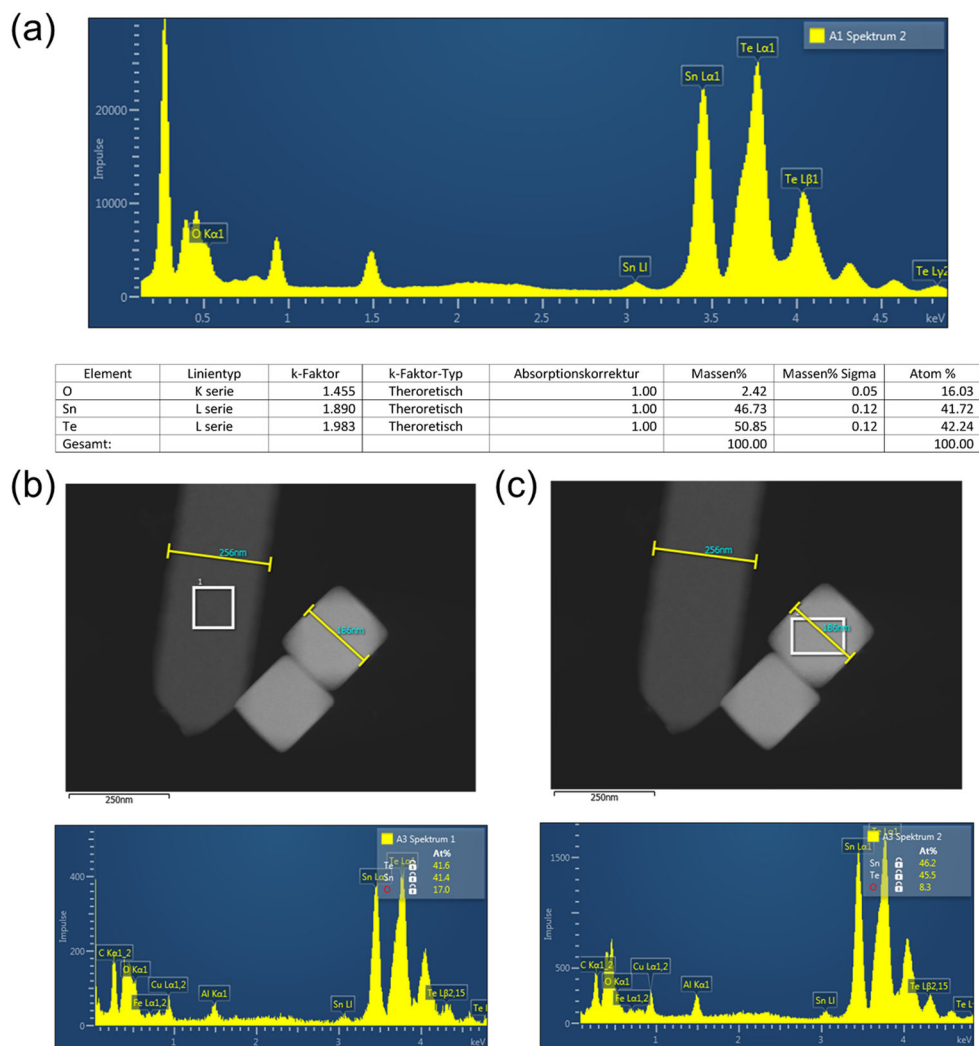
Figure 3.36. EDX elemental analysis of the synthesized SnTe nanostripes (a, b) and the byproduct SnTe nanocubes (c).

In addition, the morphology evolution has also been investigated by taking aliquots at different point in time during the reaction (see Figure 3.37). At the early stages (shorter than 30 s), no defined nanostructures with cubic phase were observed. There were only some irregular small-sized particles with weak patterns of crystalline SnO_2 instead (Figure 3.38) together with amorphous parts under the TEM (see Figure 3.37a, b). Later, defined-shaped nanostripes started to appear with a length of 2 μm and a width of approximately 100 to 180 nm. When the reaction time lasted 3.5 min, longer and wider nanostripes were formed, from which the largest ones can reach 3.8 μm and 1.2 μm in length and in width respectively. However, there were also fewer cubes formed when the reaction continued, demonstrating the dominance of the intrinsic cubic phase in facilitating the crystal morphology.[159] This morphology evolution study gives a referable hint

that the formation of SnTe nanostripes takes its rise from a fast nucleation and anisotropic growth process, which is similar to the SnS NS formation mentioned in Section 3.1 and Section 3.2.
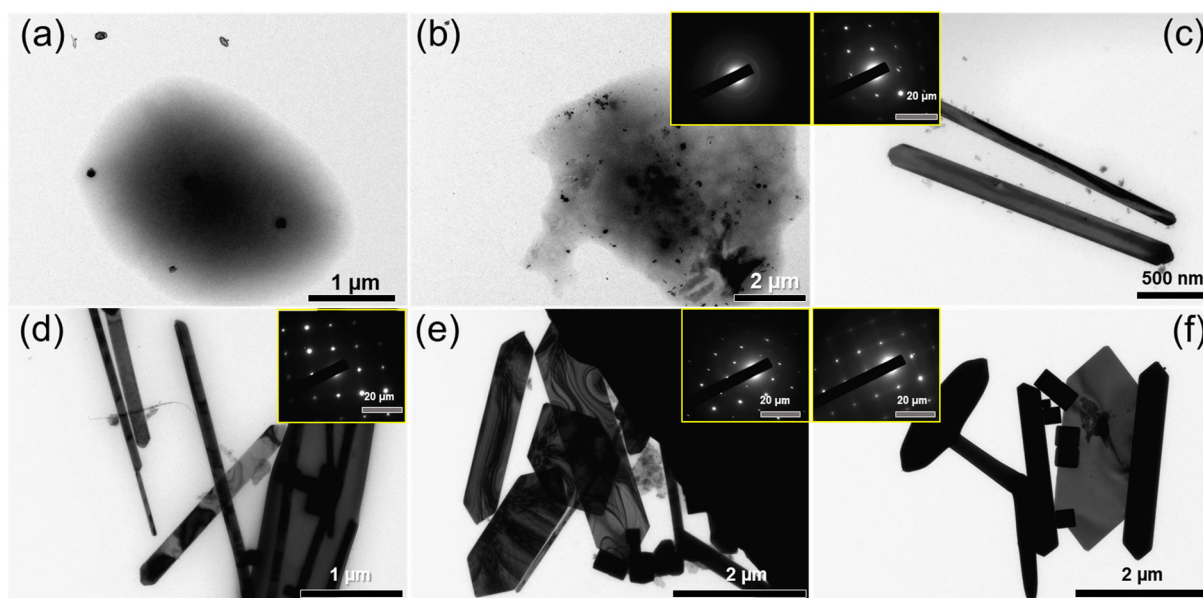
Figure 3.37. TEM images and SAED patterns of the sample taking from the reaction at (a) 5 s, (b) 30 s, (c) 1 min, (d) 1.5 min, (e) 3.5 min after the hot-injection of TOP-Te precursor. (f) TEM image of the sample collected after cooling down procedure with 3.5 min reaction time.
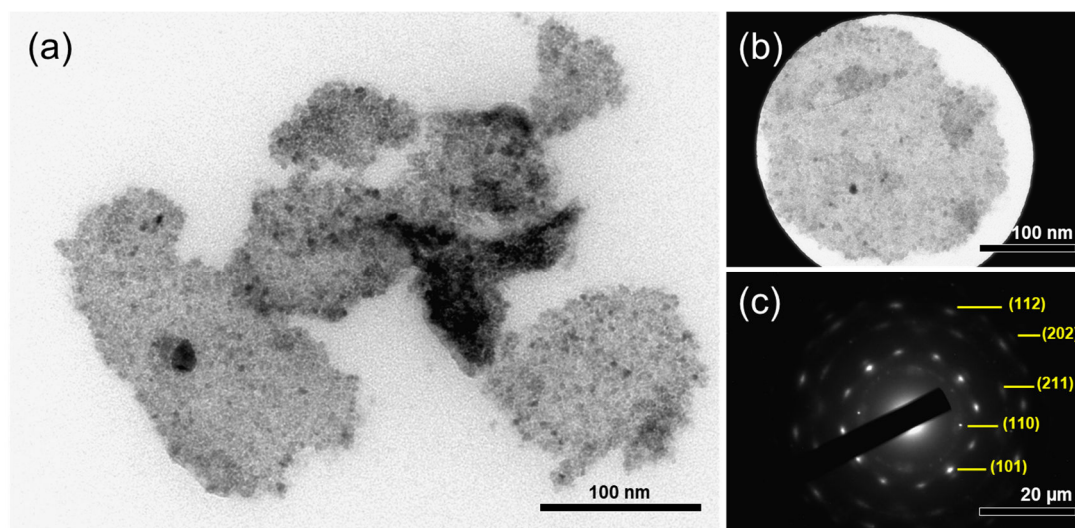
Figure 3.38. TEM images (a, b) and SAED pattern (c) of the aliquots taken after 5 s of reaction. (c) The pattern is analyzed and determined with marked facets, matching the electron diffraction pattern of SnO_2 crystal structure including (110), (101), (211), (202), (112) facets.

3.3.2 Influence of the 1-BTD Amount on the Shape Evolution

In this section, a new ligand strategy is applied by introducing halide ligands, compared to the synthesis of SnS in previous sections. As is well known, the nucleation and growth process of the synthesized nanocrystals often happen with the aid of involved ligands and salts in the solution. However, it is difficult to clarify the individual influence from each involved reactant.[142] The introduction of new surfactants, even in tiny amounts, will still change the whole kinetics of the nucleation and growth of these nanocrystals. In the previous two sections, we clearly demonstrated the importance of understanding the surface energies of each facet for the final formation of specifically shaped nanocrystals. It has been explained in terms of adsorption energies of different ligands (*e.g.* OA and TOP) involved in SnS nanosheets formation.

In particular, halide ions, either from salts or from halide alkanes, are surfactants which are also good alternatives for modifying the crystal surfaces or facets based on their extraordinary properties such as high electronegativities.[142, 160] Among all the widely used surfactants such as OA, TOP or acetate groups (OAc⁻), halide ions display relative high reactivities due to their ionic nature.[142] This can also explain some interesting phenomena including that why some extreme morphologies can be smoothly realized by involving halides, for example, 2D PbS nanosheets synthesized with halide alkanes.[88]

Theoretically, there are several ways for halide ligands to influence the nucleation and growth of nanocrystals regarding thermodynamic and kinetic control, including the specific binding preference, the interaction with precursor ions by complexation, and also the etching process.[142] Owing to the nature of halide ions, the specific binding preference normally focuses on the metal atoms on the surface of nanocrystals. The interaction with precursor ions by complexation often benefits from the solution-based reaction, making the contact between halide atoms and metal atoms (from the precursor) much easier. Therefore, the occurrence of complexation of halide atoms and metal atoms become inevitable in the solution-based reaction. Nevertheless, this interaction can also affect the nucleation and growth stage, for instance, by cutting down the monomer-producing rate from the precursor-complex, which afterwards makes the growth process slower. This, in turn, leads to another possible pathway of etching. The re-dissolving of

the surface atoms into the solution can return to the complexation of metal-halide complexes. The etching process is the third way for halide ligands to work during the growth stage of nanocrystals.[142] Hence, introducing halide ligands into the synthesis of SnTe will be intriguing and worth trying for obtaining 2D SnTe nanostructures with the cubic phase which presents a high symmetry.
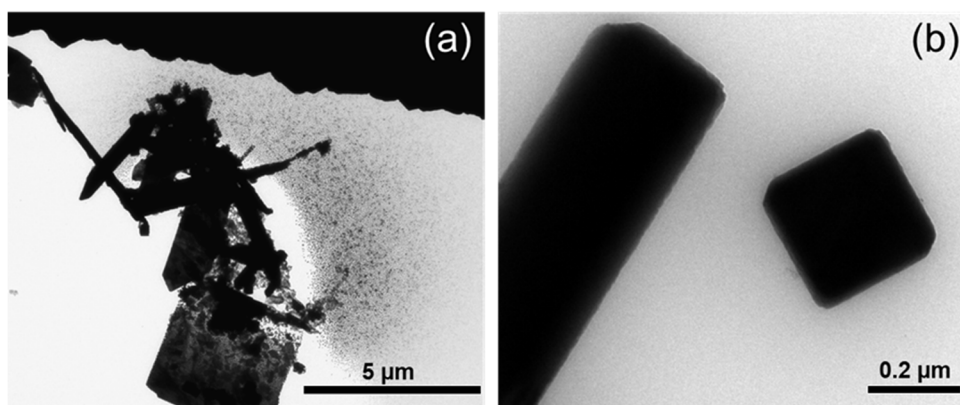
Figure 3.39. TEM images of the structures synthesized at the reaction temperature of (a) 200 ℃, and (b) 300 ℃, using no 1-BTD compared to standard SnTe recipe with 1-BTD.

In terms of the synthesis using no 1-BTD to check the necessity of applying halide alkanes (see Figure 3.39), the TEM images show that only agglomerates and 3D microstructures can be formed. Thus, involving halogenated compounds like 1-BTD is necessary to obtain well-defined 2D SnTe nanostripes. Furthermore, the variation of 1-BTD amount has also been performed to observe the impact of halide ligands and to optimize the amount of 1-BTD (see Figure 3.40). There are only irregular-shaped platelets synthesized, along with long rods and several cubes, when the amount of 1-BTD is equal or lesser than 0.64 mmol (see Figure 3.40a, b). When the amount of 1-BTD reaches 0.64 mmol, the product mostly exhibits the morphology of 2D elongated nanostripes with few cubes and long nanorods (see Figure 3.40c). Nevertheless, a larger amount of 1-BTD leads to larger numbers of long rods or wires with reduced number of nanostripes (see Figure 3.40d). This implies that 1-BTD in a small amount cooperating with OA and TOP in the solution tends to passivate the (100) facets and presents less passivation on (010) and (001) than (0$\bar{1}$1), or (01$\bar{1}$) as co-ligand. It prompts the nuclei to form nanostripes with the aid of co-ligands in the anisotropic growth process (see Figure 3.35a, e). More 1-BTD will exchange the original OA and TOP in specific facets, easing the strong passivation on {100} facets and (0$\bar{1}$1). This finally results

in the formation of longer nanorods. Additionally, more 1-BTD could make the texture effect slightly less apparent according to the corresponding XRD data (see Figure 3.40e).
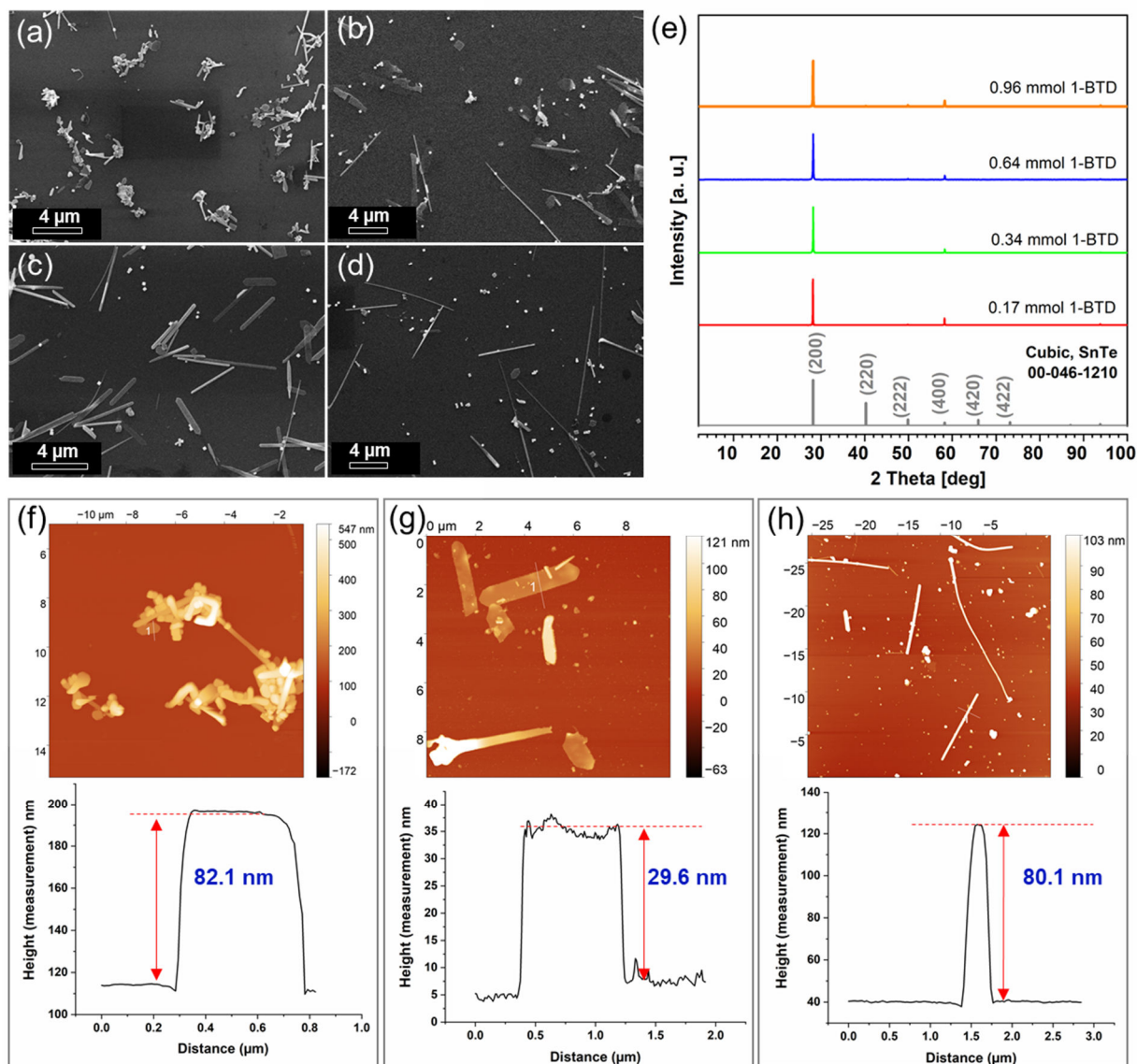
Figure 3.40. SEM images (a-d) and the corresponding XRD (e) and AFM measurements (f-h, f refers to a, g refers to b, h refers to d) of the SnTe nanostructures synthesized using (a) 0.17 mmol, (b) 0.34 mmol, (c) 0.64 mmol, (d) 0.96 mmol BTD.

Theoretically, halide ions can be released from the halide alkanes during the reaction, acting as X-type ligands as well as Z-type ligands, which has been proven by our group.[161] In our case, Br^- ligands can bind as X-type ligands to Sn^+ cations on the surface, directly passivating the surface. But Br^- and the excess Sn^+ can also form a $SnBr_2$ complex as Z-type ligand, similar to $CdCl_2$.[142, 162] Thus, the halide ions competing with oleate or phosphine ligands can change the surface energy

of SnTe nanocrystals during the thermodynamic growth stage. This can finally result in the favorable 2D nanostructures after co-passivation with other involved ligands.

AFM measurements have been conducted as shown in Figure 3.40f-h, to investigate the height evolution of synthesized SnTe nanostructures with the variation of the amount of 1-BTD mentioned above. The nanostructures produced with 0.17 mmol 1-BTD show differently shaped platelets and particles like small agglomerates with large size (~82.1 nm, see Figure 3.40f). The nanostripe synthesized using 0.34 mmol 1-BTD displays a similar thickness (~32 nm) to that of the synthesized SnTe nanocrystals with 0.64 mmol 1-BTD (considered as the standard synthesis). However, long nanorods present a relative round cross-section with a diameter around 80 nm (see Figure 3.40h), exhibiting a similar morphology to that of the rods obtained from the standard synthesis (~90 nm, Figure 3.41).
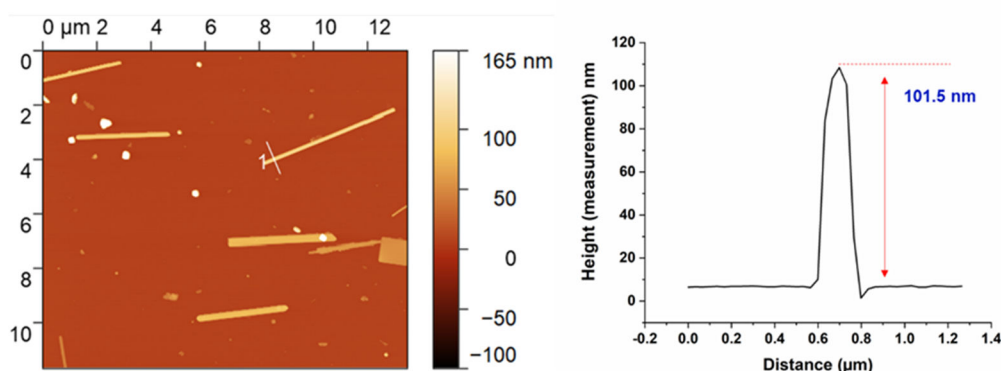
Figure 3.41. AFM image and the height profile of the long rod-like structure from the standard SnTe-nanostripe synthesis.

Afterwards, it has also been observed that 1-chlorotetradecane (1-CTD) can also help to form 2D SnTe nanostructures as does 1-BTD (see Figure 3.42). By tuning the reaction temperature from 170 ℃, to 220 ℃, and to 260 ℃, the obtained products display a clear shape evolution from thin square-like shape (40 nm thick), to thick square or irregular shape (112.7 nm thick), and further to thick elongated stripes (99.1 nm) (see Figure 3.42). The corresponding XRD diffractograms for the samples from 1-CTD experiment series show pronounced (200) and (400) reflexes, exhibiting strong texture effect (see Figure 3.43). As is well known, the nucleophilicity increases in the line Cl⁻ < Br⁻. During the reaction, Br⁻ will be released much easier than Cl⁻ ions from the original

halide alkane molecules, resulting in higher amounts available at the early stage.[163] This will finally lead to a higher destabilization by Br⁻ ions on the crystal surface than that of Cl⁻ ions, and a more enhanced anisotropic growth. Hence, the syntheses using 1-CTD turned out to possess a lower yield of 2D nanostructures, which present larger thicknesses (see AFM data in Figure 3.42).
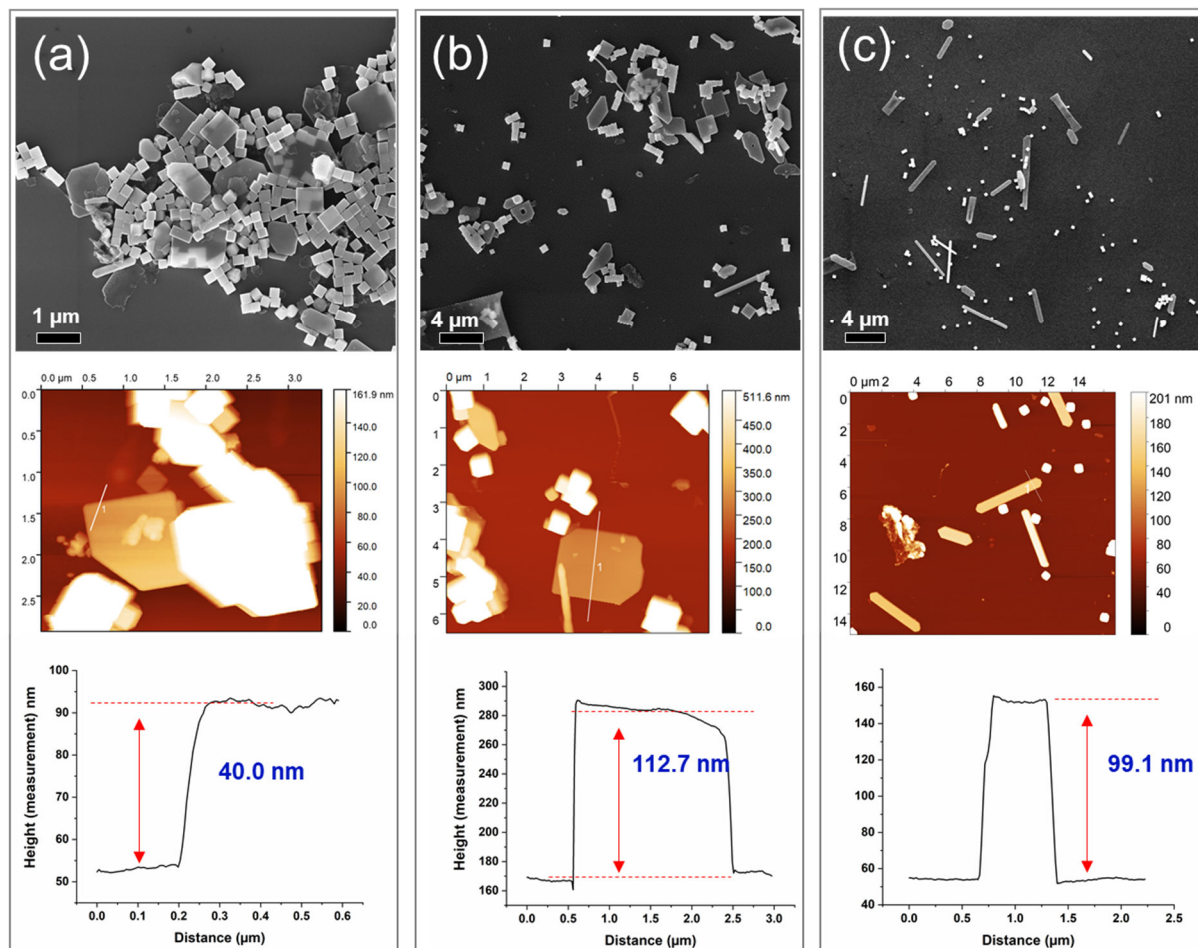
Figure 3.42. SEM image, the corresponding AFM images and the height measurements of the synthesized SnTe nanocrystals using 1-CTD as co-ligands, synthesized at specific reaction temperature (a) 170 °C, (b)220 °C, (c) 260 °C.
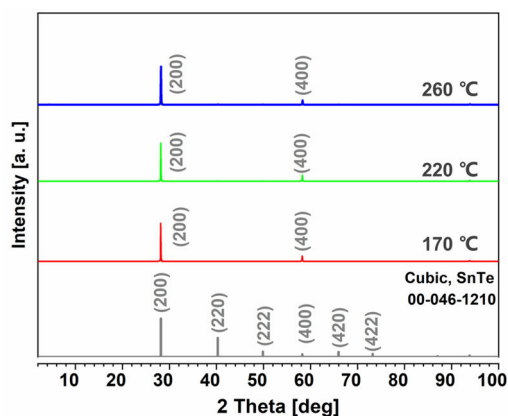
Figure 3.43. XRD diffractograms of the corresponding SnTe nanocrystals shown in Figure 3.42.

3.3.3 Other Ways to Introduce Halides

To investigate the necessity of introducing halide alkanes, we have also performed the synthesis of SnTe nanocrystals with tin halide precursors, as well as the synthesis of SnTe nanocrystals using halide salts including lithium chloride (LiCl) or lithium bromide (LiBr) to introduce halide ions.
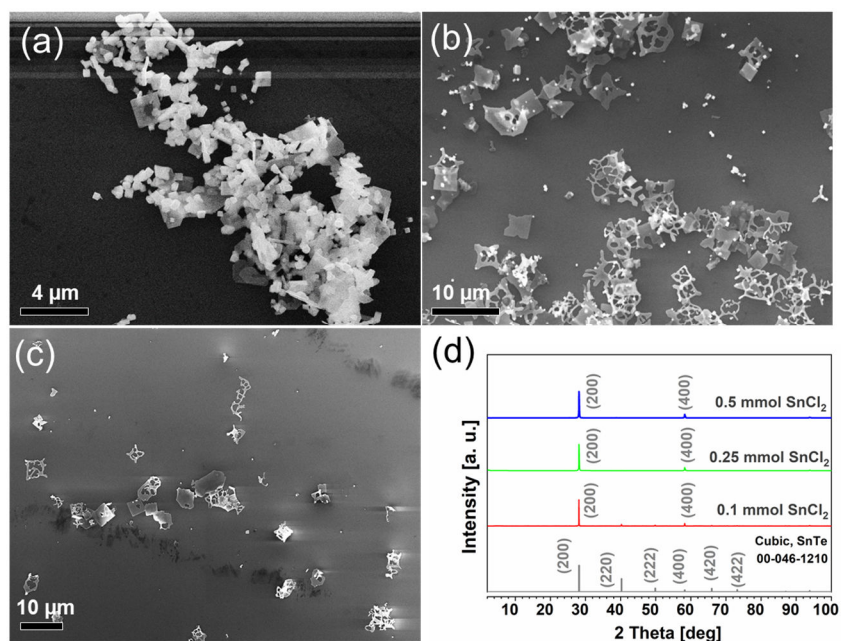
Figure 3.44. SEM images and the corresponding XRD diffractograms of the synthesized SnTe nanocrystals using no halide alkanes as co-ligands and different amounts of tin (II) chloride as a tin precursor. (a) 0.1 mmol, (b) 0.25 mmol, (c) 0.5 mmol.

When tin (II) chloride ($SnCl_2$) is used as the tin precursor instead of tin (II) acetate, more than half of the nanocrystals turn out to be etched after the synthesis, which is independent of the tin chloride amount involved in the reaction (see Figure 3.44). When a small amount of $SnCl_2$ (0.1 mmol) is used, plenty of small platelets with slightly etched and thinner inside part, as well as many cubes are formed. When the amount of $SnCl_2$ reaches 0.25 mmol, larger etched 2D nanosheets appear (see Figure 3.34b). This etching effect becomes much stronger when the $SnCl_2$ amount rises to 0.5 mmol. XRD diffractograms of these samples show increasingly pronounced (200) and (400) reflexes. Introducing tin (II) bromide ($SnBr_2$) into the synthesis to replace tin (II) acetate also results in similar products (see Figure 3.45).
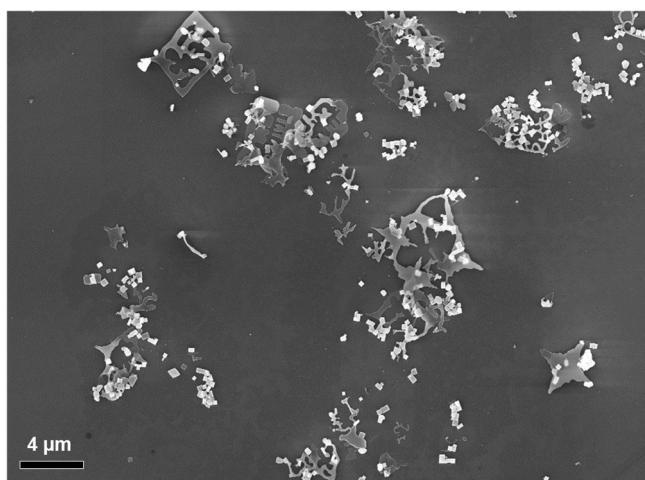
Figure 3.45. SEM image of the synthesized SnTe nanocrystals using $SnBr_2$ as the tin precursor and no halide alkanes as co-ligands for the reaction.

In terms of tin halides as precursors for the SnTe nanocrystal synthesis, tin (II) iodide (SnI_2) was used as the tin precursor for SnTe nanocube preparation along with shape evolution towards rods or even wires.[135] Nevertheless, adopting $SnCl_2$ (or $SnBr_2$) here is not appropriate since the etching problem will occur during the synthesis. Based on the standard synthesis in this thesis, it was found that acetate groups from tin (II) acetate may assist the nanocrystals to avoid etching during the synthesis. Therefore, the etching cannot be avoided if there is $SnCl_2$ serving as the tin precursor instead of tin acetate for the synthesis.

The AFM measurement on one etched nanostructure demonstrates that the height is about 76 nm (see Figure 3.46). The taking-aliquot study implies that the etching by halide ions happens

rapidly at the very beginning during the nanosheet formation, and the nanosheets grow thicker and thicker with longer reaction time based on the TEM contrast (see Figure 3.47). It can be observed that at a very early stage, there are already thin structures formed although the crystallinity at that time is not established so far, as indicated in the SAED pattern (see Figure 3.47a, inset). Then the nanosheets and etched frames which show high crystallinity appear before 1 min (see Figure 3.47b). With the extended period of the reaction time, thicker nanosheets as well as more etched structures from the nanosheets can be seen based on a much darker contrast from the TEM image (see Figure 3.47c-f).
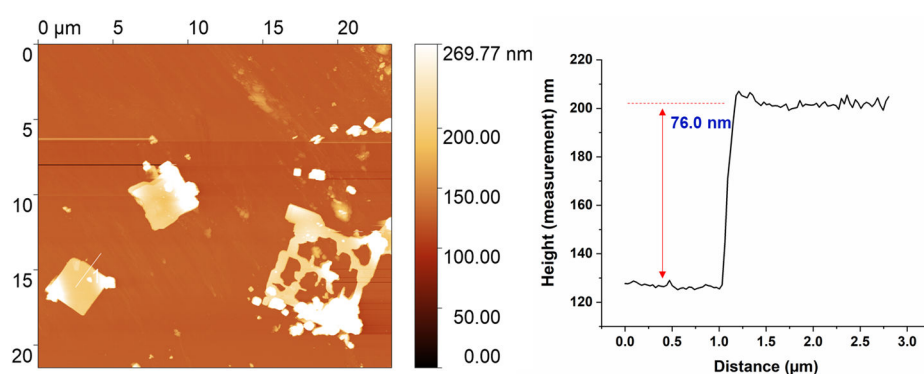
Figure 3.46. AFM image and the corresponding height line scan of the synthesized SnTe nanocrystals which are shown in Figure 3.44b.
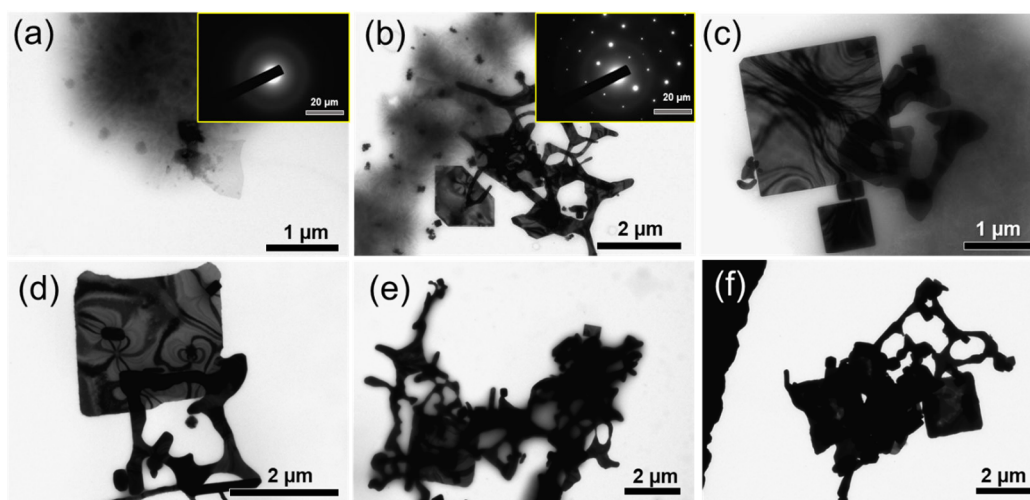
Figure 3.47. TEM images and SAED pattern of the aliquot samples taking from the reaction in Figure 3.44b during the reaction at (a) 15 s, (b) 1 min, (c) 2 min, (d) 4 min, (e) 10 min after the hot-injection of TOP-Te precursor and (f) 10 min reaction followed by cooling down and purification process.

Furthermore, LiCl or LiBr dissolved in dimethylformamide (DMF) has also been used to replace 1-BTD for introducing halides as comparison groups. From Figure 3.48, we can observe that more 2D nanostructures are formed with an increasing amount of LiCl. When there is only a small amount of LiCl involved, small rods and particles are produced in the form of agglomerates. When the amount reaches 0.2 mmol, the synthesized nanostructures are etched more strongly and the products become stickier during the washing steps (see Figure 3.48c). The products contain few nanosheets. There are also small particles or agglomerates prepared in the syntheses using LiBr instead of LiCl (see Figure 3.48d-f). These experiments indicate that direct introduction of halide ions will strongly influence the surface passivation and finally lead to large agglomerates or undefined etched structures and high polydispersity (see Figure 3.48). This also indirectly implies that the acetate group is not the key factor to avoid etching on nanocrystals, whereas the halide alkane is considered as the important parameter for obtaining non-etched 2D SnTe nanocrystals in our case.
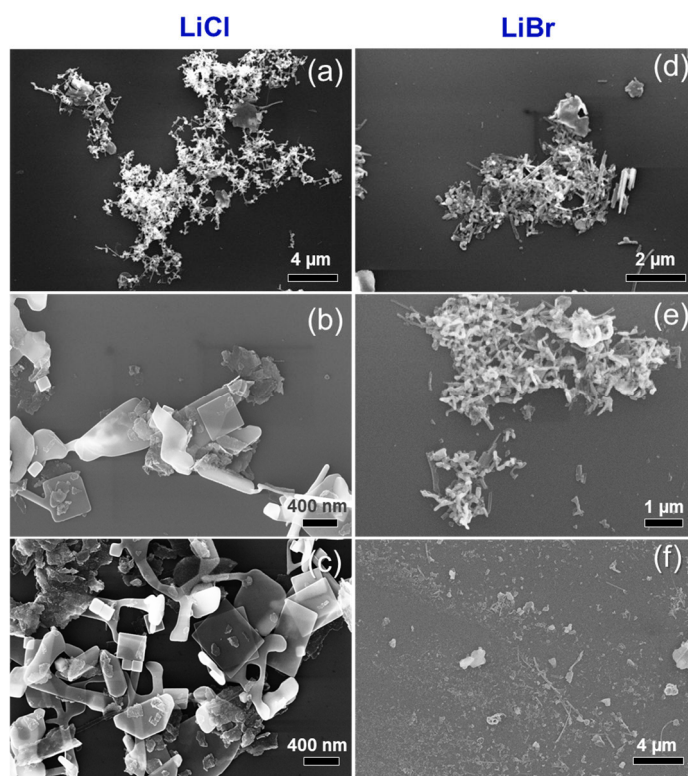
Figure 3.48. (a-c) SEM images of the synthesized SnTe nanocrystals using different amounts of LiCl dissolving in DMF: (a) 0.005 mmol LiCl, (b) 0.02 mmol LiCl, (c) 0.2 mmol LiCl. (d-f) SEM images of the synthesized SnTe nanocrystals using different amounts of LiBr dissolving in DMF: (d) 0.01 mmol LiBr, (e) 0.02 mmol LiBr, (f) 0.04 mmol LiBr.

3.3.4 Effect of Reaction Time

The influence of the reaction time has also been investigated (see Figure 3.49). The TEM images and AFM images (see Figure 3.50) display that longer time leads to a greater number of cubes and rods and fewer nanostripes. The results also exhibit less uniformity and increasing thicknesses (see Figure 3.50a, b). This phenomenon can be explained by the fact that 1-BTD can decompose to a larger extend if longer reaction time is used during the reaction, leading to similar products to the synthesis with more 1-BTD involved (see Figure 3.40d). The synthesis will be thermodynamically controlled if enough reaction time is used for the synthesis and enough activation energy to reach the minimum status of the Gibbs free energy based on the determination of thermodynamic control and kinetic control. The extended period of the reaction time can promote the formation of the product with more stability. However, the obtained products contain a high variety of structures and present less uniformity. Hence, they may be the thermodynamically favored products.
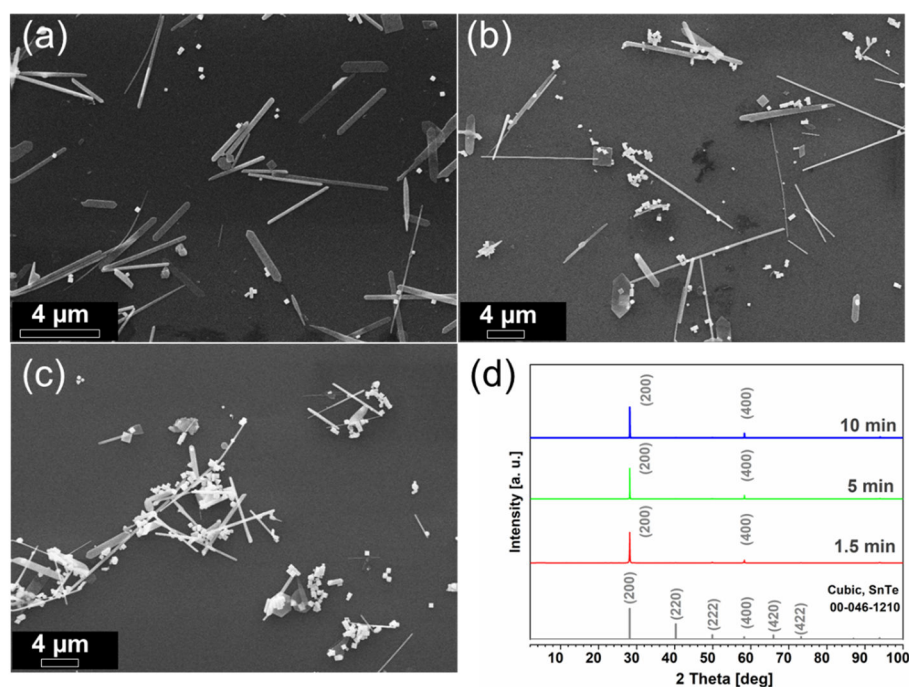
Figure 3.49. SEM images of the synthesized SnTe nanocrystals under different reaction time: (a) 1.5 min, (b) 5 min, (c) 10 min.
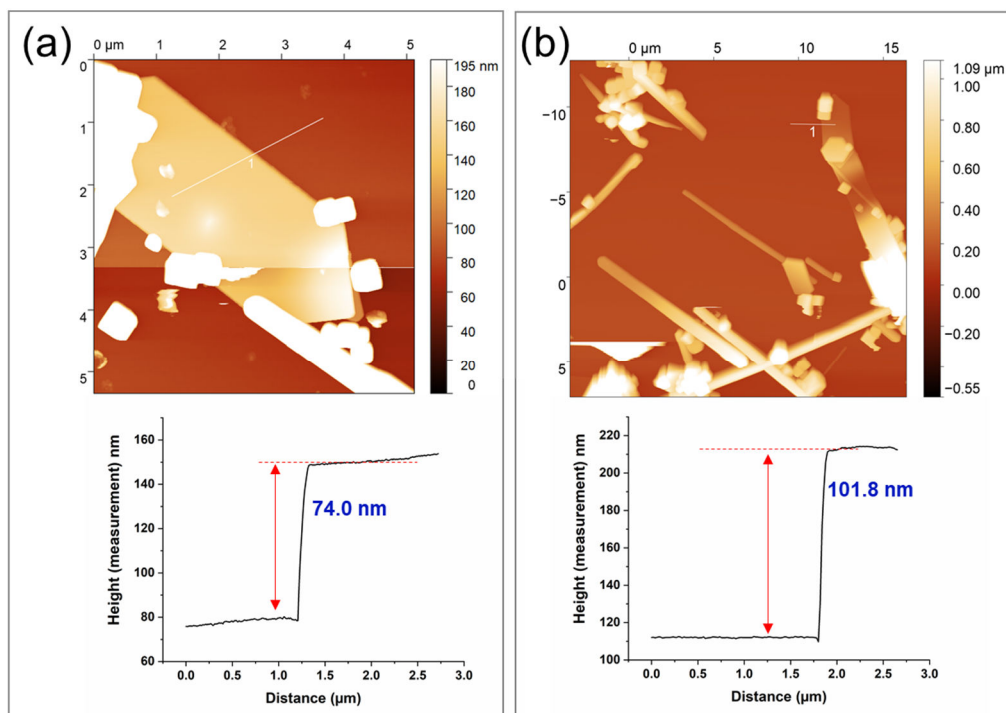
Figure 3.50. AFM images and the corresponding height line scan analysis of the synthesized SnTe nanocrystals with the reaction time of 5 min (a) and 10 min (b) compared to the standard recipe.

3.3.5 FTIR Measurements

The absorption spectra of the SnTe nanocrystals synthesized under different conditions were obtained by Fourier-transform infrared (FTIR) spectroscopy (see Figure 3.51) since the range which we are interested in lies out of the measurement range of available optical spectrometers (*e.g.* Cary 5000 with PbS detector). The nanocrystals exhibit pronounced features in the IR range, except for the ligand-related peaks at 0.35-0.36 eV (asymmetric and symmetric stretching modes of methyl (CH_3) and methylene (CH_2) groups).[164] Regarding the sample containing nanostripes synthesized with 1-BTD, there is a wide pronounced peak centered at 0.40 eV. The samples composed of nanosheets synthesized with $SnCl_2$ or 1-CTD, both show blue-shifted features, namely wide feature comprising of three strong peaks at 0.23 eV, 0.26 eV and 0.29 eV. Theoretically, the bulk bandgap of SnTe is 0.18 eV. A previous work ascribed the up-shifted features to a quantum-confined exciton transitions.[125, 159] As it is known, the first excitonic transition is below the fundamental bandgap and gives information about the optical bandgap.

We can assume that observed features within absorption curves (ii) and (iii) can be attributed to distinct populations in the ensemble. As was shown earlier, all the three typical samples are dominated with nanostructures with representative morphologies, but they still contain several other different morphologies, which leads to combined optical features with several peaks. Thus, more advanced measurements need to be applied to separate each structure such as the study of individual nanostructures for advanced IR measurements using nano-FTIR. This study is addressed to future research and will be realized, together with supportive theoretical analysis like bandgap simulations in order to individually analyze nanostripe or nanocube structures for their special optical features.
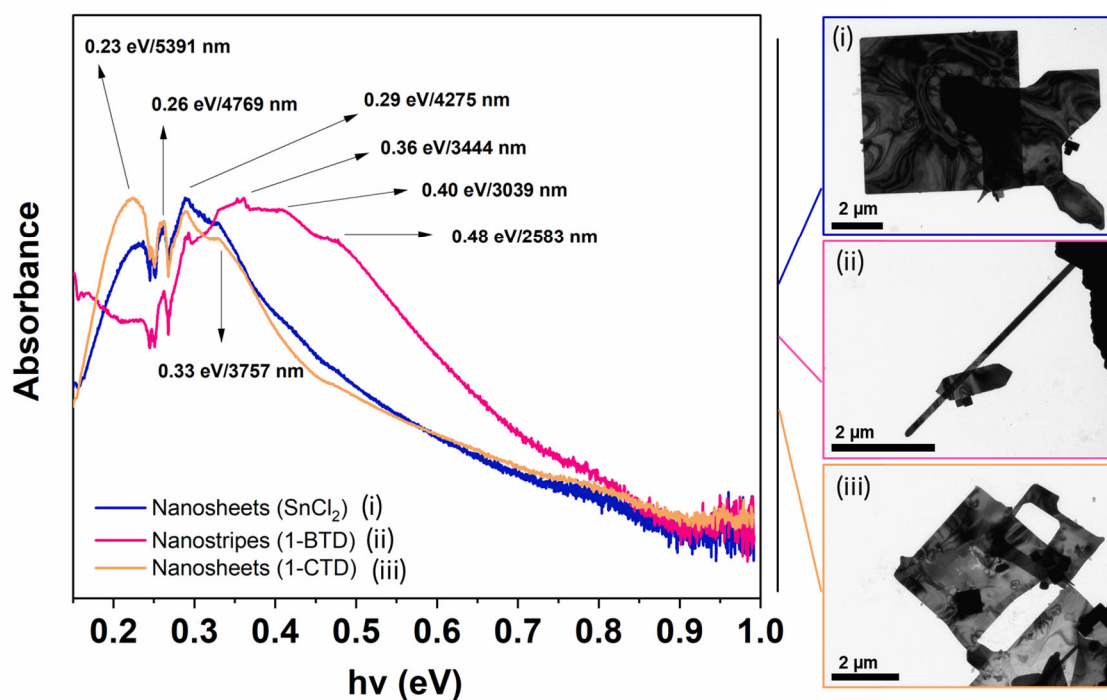
Figure 3.51. Optical absorption spectra of the synthesized different SnTe nanostructures respectively using $SnCl_2$ as the precursor (i), 1-BTD molecules as halide ligands (ii) and 1-CTD molecules as halide ligands (iii).

Chapter 4 Conclusion and Outlook

Colloidal tin (II) sulfide is emerging as a promising type of materials with a band gap similar to silicon, which is highly suitable for solar light conversion. In contrast to CdSe and PbS families, it is less toxic and possesses a layered structure with in-plane anisotropy which opens additional possibilities for property modulation. Based on the idea of facile and "green" synthesis, a stable recipe of large-sized SnS nanosheets was developed with possibilities to tune the faceting of the nanocrystals. The lateral sizes of the synthesized SnS NSs range from 150 nm to nearly 1680 nm, and the thicknesses can be tuned from 16 nm to 50 nm with the aid of oleic acid and trioctylphosphine as co-ligands in the presence of tin acetate and thioacetamide as two metal precursors. During the reaction, no metal halide such as tin chloride or flammable organo-metallic precursors is involved. Furthermore, the introduction of ligands oleic acid, trioctylphosphine, as well as dissociated oleate is the key to the shape and size tuning of the synthesized SnS nanosheets. The shape of the synthesized nanosheets varies between hexagonal shape and square-like shape with respect to the change of the ligand quantity (acetate, oleate, trioctylphosphine, oleic acid). In addition, the phase is optimized from pseudotetragonal (as presented in nanoparticle byproducts) and orthorhombic crystal structures (SnS nanosheets) to pure orthorhombic type. The measurements of conductivity and photoconductivity exhibit tremendous potential for electric and optoelectronic applications like photo-sensors and photo-switches.

With the optimization of the original recipe above, the evolution of crystal-edge orientation switching, defined as edge faceting of large and thin SnS nanosheets has also been investigated. It was found that the edge-faceting can be switched between faceting along two anisotropic directions (*i.e.* (100) and (001) facets) and along two isotropic directions (*i.e.* {101} facets). The lateral size (up to 8 μm) and thickness (down to 7 nm) for SnS nanocrystals are also highly improved. Such tunability is realized by the usage of less reactive sulfur precursor trioctylphosphine-S, TOP-S. This approach provides an opportunity to easily contact individual nanosheets on the substrate with predefined orientations, which can hence facilitate the device-level application based on the anisotropic electronic properties of SnS. In our investigations, we have evaluated the conductivities along these two directions. The results exhibit different conductivities (ratio: 1.67) for each distinct crystallographic direction, showing an in-plane

electronic anisotropy along zigzag and armchair directions, but an isotropic behavior from corner to corner, or "ladder" directions. This also validates the edge faceting in terms of morphology.

Furthermore, another tin chalcogenide nanomaterial SnTe has also been investigated. Due to the absence of established recipes for the synthesis of 2D SnTe nanostructures in literature, a novel colloidal synthesis method has been developed to obtain large 2D SnTe nanocrystals, or nanostripes. The recipe involves halide alkane 1-bromotetradecane (1-BTD) and is based on the developed recipe mentioned above for SnS nanocrystals. 2D elongated SnTe nanosheets or SnTe nanostripes are obtained with few byproducts of cubes and long nanorods as byproducts. The thickness of the synthesized SnTe nanostripes can be tuned down to 29 nm and the length can reach approximately 6.0 μm. The nanocrystals display high crystallinity as can be proved by XRD and SAED. The influence of 1-BTD used in the reaction has also been studied, uncovering that an increase in 1-BTD leads to a higher percentage of nanorods instead of 2D nanostripes, which is also seen with longer reaction time for the synthesis. For the experiments with tin chloride as the precursor, it is found that direct introduction of halide ions in tin precursors such as $SnCl_2$ or $SnBr_2$ results in strong etching effects even at the initial stage of the formation of SnTe nanocrystals. Introducing halide ions by adopting LiCl or LiBr is found not appropriate, causing not avoidable aggregation and etching as well as a low yield of 2D nanostructures. Additionally, the IR absorption spectra of SnTe with different nanostructures have been investigated, revealing pronounced excitonic absorption features in the IR range.

In conclusion, the optimization of the solution-phase recipes for tin chalcogenide nanocrystals have been studied. The anisotropic growth patterns can be obtained by modulating the ligands composition due to different binding affinities of applied ligands on the crystal surfaces. Observed effects have been supported by DFT calculations of adsorption energies of corresponding molecules on relevant crystal facets. Hence, the introduced colloidal-synthesis techniques exhibit the possibilities that tin chalcogenide nanocrystals with tunable morphologies can be prepared independent of the crystal structures (layered or non-layered). These established methods can be further optimized and extended to other metal chalcogenides to achieve more fascinating 2D metal chalcogenide nanocrystals.

The investigation of tin chalcogenides is intriguing and opens more possible researching puzzles for the future. Further work will also be done as follows: the investigation on anisotropic SnS, the further analysis for absorption features of SnTe nanostructures (for instance by nanoFTIR for individual particles), as well as absorption ab-initio simulations for SnTe to clarify the absorption spectra of individual nanostructures, and band structure peculiarities and optical transitions of a nanocrystal in 1D confinement. The further fabrication of anisotropic SnS *e.g.* field-effect transistors (FETs) can also be investigated to evaluate the intrinsic anisotropic transport properties about the strong in-plane electronic anisotropy.[123] Different from the promising prospect in broadband photodetectors for graphene, layered 2D SnS has potential in near-infrared photodetectors owing to its direct bandgap (1.3 eV) as well as high absorption coefficient (> 10^4 cm^{-1}).[165] Hence, further work on fabricating NIR light photodetectors with large 2D anisotropic SnS will also be attractive. It has also been illustrated that SnS displays remarkable anisotropy in the lattice thermal conductivity in addition to strong anisotropic electrical conductivities, based on the first-principles calculations.[124] Therefore, thermoelectric performance of synthesized SnS nanocrystals in the thesis can also be interesting for further research. First-principles calculations were also applied on SnS and SnTe by Li *et al.* to calculate the bandgaps with the effect of compressive strains and tensile strains, exhibiting excellent piezoelectric properties.[166]

Since most studies on topological insulators are conducted with crystals coming from vapor-phase-based methods (like for Bi_2Te_3), the solution-based synthesis of SnTe displays a good potential in this field due to the high degree of synthesis and final structure/surface control. As a new discovered type of materials, topological insulators have been witnessed in experiments on bulk SnTe crystals after forecasted by theory, and have been found to show improved features if the size reaches nanoscale dimensions.[167] This results from the large surface-to-volume ratio of nanocrystals, which significantly improves the contribution of surface carriers.[7, 168] Thus, the electrical transport measurements and studies of topological surface states clearly motivate the further work as well.

Additionally, there is an increasing attention for the substitution of lead by the element tin in the synthesis of metal halide perovskite nanocrystals.[169-176] Although lead-based perovskite

nanocrystals exhibits effective and tunable photoluminescence, the substitution of lead with Sn (or Ge, Bi, Sb) is still highly desirable, owing to their advantages of being environmentally benign.[177] There have been published solution-phase syntheses of tin-based perovskite nanocrystals in recent five years. For instance, Wang *et al.* also investigated Cs_2SnI_6 perovskite nanocrystals by introducing tin(IV) iodide and cesium oleate with the aid of oleic acid and oleylamine at 220 ℃.[172] The morphology of the synthesized Cs_2SnI_6 perovskite nanocrystals can be tuned between spherical quantum dots, nanorods, nanowires, nanobelts, and nanoplatelets. The fabrication of the nanocrystals into an FET device was also performed, showing a p-type semiconducting behavior. The synthesized nanocrystals are also in zero dimensions and the sizes can be manipulated to obtain tunable optical bandgaps. In addition, hybrid halide perovskite nanocrystals based on the element tin have also attracted increasing attention such as methylammonium or formamidinium involved $MASn(I, Br)_3$ or $FASn(I, Br)_3$.[176] However, the colloidal synthesis for large-sized and stable tin-based perovskite nanosheets is still elusive. Thus, this could be an interesting topic in the future, expanding the investigation on tin-based nanomaterials.

Chapter 5 Experimental Part

In this chapter, the experimental set-ups and steps will be explained in detail to show how the syntheses of low-dimensional SnS and SnTe are proceeded, and to show how the recipes are improved and optimized for further characterization and early applications.

5.1 Chemicals and Materials

5.1.1 Chemicals Needed for the Synthesis and Characterization

All the chemicals applied in the reaction and characterization were purchased from the companies including Sigma Aldrich, Merck, VWR International Co, and Thermo Fisher Scientific. All the chemicals and solvents are reagent grade or in better quality and used as received for the reaction. Thioacetamide (TAA), trioctylphosphine (TOP), tin (II) acetate (TA), sulfur and tellurium were all stored in the glovebox.

REAGENT LIST:

◆ 1-Bromotetradecane	Sigma Aldrich
◆ 1-Chlorotetradecane	Sigma Aldrich
◆ Diphenylether	Sigma Aldrich
◆ N, N-Dimethylformamide	Sigma Aldrich
◆ 2-propanol	VWR International
◆ Lithium chloride	Sigma Aldrich
◆ Oleic acid	Sigma Aldrich
◆ Sulfur	Sigma Aldrich
◆ Tellurium	Thermo Fisher Scientific
◆ Tetrachloroethane	Sigma Aldrich

- Thioacetamide   Sigma Aldrich

- Tin (II) acetate   Sigma Aldrich

- Tin (II) chloride   Thermo Fisher Scientific

- Tin (II) bromide   Sigma Aldrich

- Trioctylphosphine   Sigma Aldrich

- Toluene   Sigma Aldrich

5.1.2 Materials and Equipment

All the materials and equipments used for the experiments were purchased from the companies including B. Braun Melsungen AG, Carl Roth.

MATERIAL LIST:

- Magnetic stirrer   Carl Roth

- Standard heating hood (for 50 ml)   OMNILAB GmbH

- TEM grids   Plano GmbH

- Centrifuge tubes (50 ml)   Carl Roth

- Centrifuge tubes (1.5 ml)   Eppendorf AG

- Disposable syringes and cannulas   B. Braun Melsungen AG

- Disposable pipettes (1 ml)   Carl Roth

5.2 Experiments and Characterizations

The synthesis procedures and characterization methods for the synthesized SnS and SnTe nanocrystals will be explained in the following sections. The syntheses are based on the hot-injection colloidal method and the characterizations are mainly based on TEM, HRTEM, SEM, XRD, AFM, UV-Vis-NIR and FT-IR measurements. In addition, device preparations, transport measurements as well as DFT simulations will also be described in the following.

5.2.1 Synthesis of Two-dimensional Square-like SnS Nanosheets

5.2.1.1 Standard Synthesis Procedure

In a typical synthesis procedure, 59.2 mg (0.25 mmol) of TA, 0.2 ml (0.64 mmol) of oleic acid (OA), 0.5 ml (1.0 mmol) of TOP, and 10 ml of diphenyl ether (DPE) were mixed in a three-necked round-bottom glass flask (50 ml). The system was then stirred for dissolving all the content, followed by degassing and drying steps under vacuum condition for 2 h at 75 ℃, in order to transform the tin acetate into tin oleate complexes. This would lead to the release of free acetic acid from the system. Then the system was heated to 230 ℃ under N_2 atmosphere. After the temperature was stable at 230 ℃ (about 15 min), 19.5 mg of TAA (0.26 mmol) in 0.2 ml of DMF from the stock precursor solution of TAA/DMF, was quickly injected into the stirring system. After the reaction (5 min), the reaction solution was cooled down to room temperature by removing the heating mantle. The collected reaction solution was then centrifugated at 4000 rpm for 3 min (2-3 times) for purification in fresh toluene and collected again in new toluene.

5.2.1.2 Variation of Trioctylphosphine Amount

The experiments with the variation of TOP amount were carried out based on the standard recipe in Section 5.2.1.1. In each comparison experiment, 59.2 mg (0.25 mmol) of TA, 0.2 ml (0.64 mmol) of oleic acid (OA), 10 ml of diphenyl ether (DPE) and certain amount of TOP were mixed in a three-necked round-bottom glass flask (50 ml). The amount of TOP varies from 0 mmol, to 0.1 mmol, 0.5 mmol, 1.0 mmol, and 2.0 mmol for each experiment. Then the syntheses were performed as mentioned in Section 5.2.1.1.

5.2.1.3 Variation of Oleic Acid Amount

The experiments with the variation of OA amount were also carried out based on the standard recipe in Section 5.2.1.1. In each comparison experiment, 59.2 mg (0.25 mmol) of TA, certain amount of oleic acid (OA) 10 ml of diphenyl ether (DPE) and 0.5 ml (1.0 mmol) of TOP were mixed in a three-necked round-bottom glass flask (50 ml). The amount of OA varies from 0 mmol, to 0.32 mmol, 0.64 mmol, 3.2 mmol, and 6.4 mmol for each experiment. Then the syntheses were performed as mentioned in Section 5.2.1.1.

5.2.1.4 Variation of Precursor Amount

The experiments with the variation of tin acetate precursor (TA) amount were carried out based on the standard recipe in Section 5.2.1.1. In each comparison experiment, certain amount of TA, 0.2 ml (0.64 mmol) of oleic acid (OA), 10 ml of diphenyl ether (DPE) and 0.5 ml (1.0 mmol) of TOP were mixed in a three-necked round-bottom glass flask (50 ml). The amount of TA varies from 0.02 mmol, to 0.025 mmol, 0.05 mmol, 0.25 mmol, and 0.5 mmol for each experiment. Then the syntheses were performed as mentioned in Section 5.2.1.1.

The experiments with the variation of thioacetamide precursor (TAA) amount were also performed based on the standard recipe in Section 5.2.1.1. In each comparison experiment, 59.2 mg (0.25 mmol) of TA, 0.2 ml (0.64 mmol) of oleic acid (OA), 10 ml of diphenyl ether (DPE) and 0.5 ml (1.0 mmol) of TOP were mixed in a three-necked round-bottom glass flask (50 ml). After the system is completely mixed and the temperature was stable at 230 ℃, certain amount of TAA in 0.2 ml of DMF, was quickly injected into the stirring system. The amount of TAA varies from 0.005 mmol, to 0.01 mmol, 0.13 mmol, 0.26 mmol, and 0.52 mmol for each experiment. Then the following steps were conducted as mentioned in Section 5.2.1.1.

5.2.2 Synthesis of Two-dimensional Larger-sized Thin SnS Nanosheets

5.2.2.1 Standard Synthesis Procedure

The synthesis method for larger-sized thin SnS nanosheets is similar to that for the square-like small SnS nanosheet in Section 5.2.1, except for using the sulfur precursor TOP-S instead of TAA, and octadecene (ODE) as the solvent instead of DPE due to a higher reaction temperature. In detail, 59.2 mg (0.25 mmol) of TA, 0.2 ml (0.64 mmol) of OA, 0.5 ml (1.0 mmol) of TOP, and octadecene (ODE, 10 mL) were mixed in a three-necked round-bottom glass flask (50 ml). After completely dissolving the mixture by heating up to 180 ℃ (approximately 15 min), the system was then cooled down to 75 ℃, followed by degassing and drying process under vacuum for 2 h. Afterwards, the system was heated up again to 300 ℃ under N_2 atmosphere. Then, the rapid introduction of TOP-S precursor was proceeded by hot injection of TOP-S (1M) solution to the hot flask. After a 5-min reaction, the system was cooled down to room temperature. The collected product was purified by centrifugation at 2000 rpm for 3 min (1-2 times). The precipitate was then dispersed again in toluene for storage or further characterization.

5.2.2.2 Manipulating the Transition Between a-SnS and i-SnS Nanosheets

The variation of the TOP-S amount was studied based on the standard recipe in Section 5.2.2.1.

Under the circumstance with 1.0 mmol TOP in the flask before mixing, the system was heated up again to 300 ℃ under N_2 atmosphere. Then, the rapid hot-injection of a certain amount of TOP-S was performed. The amount of TOP-S (1M) varies from 0.26 ml to 0.52 ml, and 0.78 ml for each experiment. Then the following steps were conducted as mentioned in Section 5.2.2.1.

Under the circumstance without any TOP in the flask before mixing, the system was heated up again to 300 ℃ under N_2 atmosphere. Then, the rapid hot-injection of a certain amount of TOP-S was performed. The amount of TOP-S (1M) varies from 0.52 ml to 1.04 ml for each experiment. Then the following steps were conducted as mentioned in Section 5.2.2.1.

5.2.3 Synthesis of SnTe Nanostructures

5.2.3.1 Standard Synthesis Procedure

In a standard synthesis recipe for obtaining SnTe nanostripes, 59.2 mg (0.25 mmol) of TA, 2 ml (6.4 mmol) of OA, 0.5 ml (1.0 mmol) TOP, and 10 ml of diphenyl ether (DPE) were mixed in a three-necked round-bottom glass flask (50 ml). After completely dissolving the mixture by heating up to 130 ℃ (approximately 10 min), the system was cooled down to 75 ℃, followed by degassing and drying process under vacuum for 2 h at 75 ℃. Afterwards, the system was heated up to 250 ℃ under N_2 atmosphere after injecting 0.19 ml (0.64 mmol) 1-bromotetradecane (1-BTD) at 75 ℃. Then, the rapid introduction of TOP-Te precursor was proceeded by the hot-injection of TOP-Te (1M) solution to the hot flask. The system was then cooled down to the room temperature after the reaction solution had a color change to greyish-yellow. The collected product was purified by centrifugation at 4000 rpm for 3-4 min. The precipitate was then dispersed again in toluene for storage or further characterization.

5.2.3.2 Variation of 1-BTD Halide Alkanes

The experiments with the variation of 1-BTD amount were performed based on the standard recipe in Section 5.2.3.1. In each comparison experiment, the system was heated up to 250 ℃ under N_2 atmosphere after injecting certain amount of 1-bromotetradecane (1-BTD) at 75 ℃. Then the rapid introduction of TOP-Te precursor was proceeded by the hot-injection. The amount of 1-BTD varies from 0.17 mmol, to 0.34 mmol, 0.64 mmol, and 0.96 mmol for each experiment. Then the syntheses were conducted as mentioned in Section 5.2.3.1.

Additionally, 1-CTD was also used to replace 1-BTD to observe the effect on the reaction. The amount of 1-CTD was 0.64 mmol and the reaction temperature varies from 250 ℃ to 220 ℃ and 260 ℃. Then the syntheses were conducted as mentioned in Section 5.2.3.1.

5.2.3.3 Involving Halide Salt Precursors

The experiments with the variation of tin (II) chloride amount were performed based on the standard recipe in Section 5.2.3.1. The tin (II) chloride halide salts were used to replace tin (II) acetate precursors. The amount of tin (II) chloride varies from 0.1 mmol, to 0.25 mmol, and 0.5 mmol. Then the syntheses were conducted as mentioned in Section 5.2.3.1.

Additionally, tin (II) bromide was also used to replace tin (II) acetate with the amount of 0.25 mmol. Then the syntheses were conducted as mentioned in Section 5.2.3.1.

5.2.3.4 Involving Halide Salt Surfactants

The experiments with the variation of LiCl amount were performed based on the standard recipe in Section 5.2.3.1. The amount of LiCl varies from 0.005 mmol, to 0.02 mmol, and 0.2 mmol. Then the syntheses were conducted as mentioned in Section 5.2.3.1.

Additionally, LiBr was also studied to replace LiBr and the amount varies from 0.01 mmol, to 0.02 mmol, and 0.04 mmol. Then the syntheses were conducted as mentioned in Section 5.2.3.1.

5.2.3.5 Adjusting the Reaction Time

The experiments with the variation of reaction time were performed based on the standard recipe in Section 5.2.3.1. The reaction time varies from 1.5 min, to 5 min, and 10 min.

5.2.4 Device Preparation and Transport Measurement

Diluted SnS nanosheet suspension was dropped on the Si substrate (fabricated with a 300 nm thermal silicon oxide layer as the gate dielectric) by spin-coating procedure with optimized speed and spin time. The highly doped silicon was applied here as the back gate. The selected single SnS NS was contacted by e-beam lithography, and the thermal evaporation of Ti/Au (1/55 nm) and lift-off were carried on for the measurements.

The contacted sample prepared after device fabrication was immediately transferred to a probe station (Lakeshore Desert), which was connected to a semiconductor parameter analyzer (Agilent B1500a). All the measurements were conducted under vacuum at room temperature. The sample illumination could be realized through the view port of the vacuum chamber. For NS illumination, a red laser (627 nm, 1-16 mW) with a spot size of 2 mm was utilized.

The device preparation and transport measurements for anisotropic SnS nansheets were also performed similarly as mentioned above. Individual sheets were picked to be contacted and measured at room temperature. In one group, four contacts were placed parallel to the side edges, to get the conductivity value along the anisotropic directions. For another group of devices, the contacts were placed from corner to corner, to investigate the isotropic directions.

5.2.5 Material Characterizations

The material characterizations were performed using TEM, HRTEM, SEM, XRD, AFM, UV-Vis-NIR spectrophotometer and FTIR for obtaining morphology information, crystal structure, and thickness.

In detail, TEM images and SAED patterns were taken using a JEOL-1011 (100 kV). The TEM samples were prepared via dropping diluted sample solution on carbon-covered TEM grids. HRTEM images and corresponding SAED patterns were acquired using a Philips CM300 UT microscope (200 kV). The HRTEM samples were also prepared via dropping diluted sample solution on carbon-covered TEM grids.

The XRD patterns were obtained from the measurement by a Philips X'Pert System in Bragg– Brentano geometry equipped with a Cu anode at 0.154 nm of X-ray wavelength. XRD samples were prepared by drop-casting of well-dispersed nanocrystal solution on the silicon wafer.

The height information or thickness data were measured by an AFM device (JPK, Bruker) via intermittent-contact mode (tapping mode). The AFM samples were prepared by dropping a diluted sample solution on a Si substrate.

SEM characterizations were conducted to acquire the surface morphology and shape distribution.

The SEM samples were also prepared by dropping a diluted sample solution on a Si substrate. The secondary electron (SE) mode was used for imaging, which can give better information about the surface morphology of 2D nanostructures.

UV-Vis-NIR absorption spectra were recorded on a Cary 5000 spectrophotometer (Varian, Agilent Technologies) with an integrated sphere in a range between 300 and 1500 nm. The purified samples were finally dispersed in tetrachloroethane (TCE) which was also used as background source during UV measurement.

FTIR measurements were carried out by drying the nanocrystals and putting the powders on a diamond-ATR unit. The FTIR measurements are performed with a range from 400 to 8000 cm^{-1}.

5.2.6 DFT Simulations

Owing to the requirement for evaluating the adsorption energies of each type of ligand on different crystal facets, simulations relying on density functional theory (DFT) were carried on. For making the adsorption abilities of all tested ligands comparable, ligands were set free to relax by geometry optimization, with the condition that the crystal geometry was kept fixed to experimental values for OR-SnS.

We employed the DZVP basis set from the CP2K software package, together with a GTH-PADE potential.[178] In terms of the model, an individual built SnS nanocrystal with 224 Sn and 224 S atoms, and respective ligands molecules were simulated. The simulations were all conducted under periodic boundary conditions. The box dimensions are adequately large, in order to shun the interactions between the neighboring virtual molecular structures.

Chapter 6 Appendix

Chemicals and Additional Data

Appendix A List of Hazardous Substances

Table A1: Described GHS information sheet of hazardous substances applied in this thesis.[179-180]

Chemical Name	Pictogram Symbol	Hazard Statement	Precautionary Statement
1-Bromotetradecane	⚠	H315-H319	P264-P280
1-Chlorotetradecane	Not a hazardous substance or mixture according to Regulation (EC) No. 1272/2008.		
Diphenylether	⚠ 🌍	H319-H411	P273-P305+P351+P338
N, N-Dimethylformamide	🔥 ☣ ⚠	H226-H312-H332-H319-H360D	P201-P210-P302+P352-P304+P340-P305+P351+P338-P308+P313
2-propanol	🔥 ⚠	H225-H319-H336	P210-P233-P240-P305+P351+P338-P403+P235
Lithium chloride	⚠	H302-H315-H319	P301+P312+P330-P305+P351+P338
Oleic acid	Not a dangerous substance according to GHS.		
Sulfur	⚠	H315	P280-P302+P352-P332+P313-P362+P364
Tellurium	☣ ⚠	H332-H317-H360-H412	P201-P261-P280-P380+P313

Chemical Name	Pictogram Symbol	Hazard Statement	Precautionary Statement
Tetrachloroethane		H310-H330-H411	P260-P273-P280-P302+P352-P304+P340-P308+P310
Thioacetamide		H350-H302-H315-H319-H412	P201-P273-P308+P313-P305+P351+P338-P302+P352
Tin (II) acetate		H302-H312-H332	P280
Tin (II) chloride		H332-H314-H317-H341-H361-H335-H373-H410	P260-P280-P303+P361+P353-P304+P340+P310-P305+P351+P338
Tin (II) bromide		H314	None
Trioctylphosphine		H314	None
Toluene		H225-H304-H315-H336-H361d-H373	P210-P240-P301+P310+P330-P302+P352-P314-P403+P233

Appendix B Phrases of GHS hazard statements[181]

B1. Physical hazards

H225	Highly flammable liquid and vapour
H226	Flammable liquid and vapour

B2. Health hazards

H302	Harmful if swallowed
H304	May be fatal if swallowed and enters airways
H310	Fatal in contact with skin
H312	Harmful in contact with skin
H314	Causes severe skin burns and eye damage
H315	Causes skin irritation
H317	May cause an allergic skin reaction
H319	Causes serious eye irritation
H330	Fatal if inhaled
H332	Harmful if inhaled
H335	May cause respiratory irritation
H336	May cause drowsiness or dizziness
H341	Suspected of causing genetic defects
H350	May cause cancer
H360	May damage fertility or the unborn child
H361d	Suspected of damaging the unborn child
H361	Suspected of damaging fertility or the unborn child
H373	May cause damage to organs through prolonged or repeated exposure

B3. Environmental hazards

H410	Very toxic to aquatic life with long-lasting effects
H411	Toxic to aquatic life with long-lasting effects
H412	Harmful to aquatic life with long-lasting effects

Appendix C Phrases of GHS precautionary statements

C1. Prevention precautionary statements

P201	Obtain special instructions before use
P210	Keep away from heat, hot surfaces, sparks, open flames, and other ignition sources. No smoking
P233	Keep container tightly closed
P240	Ground/bond container and receiving equipment
P260	Do not breathe dust/fumes/gas/mist/vapours/spray
P261	Avoid breathing dust/fumes/gas/mist/vapours/spray
P264	Wash … thoroughly after handling
P273	Avoid release to the environment
P280	Wear protective gloves/protective clothing/eye protection/face protection

C2. Response precautionary statements

P314	Get medical advice/attention if you feel unwell
P301+330+331	IF SWALLOWED: Rinse mouth. Do NOT induce vomiting
P301+312	IF SWALLOWED: Call a POISON CENTER/doctor/…/if you feel unwell
P302+352	IF ON SKIN: Wash with plenty of water/…
P303+361+353	IF ON SKIN (or hair): Take off immediately all contaminated clothing. Rinse skin with

	water/ shower
P304+340	IF INHALED: Remove person to fresh air and keep comfortable for breathing
P305+351+338	IF IN EYES: Rinse cautiously with water for several minutes. Remove contact lenses if present and easy to do – continue rinsing
P308+313	If exposed: Call a POISON CENTER or doctor/physician
P332+313	If skin irritation occurs: Get medical advice/attention
P362+364	Take off contaminated clothing and wash them before reuse

C3. Storage precautionary statements

P403+233	Store in a well-ventilated place. Keep container tightly closed
P403+235	Store in a well-ventilated place. Keep cool

Appendix D hazard pictograms

GHS02   GHS05   GHS06   GHS07

GHS08   GHS09

D1. GHS hazard pictograms phrases:

GHS02: Flammable

GHS05: Corrosive

GHS06: Toxic

GHS07: Harmful

GHS08: Health hazard

GHS09: Environmental hazard

Chapter 7 Bibliography

1.   Wood, A. J. Fabrication and characterization of a plasmonic grating platform for enhanced fluorescence biosensor applications. University of Missouri--Columbia, 2016.

2.   Lv, R.; Robinson, J. A.; Schaak, R. E.; Sun, D.; Sun, Y.; Mallouk, T. E.; Terrones, M., Transition metal dichalcogenides and beyond: synthesis, properties, and applications of single-and few-layer nanosheets. *Accounts of chemical research* **2014,** *48* (1), 56-64.

3.   Koh, W.-k.; Dandu, N. K.; Fidler, A. F.; Klimov, V. I.; Pietryga, J. M.; Kilina, S. V., Thickness-Controlled Quasi-Two-Dimensional Colloidal PbSe Nanoplatelets. *Journal of the American Chemical Society* **2017,** *139* (6), 2152-2155.

4.   Thanh, N. T. K.; Maclean, N.; Mahiddine, S., Mechanisms of nucleation and growth of nanoparticles in solution. *Chemical Reviews* **2014,** *114* (15), 7610-7630.

5.   Valiev, R., Nanomaterial advantage. *Nature* **2002,** *419*, 887-889.

6.   Chen, Y. P.; Yu, Q., Nanomaterials: Graphene rolls off the press. *Nature Nanotechnology* **2010,** *5* (8), 559-560.

7.   Safdar, M.; Wang, Q.; Mirza, M.; Wang, Z.; Xu, K.; He, J., Topological surface transport properties of single-crystalline SnTe nanowire. *Nano letters* **2013,** *13* (11), 5344-5349.

8.   Hsieh, T. H.; Lin, H.; Liu, J.; Duan, W.; Bansil, A.; Fu, L., Topological crystalline insulators in the SnTe material class. *Nature communications* **2012,** *3*, 982.

9.   Tanaka, Y.; Ren, Z.; Sato, T.; Nakayama, K.; Souma, S.; Takahashi, T.; Segawa, K.; Ando, Y., Experimental realization of a topological crystalline insulator in SnTe. *Nat Phys* **2012,** *8* (11), 800.

10.   Shen, J.; Jung, Y.; Disa, A. S.; Walker, F. J.; Ahn, C. H.; Cha, J. J., Synthesis of SnTe nanoplates with {100} and {111} surfaces. *Nano letters* **2014,** *14* (7), 4183-4188.

11.   Li, Z.; Shao, S.; Li, N.; McCall, K.; Wang, J.; Zhang, S., Single crystalline nanostructures of topological crystalline insulator SnTe with distinct facets and morphologies. *Nano letters* **2013,** *13* (11), 5443-5448.

12.   Dobson, J., Gene therapy progress and prospects: Magnetic nanoparticle-based gene delivery. *Gene Therapy* **2006,** *13* (4), 283-287.

13.   Schmid, G., Nanoparticles: from theory to application. Wiley-VCH 2004.

14.   Dang, S.; Zhu, Q. L.; Xu, Q., Nanomaterials derived from metal-organic frameworks. *Nature Reviews Materials* **2017,** *3*, 17075-17075.

15.   Niemann, M. U.; Srinivasan, S. S.; Phani, A. R.; Kumar, A.; Goswami, D. Y.; Stefanakos, E. K.,

Nanomaterials for hydrogen storage applications: A review. *Journal of Nanomaterials* **2008,** *2008* (1).

16. Fahlman, B. D., What Is "Materials Chemistry"? In *Materials chemistry*, Springer: 2018; pp 282-283.

17. Yin, Y.; Alivisatos, A. P., Colloidal nanocrystal synthesis and the organic–inorganic interface. *Nature* **2004,** *437* (7059), 664.

18. Erdemir, D.; Lee, A. Y.; Myerson, A. S., Nucleation of crystals from solution: classical and two-step models. *Accounts of chemical research* **2009,** *42* (5), 621-629.

19. Polte, J., Fundamental growth principles of colloidal metal nanoparticles–a new perspective. *CrystEngComm* **2015,** *17* (36), 6809-6830.

20. Lamer, V. K.; Dinegar, R. H., Theory, Production and Mechanism of Formation of Monodispersed Hydrosols. *Journal of the American Chemical Society* **1950,** *72* (11), 4847-4854.

21. Watzky, M. A.; Finke, R. G., Transition metal nanocluster formation kinetic and mechanistic studies. A new mechanism when hydrogen is the reductant: slow, continuous nucleation and fast autocatalytic surface growth. *Journal of the American Chemical Society* **1997,** *119* (43), 10382-10400.

22. Peng, X.; Manna, L.; Yang, W.; Wickham, J.; Scher, E.; Kadavanich, a.; Alivisatos, A., Shape control of CdSe nanocrystals. *Nature* **2000,** *404* (6773), 59-61.

23. Cho, K. S.; Talapin, D. V.; Gaschler, W.; Murray, C. B., Designing PbSe nanowires and nanorings through oriented attachment of nanoparticles. *Journal of the American Chemical Society* **2005,** *127*, 7140-7147.

24. Schliehe, C.; Juarez, B. H.; Pelletier, M.; Jander, S.; Greshnykh, D.; Nagel, M.; Meyer, A.; Foerster, S.; Kornowski, A.; Klinke, C.; Weller, H., Ultrathin PbS Sheets by Two-Dimensional Oriented Attachment. *Science* **2010,** *329* (5991), 550-553.

25. Becker, R.; Döring, W., Kinetische behandlung der keimbildung in übersättigten dämpfen. *Annalen der Physik* **1935,** *416* (8), 719-752.

26. Mullin, J., In Crystallization; Mullin, JW, Ed. Butterworth-Heinemann: Boston: 1997.

27. Sugimoto, T., *Monodispersed particles*. Elsevier: 2001.

28. Scopigno, T.; Yannopoulos, S. N.; Scarponi, F.; Andrikopoulos, K. S.; Fioretto, D.; Ruocco, G., Origin of the λ transition in liquid sulfur. *Physical Review Letters* **2007,** *99* (2), 1-4.

29. Peng, X.; Wickham, J.; Alivisatos, A., Kinetics of II-VI and III-V colloidal semiconductor nanocrystal growth:"focusing" of size distributions. *Journal of the American Chemical Society* **1998,** *120* (21), 5343-5344.

30. Ostwald, W., Studien über die Bildung und Umwandlung fester Körper 1897 Vol. 22, pp 289-330.

31. Peter, W. V., The Theory of Ostwald Ripening. *Journal of Statistical Physics* **1985,** *38* (1-2), 231-252.

32. Prasad, B. L. V.; Stoeva, S. I.; Sorensen, C. M.; Klabunde, K. J., Digestive-Ripening Agents for Gold Nanoparticles : Alternatives to Thiols. **2003,** *15* (4), 935-942.

33. Sidhaye, D. S.; Prasad, B. L. V., Many manifestations of digestive ripening: Monodispersity, superlattices and nanomachining. *New Journal of Chemistry* **2011,** *35* (4), 755-763.

34. Wang, F.; Richards, V. N.; Shields, S. P.; Buhro, W. E., Kinetics and Mechanisms of Aggregative Nanocrystal Growth. **2014,** *26*, 5-21.

35. Dahmen, U.; Alivisatos, A. P., Observation of Single Colloidal Platinum Nanocrystal Growth Trajectories. **2009,** *324* (June), 1309-1313.

36. Yuk, J. M.; Park, J.; Ercius, P.; Kim, K.; Hellebusch, D. J.; Crommie, M. F.; Lee, J. Y.; Zettl, A.; Alivisatos, A. P., High-Resolution EM of Colloidal Nanocrystal Growth Using Graphene Liquid Cells. *Science.* **2012,** *336* (April), 61-65.

37. Perala, S. R. K.; Kumar, S., On the two-step mechanism for synthesis of transition-metal nanoparticles. *Langmuir* **2014,** *30* (42), 12703-12711.

38. Penn, R. L.; Banfield, J. F., Imperfect oriented attachment: dislocation generation in defect-free nanocrystals. *Science* **1998,** *281* (5379), 969-971.

39. Nasilowski, M.; Mahler, B.; Lhuillier, E.; Ithurria, S.; Dubertret, B., Two-dimensional colloidal nanocrystals. *Chemical Reviews* **2016,** *116* (18), 10934-10982.

40. Zhang Q; Liu S J; H, Y. S., Recent advances in oriented attachment growth and synthesis of functional materials: concept, evidence, mechanism, and future. **2009,** *19* (2), 191-207.

41. Zhao, L.; Ji, X.; Sun, X.; Li, J.; Yang, W.; Peng, X., Formation and stability of gold nanoflowers by the seeding approach: the effect of intraparticle ripening. *The Journal of Physical Chemistry C* **2009,** *113* (38), 16645-16651.

42. Wulff, G., Xxv. zur frage der geschwindigkeit des wachsthums und der auflösung der

krystallflächen. *Zeitschrift für Kristallographie-Crystalline Materials* **1901,** *34* (1-6), 449-530.

43. Son, J. S.; Park, K.; Kwon, S. G.; Yang, J.; Choi, M. K.; Kim, J.; Yu, J. H.; Joo, J.; Hyeon, T., Dimension-controlled synthesis of CdS nanocrystals: from 0D quantum dots to 2D nanoplates. *Small* **2012,** *8* (15), 2394-402.

44. Huang, X.; Zeng, Z.; Zhang, H., Metal dichalcogenide nanosheets: preparation, properties and applications. *Chemical Society Reviews* **2013,** *42* (5), 1934-1946.

45. Chimene, D.; Alge, D. L.; Gaharwar, A. K., Two-dimensional nanomaterials for biomedical applications: emerging trends and future prospects. *Advanced materials* **2015,** *27* (45), 7261-7284.

46. Zhao, M.; Wang, Y.; Ma, Q.; Huang, Y.; Zhang, X.; Ping, J.; Zhang, Z.; Lu, Q.; Yu, Y.; Xu, H., Ultrathin 2D metal–organic framework nanosheets. *Advanced Materials* **2015,** *27* (45), 7372-7378.

47. Coleman, J. N.; Lotya, M.; O'Neill, A.; Bergin, S. D.; King, P. J.; Khan, U.; Young, K.; Gaucher, A.; De, S.; Smith, R. J., Two-dimensional nanosheets produced by liquid exfoliation of layered materials. *Science* **2011,** *331* (6017), 568-571.

48. Chhowalla, M.; Shin, H. S.; Eda, G.; Li, L.-J.; Loh, K. P.; Zhang, H., The chemistry of two-dimensional layered transition metal dichalcogenide nanosheets. *Nature chemistry* **2013,** *5* (4), 263.

49. Zhang, H., Ultrathin two-dimensional nanomaterials. *ACS nano* **2015,** *9* (10), 9451-9469.

50. Xu, M.; Liang, T.; Shi, M.; Chen, H., Graphene-like two-dimensional materials. *Chemical reviews* **2013,** *113* (5), 3766-3798.

51. Lee, Y. H.; Zhang, X. Q.; Zhang, W.; Chang, M. T.; Lin, C. T.; Chang, K. D.; Yu, Y. C.; Wang, J. T. W.; Chang, C. S.; Li, L. J., Synthesis of large-area MoS2 atomic layers with chemical vapor deposition. *Advanced materials* **2012,** *24* (17), 2320-2325.

52. Garcia, J. M.; Wurstbauer, U.; Levy, A.; Pfeiffer, L. N.; Pinczuk, A.; Plaut, A. S.; Wang, L.; Dean, C. R.; Buizza, R.; Van Der Zande, A. M., Graphene growth on h-BN by molecular beam epitaxy. *Solid State Communications* **2012,** *152* (12), 975-978.

53. Li, H.; Lu, G.; Wang, Y.; Yin, Z.; Cong, C.; He, Q.; Wang, L.; Ding, F.; Yu, T.; Zhang, H., Mechanical Exfoliation and Characterization of Single-and Few-Layer Nanosheets of WSe_2, TaS_2, and $TaSe_2$. *Small* **2013,** *9* (11), 1974-1981.

54. Kajiyama, S.; Szabova, L.; Sodeyama, K.; Iinuma, H.; Morita, R.; Gotoh, K.; Tateyama, Y.; Okubo, M.; Yamada, A., Sodium-ion intercalation mechanism in MXene nanosheets. *ACS nano* **2016,** *10*

(3), 3334-3341.

55.   Lee, K.; Kim, H. Y.; Lotya, M.; Coleman, J. N.; Kim, G. T.; Duesberg, G. S., Electrical characteristics of molybdenum disulfide flakes produced by liquid exfoliation. *Advanced materials* **2011,** *23* (36), 4178-4182.

56.   Alhabeb, M.; Maleski, K.; Mathis, T. S.; Sarycheva, A.; Hatter, C. B.; Uzun, S.; Levitt, A.; Gogotsi, Y., Selective etching of silicon from Ti_3SiC_2 (MAX) to obtain 2D titanium carbide (MXene). *Angewandte Chemie* **2018,** *130* (19), 5542-5546.

57.   Reina, A.; Jia, X.; Ho, J.; Nezich, D.; Son, H.; Bulovic, V.; Dresselhaus, M. S.; Kong, J., Large area, few-layer graphene films on arbitrary substrates by chemical vapor deposition. *Nano letters* **2008,** *9* (1), 30-35.

58.   Eigler, S.; Enzelberger-Heim, M.; Grimm, S.; Hofmann, P.; Kroener, W.; Geworski, A.; Dotzer, C.; Röckert, M.; Xiao, J.; Papp, C., Wet chemical synthesis of graphene. *Advanced materials* **2013,** *25* (26), 3583-3587.

59.   Li, H.; Wu, J.; Yin, Z.; Zhang, H., Preparation and applications of mechanically exfoliated single-layer and multilayer MoS_2 and WSe_2 nanosheets. *Accounts of chemical research* **2014,** *47* (4), 1067-1075.

60.   Geim, A. K., Graphene: status and prospects. *science* **2009,** *324* (5934), 1530-1534.

61.   Nicolosi, V.; Chhowalla, M.; Kanatzidis, M. G.; Strano, M. S.; Coleman, J. N., Liquid exfoliation of layered materials. *Science* **2013,** *340* (6139), 1226419.

62.   Dreyer, D. R.; Park, S.; Bielawski, C. W.; Ruoff, R. S., The chemistry of graphene oxide. *Chemical society reviews* **2010,** *39* (1), 228-240.

63.   Sun, J.; Lee, H.-W.; Pasta, M.; Yuan, H.; Zheng, G.; Sun, Y.; Li, Y.; Cui, Y., A phosphorene–graphene hybrid material as a high-capacity anode for sodium-ion batteries. *Nature nanotechnology* **2015,** *10* (11), 980.

64.   Zheng, J.; Zhang, H.; Dong, S.; Liu, Y.; Nai, C. T.; Shin, H. S.; Jeong, H. Y.; Liu, B.; Loh, K. P., High yield exfoliation of two-dimensional chalcogenides using sodium naphthalenide. *Nature communications* **2014,** *5*, 2995.

65.   Wang, X.; Gong, Y.; Shi, G.; Chow, W. L.; Keyshar, K.; Ye, G.; Vajtai, R.; Lou, J.; Liu, Z.; Ringe, E., Chemical vapor deposition growth of crystalline monolayer $MoSe_2$. *ACS nano* **2014,** *8* (5), 5125-5131.

66. Han, J. H.; Lee, S.; Cheon, J., Synthesis and structural transformations of colloidal 2D layered metal chalcogenide nanocrystals. *Chemical Society Reviews* **2013,** *42* (7), 2581-2591.

67. Huang, K.-J.; Zhang, J.-Z.; Shi, G.-W.; Liu, Y.-M., Hydrothermal synthesis of molybdenum disulfide nanosheets as supercapacitors electrode material. *Electrochimica Acta* **2014,** *132*, 397-403.

68. Biswas, S.; Kar, S.; Chaudhuri, S., Thioglycolic acid (TGA) assisted hydrothermal synthesis of SnS nanorods and nanosheets. *Applied Surface Science* **2007,** *253* (23), 9259-9266.

69. Muralikrishna, S.; Manjunath, K.; Samrat, D.; Reddy, V.; Ramakrishnappa, T.; Nagaraju, D. H., Hydrothermal synthesis of 2D MoS_2 nanosheets for electrocatalytic hydrogen evolution reaction. *RSC Advances* **2015,** *5* (109), 89389-89396.

70. Zhang, Y.; Hu, L.; Zhu, T.; Xie, J.; Zhao, X., High yield Bi_2Te_3 single crystal nanosheets with uniform morphology via a solvothermal synthesis. *Crystal growth & design* **2013,** *13* (2), 645-651.

71. Vattikuti, S. P.; Byon, C.; Reddy, C. V.; Venkatesh, B.; Shim, J., Synthesis and structural characterization of MoS_2 nanospheres and nanosheets using solvothermal method. *Journal of Materials Science* **2015,** *50* (14), 5024-5038.

72. Qing-Sheng, W.; Guo-Xin, Z.; Ya-Ping, D., Soft-template synthesis and optical Properties of Sb_2S_3 semiconductor quasi-nanospheres. *Journal of Nanoparticle Research* **2006,** *8* (5), 737-742.

73. Liu, Y.; Goebl, J.; Yin, Y., Templated synthesis of nanostructured materials. *Chemical Society Reviews* **2013,** *42* (7), 2610-2653.

74. Kumar, S.; Nann, T., Shape control of II–VI semiconductor nanomaterials. *Small* **2006,** *2* (3), 316-329.

75. Purkayastha, A.; Yan, Q.; Raghuveer, M. S.; Gandhi, D. D.; Li, H.; Liu, Z. W.; Ramanujan, R. V.; Borca-Tasciuc, T.; Ramanath, G., Surfactant-Directed Synthesis of Branched Bismuth Telluride/Sulfide Core/Shell Nanorods. *Advanced Materials* **2008,** *20* (14), 2679-2683.

76. Lauth, J.; Gorris, F. E.; Samadi Khoshkhoo, M.; Chassé, T.; Friedrich, W.; Lebedeva, V.; Meyer, A.; Klinke, C.; Kornowski, A.; Scheele, M., Solution-processed two-dimensional ultrathin InSe nanosheets. *Chemistry of Materials* **2016,** *28* (6), 1728-1736.

77. Son, J. S.; Wen, X. D.; Joo, J.; Chae, J.; Baek, S. i.; Park, K.; Kim, J. H.; An, K.; Yu, J. H.; Kwon, S. G., Large-Scale Soft Colloidal Template Synthesis of 1.4 nm Thick CdSe Nanosheets. *Angewandte Chemie International Edition* **2009,** *48* (37), 6861-6864.

78. Owen, J., The coordination chemistry of nanocrystal surfaces. *Science* **2015,** *347* (6222), 615-616.

79. De Roo, J.; Justo, Y.; De Keukeleere, K.; Van den Broeck, F.; Martins, J. C.; Van Driessche, I.; Hens, Z., Carboxylic-Acid-Passivated Metal Oxide Nanocrystals: Ligand Exchange Characteristics of a New Binding Motif. *Angewandte Chemie International Edition* **2015,** *54* (22), 6488-6491.

80. Green, M., A new approach to the formal classification of covalent compounds of the elements. *Journal of organometallic chemistry* **1995,** *500* (1-2), 127-148.

81. Lu, W.; Ding, Y.; Chen, Y.; Wang, Z. L.; Fang, J., Bismuth telluride hexagonal nanoplatelets and their two-step epitaxial growth. *Journal of the American Chemical Society* **2005,** *127* (28), 10112-10116.

82. Park, K. H.; Jang, K.; Kim, S.; Kim, H. J.; Son, S. U., Phase-controlled one-dimensional shape evolution of InSe nanocrystals. *Journal of the American Chemical Society* **2006,** *128* (46), 14780-14781.

83. Liu, X.; Li, Y.; Zhou, B.; Wang, X.; Cartwright, A. N.; Swihart, M. T., Shape-controlled synthesis of SnE (E= S, Se) semiconductor nanocrystals for optoelectronics. *Chemistry of Materials* **2014,** *26* (11), 3515-3521.

84. Ramasamy, P.; Kwak, D.; Lim, D.-H.; Ra, H.-S.; Lee, J.-S., Solution synthesis of GeS and GeSe nanosheets for high-sensitivity photodetectors. *Journal of Materials Chemistry C* **2016,** *4* (3), 479-485.

85. Vaughn, D. D.; Patel, R. J.; Hickner, M. A.; Schaak, R. E., Single-crystal colloidal nanosheets of GeS and GeSe. *Journal of the American Chemical Society* **2010,** *132* (43), 15170-15172.

86. Wang, F.; Wang, Z.; Shifa, T. A.; Wen, Y.; Wang, F.; Zhan, X.; Wang, Q.; Xu, K.; Huang, Y.; Yin, L., Two-Dimensional Non-Layered Materials: Synthesis, Properties and Applications. *Advanced Functional Materials* **2017,** *27* (19), 1603254.

87. Chhowalla, M.; Liu, Z.; Zhang, H., Two-dimensional transition metal dichalcogenide (TMD) nanosheets. *Chemical Society Reviews* **2015,** *44* (9), 2584-2586.

88. Bielewicz, T.; Ramin Moayed, M. M.; Lebedeva, V.; Strelow, C.; Rieckmann, A.; Klinke, C., From dots to stripes to sheets: shape control of lead sulfide nanostructures. *Chemistry of Materials* **2015,** *27* (24), 8248-8254.

89. Tan, C.; Zhang, H., Wet-chemical synthesis and applications of non-layer structured two-

dimensional nanomaterials. *Nature communications* **2015,** *6*, 7873.

90.   Shi, Y.; Li, H.; Li, L.-J., Recent advances in controlled synthesis of two-dimensional transition metal dichalcogenides via vapour deposition techniques. *Chemical Society Reviews* **2015,** *44* (9), 2744-2756.

91.   Ling, T.; Wang, J. J.; Zhang, H.; Song, S. T.; Zhou, Y. Z.; Zhao, J.; Du, X. W., Freestanding Ultrathin Metallic Nanosheets: Materials, Synthesis, and Applications. *Advanced Materials* **2015,** *27* (36), 5396-5402.

92.   Yang, H. G.; Liu, G.; Qiao, S. Z.; Sun, C. H.; Jin, Y. G.; Smith, S. C.; Zou, J.; Cheng, H. M.; Lu, G. Q., Solvothermal Synthesis and Photoreactivity of Anatase TiO_2 Nanosheets with Dominant {001} Facets. *Journal of the American Chemical Society* **2009,** *131* (11), 4078-4083.

93.   Chen, J. S.; Lou, X. W., SnO_2-Based Nanomaterials: Synthesis and Application in Lithium-Ion Batteries. *Small* **2013,** *9* (11), 1877-1893.

94.   Huang, X. Q.; Tang, S. H.; Mu, X. L.; Dai, Y.; Chen, G. X.; Zhou, Z. Y.; Ruan, F. X.; Yang, Z. L.; Zheng, N. F., Freestanding palladium nanosheets with plasmonic and catalytic properties. *Nature Nanotechnology* **2011,** *6* (1), 28-32.

95.   Mourdikoudis, S.; Pallares, R. M.; Thanh, N. T. K., Characterization techniques for nanoparticles: comparison and complementarity upon studying nanoparticle properties. *Nanoscale* **2018,** *10* (27), 12871-12934.

96.   Kalantar-zadeh, K.; Fry, B., Characterization techniques for nanomaterials. *Nanotechnology-Enabled Sensors* **2008**, 211-281.

97.   Egerton, R. F., *Physical principles of electron microscopy*. Springer: 2005.

98.   Wu, C. Z.; Lu, X. L.; Peng, L. L.; Xu, K.; Peng, X.; Huang, J. L.; Yu, G. H.; Xie, Y., Two-dimensional vanadyl phosphate ultrathin nanosheets for high energy density and flexible pseudocapacitors. *Nature Communications* **2013,** *4*.

99.   David, B.; WILLIAMS, C.; Barry, C., *Transmission Electron Microscopy: A Textbook for Materials Science*. SPRINGER-VERLAG NEW YORK: 2016.

100. Xin, W.; Yang, J. M.; Li, C.; Goorsky, M. S.; Carlson, L.; De Rosa, I. M., Novel Strategy for One-Pot Synthesis of Gold Nanoplates on Carbon Nanotube Sheet As an Effective Flexible SERS Substrate. *Acs Appl Mater Inter* **2017,** *9* (7), 6246-6254.

101. Xu, Z.; Bando, Y.; Wang, W. L.; Bai, X. D.; Golberg, D., Real-Time In Situ HRTEM-Resolved

Resistance Switching of Ag_2S Nanoscale Ionic Conductor. *Acs Nano* **2016,** *10* (2), 2982-2982.

102. Severin, K. P., *Energy dispersive spectrometry of common rock forming minerals*. Springer: 2004.

103. Hayes, T. L.; Pease, R., The scanning electron microscope: principles and applications in biology and medicine. In *Advances in biological and medical physics*, Elsevier: 1968; Vol. 12, pp 85-137.

104. Crewe, A. V., Scanning electron microscopes: is high resolution possible? *Science* **1966,** *154* (3750), 729-738.

105. Different Types of SEM Imaging – BSE and Secondary Electron Imaging.

106. Seiler, H., Secondary electron emission in the scanning electron microscope. *Journal of Applied Physics* **1983,** *54* (11), R1-R18.

107. MacDonald, N., Auger electron spectroscopy in scanning electron microscopy: Potential measurements. *Applied Physics Letters* **1970,** *16* (2), 76-80.

108. Yacobi, B. G.; Holt, D. B., Cathodoluminescence. In *Cathodoluminescence Microscopy of Inorganic Solids*, Springer: 1990; pp 55-88.

109. Flemban, T. H. High Quality Zinc Oxide Thin films and Nanostructures Prepared by Pulsed Laser Deposition for Photodetectors. 2017.

110. Whiteside, P. J. D.; Chininis, J. A.; Hunt, H. K., Techniques and Challenges for Characterizing Metal Thin Films with Applications in Photonics. *Coatings* **2016,** *6* (3).

111. Binnig, G.; Quate, C. F.; Gerber, C., Atomic Force Microscope. *Physical Review Letters* **1986,** *56* (9), 930-933.

112. Bragg, W. H.; Bragg, W. L., The reflection of X-rays by crystals. *Proceedings of the Royal Society of London. Series A, Containing Papers of a Mathematical and Physical Character* **1913,** *88* (605), 428-438.

113. Skoog, D. A.; Holler, F. J.; Crouch, S. R., *Principles of instrumental analysis*. Cengage learning: 2017.

114. Elmer, P., FT-IR Spectroscopy Attenuated Total Reflectance (ATR). *Technical note* **2005,** *27* (11).

115. Chakravadhanula, V. S. K. Vapor phase deposition of functional nanocomposite thin films and their modification by ion beam irradiation. Christian-Albrechts Universität Kiel, 2011.

116. Griffiths, P. R., Fourier transform infrared spectrometry. *Science* **1983,** *222* (4621), 297-302.

117. Smith, A. L., Applied infrared spectroscopy. Fundamentals, techniques and analytical problem solving. *Applied infrared spectroscopy. Fundamentals, techniques and analytical problem solving., by Smith, AL. Chichester (UK): John Wiley & Sons, 11+ 322 p.* **1979**.

118. Kannan, P. K.; Late, D. J.; Morgan, H.; Rout, C. S., Recent developments in 2D layered inorganic nanomaterials for sensing. *Nanoscale* **2015,** *7* (32), 13293-13312.

119. Yang, G. H.; Zhu, C. Z.; Du, D.; Zhu, J. J.; Lin, Y. H., Graphene-like two-dimensional layered nanomaterials: applications in biosensors and nanomedicine. *Nanoscale* **2015,** *7* (34), 14217-14231.

120. Lin, S.; Carvalho, A.; Yan, S.; Li, R.; Kim, S.; Rodin, A.; Carvalho, L.; Chan, E. M.; Wang, X.; Neto, A. H. C., Accessing valley degree of freedom in bulk Tin (II) sulfide at room temperature. *Nature communications* **2018,** *9* (1), 1455.

121. Koteeswara Reddy, N.; Devika, M.; Gopal, E., Review on tin (II) sulfide (SnS) material: synthesis, properties, and applications. *Critical Reviews in Solid State and Materials Sciences* **2015,** *40* (6), 359-398.

122. Wang, J.; Lian, G.; Xu, Z.; Fu, C.; Lin, Z.; Li, L.; Wang, Q.; Cui, D.; Wong, C.-P., Growth of large-size SnS thin crystals driven by oriented attachment and applications to gas sensors and photodetectors. *Acs Appl Mater Inter* **2016,** *8* (15), 9545-9551.

123. Tian, Z.; Guo, C.; Zhao, M.; Li, R.; Xue, J., Two-dimensional SnS: A phosphorene analogue with strong in-plane electronic anisotropy. *Acs Nano* **2017,** *11* (2), 2219-2226.

124. Guo, R.; Wang, X.; Kuang, Y.; Huang, B., First-principles study of anisotropic thermoelectric transport properties of IV-VI semiconductor compounds SnSe and SnS. *Physical Review B* **2015,** *92* (11), 115202.

125. Kovalenko, M. V.; Heiss, W.; Shevchenko, E. V.; Lee, J. S.; Schwinghammer, H.; Alivisatos, A. P.; Talapin, D. V., SnTe nanocrystals: A new example of narrow-gap semiconductor quantum dots. *Journal of the American Chemical Society* **2007,** *129* (37), 11354-11355.

126. Bhandari, G. B.; Subedi, K.; He, Y. F.; Jiang, Z. F.; Leopold, M.; Reilly, N.; Lu, H. P.; Zayak, A. T.; Sun, L. F., Thickness-Controlled Synthesis of Colloidal PbS Nanosheets and Their Thickness-Dependent Energy Gaps. *Chemistry of Materials* **2014,** *26* (19), 5433-5436.

127. Baumgardner, W. J.; Choi, J. J.; Lim, Y. F.; Hanrath, T., SnSe Nanocrystals: Synthesis, Structure, Optical Properties, and Surface Chemistry. *Journal of the American Chemical Society* **2010,** *132* (28), 9519-9521.

128. Ke, F.; Yang, J.; Liu, C. L.; Wang, Q. L.; Li, Y. Q.; Zhang, J. K.; Wu, L.; Zhang, X.; Han, Y. H.; Wu, B. J.; Ma, Y. Z.; Gao, C. X., High-Pressure Electrical-Transport Properties of SnS: Experimental and Theoretical Approaches. *J Phys Chem C* **2013,** *117* (12), 6033-6038.

129. Li, F.; Moayed, M. M. R.; Gerdes, F.; Kull, S.; Klein, E.; Lesyuk, R.; Klinke, C., Colloidal tin sulfide nanosheets: formation mechanism, ligand-mediated shape tuning and photo-detection. *Journal of Materials Chemistry C* **2018,** *6* (35), 9410-9419.

130. Brent, J. R.; Lewis, D. J.; Lorenz, T.; Lewis, E. A.; Savjani, N.; Haigh, S. J.; Seifert, G.; Derby, B.; O'Brien, P., Tin (II) sulfide (SnS) nanosheets by liquid-phase exfoliation of herzenbergite: IV–VI main group two-dimensional atomic crystals. *Journal of the American Chemical Society* **2015,** *137* (39), 12689-12696.

131. Xia, J.; Li, X. Z.; Huang, X.; Mao, N. N.; Zhu, D. D.; Wang, L.; Xu, H.; Meng, X. M., Physical vapor deposition synthesis of two-dimensional orthorhombic SnS flakes with strong angle/temperature-dependent Raman responses. *Nanoscale* **2016,** *8* (4), 2063-2070.

132. Biacchi, A. J.; Vaughn, D. D.; Schaak, R. E., Synthesis and Crystallographic Analysis of Shape-Controlled SnS Nanocrystal Photocatalysts: Evidence for a Pseudotetragonal Structural Modification. *Journal of the American Chemical Society* **2013,** *135* (31), 11634-11644.

133. de Kergommeaux, A.; Lopez-Haro, M.; Pouget, S.; Zuo, J. M.; Lebrun, C.; Chandezon, F.; Aldakov, D.; Reiss, P., Synthesis, Internal Structure, and Formation Mechanism of Monodisperse Tin Sulfide Nanoplatelets. *Journal of the American Chemical Society* **2015,** *137* (31), 9943-9952.

134. Vaughn, D. D.; In, S. I.; Schaak, R. E., A Precursor-Limited Nanoparticle Coalescence Pathway for Tuning the Thickness of Laterally-Uniform Colloidal Nanosheets: The Case of SnSe. *Acs Nano* **2011,** *5* (11), 8852-8860.

135. Guo, S. J.; Fidler, A. F.; He, K.; Su, D.; Chen, G.; Lin, Q. L.; Pietryga, J. M.; Klimov, V. I., Shape-Controlled Narrow-Gap SnTe Nanostructures: From Nanocubes to Nanorods and Nanowires. *Journal of the American Chemical Society* **2015,** *137* (48), 15074-15077.

136. Kobylinski, M. M.; Ruhmlieb, C.; Kornowski, A.; Mews, A., Hexagonally Shaped Two-Dimensional Tin (II) sulfide Nanosheets: Growth Model and Controlled Structure Formation. *The Journal of Physical Chemistry C* **2018,** *122* (10), 5784-5795.

137. Zhang, Y.; Lu, J.; Shen, S.; Xu, H.; Wang, Q., Ultralarge single crystal SnS rectangular nanosheets. *Chemical Communications* **2011,** *47* (18), 5226-5228.

138. Gerdes, F.; Navío, C.; Juárez, B. H.; Klinke, C., Size, shape, and phase control in ultrathin CdSe nanosheets. *Nano letters* **2017,** *17* (7), 4165-4171.

139. Wenk, H.-R.; Van Houtte, P., Texture and anisotropy. *Reports on Progress in Physics* **2004,** *67* (8), 1367.

140. Xia, Y.; Xia, X.; Peng, H.-C., Shape-controlled synthesis of colloidal metal nanocrystals: thermodynamic versus kinetic products. *Journal of the American Chemical Society* **2015,** *137* (25), 7947-7966.

141. Sun, S.; Yuan, D.; Xu, Y.; Wang, A.; Deng, Z., Ligand-mediated synthesis of shape-controlled cesium lead halide perovskite nanocrystals via reprecipitation process at room temperature. *ACS nano* **2016,** *10* (3), 3648-3657.

142. Ghosh, S.; Manna, L., The many "facets" of halide ions in the chemistry of colloidal inorganic nanocrystals. *Chemical reviews* **2018,** *118* (16), 7804-7864.

143. Kudera, S.; Carbone, L.; Manna, L.; Parak, W. J., Growth mechanism, shape and composition control of semiconductor nanocrystals. In *Semiconductor nanocrystal quantum dots*, Springer: 2008; pp 1-34.

144. Li, R.; Zhang, X.; Dong, H.; Li, Q.; Shuai, Z.; Hu, W., Gibbs–Curie–Wulff Theorem in Organic Materials: A Case Study on the Relationship between Surface Energy and Crystal Growth. *Advanced Materials* **2016,** *28* (8), 1697-1702.

145. Deng, Z.; Han, D.; Liu, Y., Colloidal synthesis of metastable zinc-blende IV–VI SnS nanocrystals with tunable sizes. *Nanoscale* **2011,** *3* (10), 4346-4351.

146. Gao, C.; Shen, H.; Sun, L., Preparation and properties of zinc blende and orthorhombic SnS films by chemical bath deposition. *Applied Surface Science* **2011,** *257* (15), 6750-6755.

147. Stafeeva, V. S.; Mitiaev, A. S.; Abakumov, A. M.; Tsirlin, A. A.; Makarevich, A. M.; Antipov, E. V., Crystal structure and chemical bonding in tin (II) acetate. *Polyhedron* **2007,** *26* (18), 5365-5369.

148. Bielewicz, T.; Dogan, S.; Klinke, C., Tailoring the Height of Ultrathin PbS Nanosheets and Their Application as Field-Effect Transistors. *Small* **2015,** *11* (7), 826-833.

149. Deng, Z.; Cao, D.; He, J.; Lin, S.; Lindsay, S. M.; Liu, Y., Solution synthesis of ultrathin single-crystalline SnS nanoribbons for photodetectors via phase transition and surface processing. *ACS nano* **2012,** *6* (7), 6197-6207.

150. Li, F.; Ramin Moayed, M. M.; Klein, E.; Lesyuk, R.; Klinke, C., In-plane anisotropic faceting of

ultralarge and thin single-crystalline colloidal SnS nanosheets. *The journal of physical chemistry letters* **2019,** *10* (5), 993-999.

151. Tauc, J., Optical properties and electronic structure of amorphous Ge and Si. *Materials Research Bulletin* **1968,** *3* (1), 37-46.

152. Lin, Y.-C.; Komsa, H.-P.; Yeh, C.-H.; Bjorkman, T.; Liang, Z.-Y.; Ho, C.-H.; Huang, Y.-S.; Chiu, P.-W.; Krasheninnikov, A. V.; Suenaga, K., Single-layer ReS$_2$: two-dimensional semiconductor with tunable in-plane anisotropy. *ACS nano* **2015,** *9* (11), 11249-11257.

153. Yang, Y.; Liu, S.-C.; Yang, W.; Li, Z.; Wang, Y.; Wang, X.; Zhang, S.; Zhang, Y.; Long, M.; Zhang, G., Air-stable in-plane anisotropic GeSe$_2$ for highly polarization-sensitive photodetection in short wave region. *Journal of the American Chemical Society* **2018,** *140* (11), 4150-4156.

154. Peng, Z. A.; Peng, X., Nearly monodisperse and shape-controlled CdSe nanocrystals via alternative routes: nucleation and growth. *Journal of the American Chemical Society* **2002,** *124* (13), 3343-3353.

155. Choi, J. J.; Bealing, C. R.; Bian, K.; Hughes, K. J.; Zhang, W.; Smilgies, D.-M.; Hennig, R. G.; Engstrom, J. R.; Hanrath, T., Controlling nanocrystal superlattice symmetry and shape-anisotropic interactions through variable ligand surface coverage. *Journal of the American Chemical Society* **2011,** *133* (9), 3131-3138.

156. Vidal, J.; Lany, S.; d'Avezac, M.; Zunger, A.; Zakutayev, A.; Francis, J.; Tate, J., Band-structure, optical properties, and defect physics of the photovoltaic semiconductor SnS. *Applied Physics Letters* **2012,** *100* (3), 032104.

157. Xi, L.; Chua, K. H.; Zhao, Y.; Zhang, J.; Xiong, Q.; Lam, Y. M., Controlled synthesis of CdE (E= S, Se and Te) nanowires. *RSC Advances* **2012,** *2* (12), 5243-5253.

158. Antunez, P. D.; Buckley, J. J.; Brutchey, R. L., Tin and germanium monochalcogenide IV–VI semiconductor nanocrystals for use in solar cells. *Nanoscale* **2011,** *3* (6), 2399-2411.

159. Guo, S.; Fidler, A. F.; He, K.; Su, D.; Chen, G.; Lin, Q.; Pietryga, J. M.; Klimov, V. I., Shape-controlled narrow-gap SnTe nanostructures: From nanocubes to nanorods and nanowires. *Journal of the American Chemical Society* **2015,** *137* (48), 15074-15077.

160. Grzelczak, M.; Pérez-Juste, J.; Mulvaney, P.; Liz-Marzán, L. M., Shape control in gold nanoparticle synthesis. *Chemical Society Reviews* **2008,** *37* (9), 1783-1791.

161. Kull, S.; Heymann, L.; Hungria, A. B.; Klinke, C., Synthesis of Single-Crystalline Lead Sulfide

Nanoframes and Nanorings. *Chemistry of Materials*.

162. Norman, Z. M.; Anderson, N. C.; Owen, J. S., Electrical transport and grain growth in solution-cast, chloride-terminated cadmium selenide nanocrystal thin films. *ACS nano* **2014,** *8* (7), 7513-7521.

163. Meyns, M.; Iacono, F.; Palencia, C.; Geweke, J.; Coderch, M. D.; Fittschen, U. E.; Gallego, J. M.; Otero, R.; Juárez, B. H.; Klinke, C., Shape evolution of CdSe nanoparticles controlled by halogen compounds. *Chemistry of Materials* **2014,** *26* (5), 1813-1821.

164. Carlos, L. D.; de Zea Bermudez, V.; Amaral, V. S.; Nunes, S. C.; Silva, N. J.; Sá Ferreira, R. A.; Rocha, J.; Santilli, C. V.; Ostrovskii, D., Nanoscopic Photoluminescence Memory as a Fingerprint of Complexity in Self-Assembled Alkyl/Siloxane Hybrids. *Advanced Materials* **2007,** *19* (3), 341-348.

165. Zhang, Z.; Yang, J.; Zhang, K.; Chen, S.; Mei, F.; Shen, G., Anisotropic photoresponse of layered 2D SnS-based near infrared photodetectors. *Journal of Materials Chemistry C* **2017,** *5* (43), 11288-11293.

166. Huang, L.; Wu, F.; Li, J., Structural anisotropy results in strain-tunable electronic and optical properties in monolayer GeX and SnX (X= S, Se, Te). *The Journal of chemical physics* **2016,** *144* (11), 114708.

167. Saghir, M.; Lees, M.; York, S.; Balakrishnan, G., Synthesis and characterization of nanomaterials of the topological crystalline insulator SnTe. *Crystal Growth & Design* **2014,** *14* (4), 2009-2013.

168. Safdar, M.; Wang, Q.; Mirza, M.; Wang, Z.; He, J., Crystal shape engineering of topological crystalline insulator SnTe microcrystals and nanowires with huge thermal activation energy gap. *Crystal Growth & Design* **2014,** *14* (5), 2502-2509.

169. Lee, B.; Stoumpos, C. C.; Zhou, N.; Hao, F.; Malliakas, C.; Yeh, C.-Y.; Marks, T. J.; Kanatzidis, M. G.; Chang, R. P., Air-stable molecular semiconducting iodosalts for solar cell applications: Cs_2SnI_6 as a hole conductor. *Journal of the American Chemical Society* **2014,** *136* (43), 15379-15385.

170. Dolzhnikov, D. S.; Wang, C.; Xu, Y.; Kanatzidis, M. G.; Weiss, E. A., Ligand-Free, Quantum-Confined Cs_2SnI_6 Perovskite Nanocrystals. *Chemistry of Materials* **2017,** *29* (18), 7901-7907.

171. Weidman, M. C.; Seitz, M.; Stranks, S. D.; Tisdale, W. A., Highly tunable colloidal perovskite nanoplatelets through variable cation, metal, and halide composition. *ACS nano* **2016,** *10* (8), 7830-7839.

172. Wang, A.; Yan, X.; Zhang, M.; Sun, S.; Yang, M.; Shen, W.; Pan, X.; Wang, P.; Deng, Z., Controlled synthesis of lead-free and stable perovskite derivative Cs_2SnI_6 nanocrystals via a facile hot-injection process. *Chemistry of Materials* **2016,** *28* (22), 8132-8140.

173. Weidman, M. C.; Goodman, A. J.; Tisdale, W. A., Colloidal halide perovskite nanoplatelets: an exciting new class of semiconductor nanomaterials. *Chemistry of Materials* **2017,** *29* (12), 5019-5030.

174. Jellicoe, T. C.; Richter, J. M.; Glass, H. F. J.; Tabachnyk, M.; Brady, R.; Dutton, S. n. E.; Rao, A.; Friend, R. H.; Credgington, D.; Greenham, N. C., Synthesis and optical properties of lead-free cesium tin halide perovskite nanocrystals. *Journal of the American Chemical Society* **2016,** *138* (9), 2941-2944.

175. Noel, N. K.; Stranks, S. D.; Abate, A.; Wehrenfennig, C.; Guarnera, S.; Haghighirad, A.-A.; Sadhanala, A.; Eperon, G. E.; Pathak, S. K.; Johnston, M. B., Lead-free organic–inorganic tin halide perovskites for photovoltaic applications. *Energy & Environmental Science* **2014,** *7* (9), 3061-3068.

176. Ke, W.; Stoumpos, C. C.; Kanatzidis, M. G., "Unleaded" Perovskites: Status Quo and Future Prospects of Tin-Based Perovskite Solar Cells. *Advanced Materials* **2018**, 1803230.

177. Yang, W. S.; Noh, J. H.; Jeon, N. J.; Kim, Y. C.; Ryu, S.; Seo, J.; Seok, S. I., High-performance photovoltaic perovskite layers fabricated through intramolecular exchange. *Science* **2015,** *348* (6240), 1234-1237.

178. The CP2K developers group. CP2K is freely available from http://www.cp2k.org/.

179. Sigma-Aldrich, found at https://www.sigmaaldrich.com/germany.html.

180. Gestis-stoffdatenbank, https://www.dguv.de/ifa/gestis/gestis-stoffdatenbank/index.jsp.

181. GHS_hazard_statements, found at https://en.wikipedia.org/wiki/GHS_hazard_statements.

Acknowledgements

"Stop chipping halfway, even a decayed piece of wood will not break; keep chipping, gold and stone can be engraved", said by a famous philosopher Zi Xun (荀子) from China. This is an old Chinese proverb which indicates the success is closely related to the ability of persistence, and independent on the difficulties. I think this is very suitable here. Studying for a Ph.D. program is really hard work during any period of our lives, not only because of the hardness of the Ph.D. project, but also the pressure we need to bear from that, physically and psychologically. Among all these pursuing-dream Ph.D. candidates, I think I am the luckier one, who encounters an interesting project which I am holding my passion on, meets a super nice professor who always supports me, participates a wonderful researching group which is filled with laughter and inspiration, and owns an enlightened family who always encourages me and sweeps away all my worries. Hence, I would like to express my gratitude and thanks to all the people and organizations who have supported me and have accompanied me during my four-year Ph.D. period.

I thank Prof. Dr. Christian Klinke sincerely for his support all the time. I am kind of lacking confidence and decision-ability. However, I thank you, for always encouraging me, suggesting me to do as much as discussion with you, or with colleagues if necessary, without being shy. This really helps me a lot, shedding light on the blurry problems and also inspiring more meaning questions and thinking. I thank you for all the professional suggestions and efforts such as DFT calculations and numerous stimulating discussions. I am also very grateful for the high degree of freedom on the science topic from you, as well as the opportunity to the related conferences with practicing talks and discussions. I thank you for being nice all the time with cordial smiles and jokes which sometimes need intelligence for understanding.

I thank all my colleagues in the working group of Klinke who are always being nice to me and tolerate me when I sometimes act emotionally. I thank Dr. Rostyslav Lesyuk, who is always patient to me with my tons of questions and incredibly supportive of my projects. I thank Mehdi Ramin for the precious contributions on all the papers with professional electronic

Fu Li

10/07/2019

Jülich, Germany

Declaration

According to § 7 (4) of the doctoral degree regulations from The Faculty of Mathematics, Informatics and Natural Sciences (MIN) of the University of Hamburg:

"Hereby, I declare on oath that I have written this dissertation on my own. I have not applied other than the acknowledged resources and aids. The submitted written version corresponds to the version which is shown the electronic storage medium. I declare here that the dissertation is not in an earlier one for a doctorate (Ph.D. study).

Fu LI

_____

Date, Signature